

Synthesis and Reactivity of Chromium and Vanadium Complexes  
for Atomic Layer Deposition

By

Aya Kadri, H.B.Sc.

A Thesis Submitted to the School of Graduate Studies in Partial  
Fulfillment of the Requirements for the Degree of  
Master of Science

McMaster University

© Copyright by Aya Kadri, December 2022

# Table of Contents

Acknowledgments.....	iv
Abstract.....	v
List of Figures.....	vii
List of Tables.....	xiii
List of Appendix Tables.....	xiii
List of Schemes.....	xiv
List of Compounds Synthesized.....	xv
List of Abbreviations.....	xvi
Declaration of Academic Achievement.....	xix
1 Introduction.....	1
1.1 Atomic Layer Deposition.....	3
1.2 Properties of Potential ALD Precursors.....	14
1.3 Solution State Reactivity Analyses.....	18
1.4 Homoleptic Vanadium Alkoxide Complexes.....	19
1.5 Homoleptic Chromium Alkoxide Complexes.....	22
1.6 Deposition of Vanadium- and Chromium-Containing Thin Films by ALD.....	24
1.7 Cyclic Voltammetry.....	27
2 Homoleptic <i>Tert</i> -butoxide Complexes of Vanadium and Chromium.....	32
2.1 Precursor Molecules, Co-reagents, and Proposed Reactivity.....	32
2.2 Synthesis and Characterization of [Cr(O <sup>t</sup> Bu) <sub>4</sub> ] ( <b>1</b> ) and [V(O <sup>t</sup> Bu) <sub>4</sub> ] ( <b>2</b> ).....	34
2.3 Thermal Stability and Volatility of [Cr(O <sup>t</sup> Bu) <sub>4</sub> ] ( <b>1</b> ).....	36
2.4 Thermal Stability and Volatility of [V(O <sup>t</sup> Bu) <sub>4</sub> ] ( <b>2</b> ).....	41
2.5 Reactivity Studies with HBpin.....	45
2.6 Reactivity Studies with PhSiH <sub>3</sub> .....	50
2.7 Reactivity Studies with decamethylsilicocene ( <b>3</b> ), and 1,4-bis(trimethylsilyl)-2-methyl-2,5-cyclohexadiene ( <b>4</b> ).....	57
2.8 Reactivity Studies with HBpin in the Presence of an Internal Standard.....	58
3 Perfluoro- <i>tert</i> -butoxide Complexes of Vanadium and Chromium.....	63
3.1 Synthesis and Characterization.....	63
3.2 Elemental Analysis and PXRD of K[V(pftb) <sub>4</sub> ] ( <b>6</b> ).....	75
3.3 Thermal Properties of K[V(pftb) <sub>4</sub> ] ( <b>6</b> ).....	78

3.4	Reactivity Studies with HBpin.....	82
3.5	Reactivity Studies with PhSiH <sub>3</sub> .....	82
3.6	Cyclic Voltammograms of Complexes <b>6</b> , <b>1</b> , and <b>2</b> .....	84
4	Conclusions and Future Work .....	93
5	Experimental.....	96
5.1	General Experimental Conditions .....	96
5.2	Synthetic Procedures .....	97
5.3	Solution State Reactions.....	104
6	References .....	108

## Acknowledgments

First and foremost, I would like to endlessly thank Professor David J. H. Emslie for his unwavering support and understanding. This degree was nearly impossible for many reasons, and I am so grateful you stood by me throughout it all. I could not be the person I have become, with this thesis completed, if it were not for your empathy and kindness. I am deeply indebted to you. It was an honour being your student.

Secondly, I would like to thank my chosen chemistry family. Thank you Majeda Al Hareri for literally holding me up and for bearing with all the meltdowns and tears, and for the much needed random hugs, Katia Paskaruk for being my mentor in the lab and for teaching me how to truly accept who I am, Nicholas Hoffman for the words of wisdom and always encouraging me to be the best version of myself, Lord Commander Novan Gray for all the extravagant adventures and reminders to enjoy life as it is, Dr. Jeffrey S. Price for forcing me into the softball team and for all the Friday evening ribs, and Griffin J. LaChapelle for making all the Dr. Pong appointments possible. You all made this experience so much more bearable, and I have grown so much as a person from all the moments we shared. Stay crispy.

Finally, my dearest and closest friend Ksenia Varga. I am so grateful we suffered third year 8 AM analytical chemistry together and for you asking if I'm born late April or early May because I'm "a taurus and it's very obvious". You blew my mind and for a moment I was terrified of you. I still am. You are the sister I wish I had, who stood by me when I needed it most. Hope you enjoyed the industrial grade box of Gushers™.

## Abstract

New vapour phase thin film deposition methods to enable manufacturing of increasingly smaller transistors are in high demand. Atomic layer deposition (ALD) is a thin film deposition method that yields uniquely conformal and uniform thin films through the sequential exposure of vapour-phase reagents to a surface. Typically, two reagents are used: (1) a metal-containing precursor complex and (2) a co-reagent which reacts with the precursor complex to afford the target material. Any by-products of this surface-based reactivity must be volatile, such that they can be removed by interpolated inert gas purges. One ALD cycle consists of exposure of the surface to a precursor, followed by an inert gas purge, followed by a pulse of co-reagent, and then a final inert gas purge. The thin film thickness in an ideal ALD method is controlled solely by the number of ALD cycles utilized.

Developing an ALD method requires accurate control of precursor design, so as to achieve the required thermal stability and volatility, as well as the desired reactivity with a chosen co-reagent. This work investigates the feasibility of using homoleptic chromium and vanadium alkoxides as precursors for metal ALD when combined with hydrosilanes or hydroboranes as the co-reagents. The synthesis of  $[\text{Cr}(\text{O}^t\text{Bu})_4]$  (**1**) and  $[\text{V}(\text{O}^t\text{Bu})_4]$  (**2**) was carried out according to literature procedures, with some modifications. Complex **1** sublimed at 25 °C (10 mTorr) and decomposed when a neat sample was heated to 110 °C for 24 hours. Complex **2** distilled at 25 °C (10 mTorr) and decomposed when a neat sample was heated to 110 °C (in the dark) for 24 hours. Pinacolborane (HBpin) and phenylsilane ( $\text{PhSiH}_3$ ) commercial reagents were explored as potential co-reagents through solution reactivity studies. Decamethylsilicocene (**3**), and

1,4-bis(trimethylsilyl)-2-methyl-2,5-cyclohexadiene (**4**), which were synthesized according to literature procedures, and were also explored as potential co-reagents. The reactions of **1** and **2** with HBpin were particularly promising, and suggested the possibility of utilizing these reagents for the development of a new method for chromium and vanadium metal ALD.

Additionally, chromium and vanadium complexes containing fluorinated alkoxide ligands, perfluoro-*tert*-butoxide (pftb), were synthesized in an attempt to increase the thermal stability of the precursors.  $[\text{CrCl}(\text{pftb})_2(\text{THF})_3]$  (**5**) and  $\text{K}[\text{V}(\text{pftb})_4]$  (**6**) were crystallized from these reactions. Complex **5** could not be isolated in pure form, whereas pure **6** was isolated in 59% yield. Complex **6** sublimed at 75-85 °C (10 mTorr) and exhibited some decomposition when a neat sample was heated at 130 °C for 24 hours. Complexes **5** and **6** proved to be far less reactive towards HBpin and  $\text{PhSiH}_3$  than **1** and **2**. In order to determine a suitable oxidizing agent for the synthesis of the target complex,  $[\text{V}(\text{pftb})_4]$ , cyclic voltammetry was utilized to determine the oxidation potential of **6**. The  $E_{1/2}$  value for  $\mathbf{6}^{0/+}$  was determined to be approximately 0.64 V versus  $[\text{FeCp}_2]^{+/0}$  in 1,2-difluorobenzene.

## List of Figures

<b>Figure 1.1.1</b> Schematic illustration of an ALD cycle (in this case for metal ALD). .....	5
<b>Figure 1.1.2</b> Surface and flux controlled growth in a via; highlighting the difference in film conformality between ALD (left) and CVD/PVD (right). Figure adapted from H. Knoops. <sup>22,23</sup> Licensed under Creative Commons.....	7
<b>Figure 1.1.3</b> Film thickness as a function of ALD cycles with emphasis on the different rates of growth. ....	9
<b>Figure 1.1.4</b> Comparison of reaction-limited growth (left) and diffusion-limited growth (right) in a high aspect ratio morphology. <sup>25</sup> Licensed under Creative Commons. ....	10
<b>Figure 1.1.5</b> Relationship between increasing dosage time and surface coverage ( $\theta$ ) resulting in a constant GPC due to surface saturation. <sup>25,27</sup> Licensed under Creative Commons. ....	12
<b>Figure 1.1.6</b> Saturation curve of the growth per cycle of the deposited film as a function of reactant dosing time, illustrating the difference between CVD and ALD type growth. ....	13
<b>Figure 1.6.1</b> Chromium film thickness obtained with respect to the number of ALD cycles at a deposition temperature of 180 °C indicating a plateau past 1000 ALD cycles. Reproduced with permission from Kalutarage, L. C.; Martin, P. D.; Heeg, M. J.; Winter, C. H. Volatile and Thermally Stable Mid to Late Transition Metal Complexes Containing $\alpha$ -Imino Alkoxide Ligands, a New Strongly Reducing Coreagent, and Thermal Atomic Layer Deposition of Ni, Co, Fe, and Cr Metal Films. <i>J. Am. Chem. Soc.</i> <b>2013</b> , 135, 34, 12588–12591. <sup>77</sup> .....	26
<b>Figure 1.7.1</b> Typical cyclic voltammogram of an electrochemically active analyte .....	28

<b>Figure 1.7.2</b> Application of the Nicholson equation check to a typical cyclic voltammogram .....	31
<b>Figure 2.1.1</b> Structures of the potential co-reagents decamethylsilicocene ( <b>3</b> ), and 1,4-bis(trimethylsilyl)-2-methyl-2,5-cyclohexadiene ( <b>4</b> ).....	33
<b>Figure 2.2.1</b> <sup>1</sup> H NMR spectra (C <sub>6</sub> D <sub>6</sub> , 600 MHz) of [Cr(O <sup>t</sup> Bu) <sub>4</sub> ] ( <b>1</b> ) (top) and [V(O <sup>t</sup> Bu) <sub>4</sub> ] ( <b>2</b> ) (bottom).....	36
<b>Figure 2.3.1</b> <sup>1</sup> H NMR spectrum (C <sub>6</sub> D <sub>6</sub> , 600 MHz) of the decomposition products after heating neat [Cr(O <sup>t</sup> Bu) <sub>4</sub> ] ( <b>1</b> ) at 110 °C for 3 days. ....	37
<b>Figure 2.3.2</b> TGA data for complex <b>1</b> , and the derivative curve expressed as the rate of change of the percentage mass with respect to temperature. ....	40
<b>Figure 2.4.1</b> <sup>1</sup> H NMR spectrum (C <sub>6</sub> D <sub>6</sub> , 600 MHz) of the decomposition products of neat [V(O <sup>t</sup> Bu) <sub>4</sub> ] ( <b>2</b> ) after heating at 75 °C overnight.....	41
<b>Figure 2.4.2</b> <sup>1</sup> H NMR spectrum (C <sub>6</sub> D <sub>6</sub> , 600 MHz) of the repeated analysis of the decomposition products of [V(O <sup>t</sup> Bu) <sub>4</sub> ] ( <b>2</b> ) after heating at 75 °C overnight.....	42
<b>Figure 2.4.3</b> TGA data for complex <b>2</b> , and the derivative curve expressed as the rate of change of the percentage mass with respect to temperature. ....	44
<b>Figure 2.5.1</b> <sup>1</sup> H NMR spectrum (C <sub>6</sub> D <sub>6</sub> , 600 MHz) of the reaction between [Cr(O <sup>t</sup> Bu) <sub>4</sub> ] ( <b>1</b> ) and 5.6 equivalents of HBpin in a J-Young tube after 24 hours at room temperature.	46
<b>Figure 2.5.2</b> Colour changes associated with the reaction of complex <b>2</b> with HBpin in C <sub>6</sub> D <sub>6</sub> . ....	48
<b>Figure 2.5.3</b> <sup>1</sup> H NMR spectrum (C <sub>6</sub> D <sub>6</sub> , 600 MHz) of the reaction between [V(O <sup>t</sup> Bu) <sub>4</sub> ] ( <b>2</b> ) and HBpin in a J-Young tube after 1 hour at room temperature. ....	49

<b>Figure 2.6.1</b> $^1\text{H}$ NMR spectrum ( $\text{C}_6\text{D}_6$ , 600 MHz) of the reaction between $[\text{Cr}(\text{O}^t\text{Bu})_4]$ ( <b>1</b> ) and $\text{PhSiH}_3$ in a J-Young tube after 3 days at 60 °C. ....	51
<b>Figure 2.6.2</b> PXRD diffractogram of the brown powder isolated from the reaction of $[\text{Cr}(\text{O}^t\text{Bu})_4]$ ( <b>1</b> ) and $\text{PhSiH}_3$ . ....	52
<b>Figure 2.6.3</b> $^1\text{H}$ NMR spectra ( $\text{C}_6\text{D}_6$ , 600 MHz) of the reaction between $[\text{V}(\text{O}^t\text{Bu})_4]$ ( <b>2</b> ) and $\text{PhSiH}_3$ in a J-Young tube over the course of 5 days at 70 °C. ....	53
<b>Figure 2.6.4</b> Nuclear Overhauser Effect Spectroscopy (NOESY) NMR spectrum of the reaction between $\text{PhSiH}_3$ and complex <b>2</b> after five days at 70 °C highlighting the aromatic region and the correspondence to the Si-H moiety and the tert-butoxide substituted ligand.....	54
<b>Figure 2.6.5</b> $^1\text{H}$ NMR spectrum ( $\text{C}_6\text{D}_6$ , 600 MHz, $d_1=30\text{s}$ ) of the reaction between $[\text{V}(\text{O}^t\text{Bu})_4]$ ( <b>2</b> ) and $\text{PhSiH}_3$ in a J-Young tube after 5 days at 70 °C indicating the major product of the reaction to be bis(tert-butoxide) phenyl silane. ....	56
<b>Figure 2.8.1</b> Diagram illustrating the method for use of an internal standard to monitor the degree of reactivity between <b>1</b> and HBpin.....	59
<b>Figure 2.8.2</b> $^1\text{H}$ NMR spectra ( $\text{C}_6\text{D}_6$ , 600 MHz) of $[\text{Cr}(\text{O}^t\text{Bu})_4]$ ( <b>1</b> ) and hexamethylbenzene as an internal standard (top, green), the reaction between $[\text{Cr}(\text{O}^t\text{Bu})_4]$ ( <b>1</b> ) and excess TFA in the presence of an internal standard in a J-Young tube after 24 hours at room temperature (middle, red), and the reaction between $[\text{Cr}(\text{O}^t\text{Bu})_4]$ ( <b>1</b> ) and excess HBpin in the presence of an internal standard in a J-Young tube after 24 hours at room temperature (bottom, blue). ....	60

<b>Figure 2.8.3</b> $^1\text{H}$ NMR spectrum ( $\text{C}_6\text{D}_6$ , 600 MHz) of the reaction between $[\text{V}(\text{O}^t\text{Bu})_4]$ ( <b>2</b> ) and excess HBpin with hexamethylbenzene as an internal standard in a J-Young tube after 24 hours at room temperature. ....	62
<b>Figure 3.1.1</b> $^{19}\text{F}$ NMR spectrum (THF, 188 MHz, externally referenced to $\text{CFCl}_3$ ) of the isolated material from the reaction between $\text{CrCl}_3 \cdot 3\text{THF}$ and 4 equivalents of Kpftb after 24 hours at 60 °C.....	65
<b>Figure 3.1.2</b> SCXRD crystal structure of $[\text{CrCl}(\text{pftb})_2(\text{THF})_3]$ ( <b>5</b> ) with ellipsoids presented at 50% probability. Hydrogen atoms are omitted for clarity. Space group $\text{P2}_1/\text{c}$ , $R_1 = 3.12\%$ .....	66
<b>Figure 3.1.3</b> $^{19}\text{F}$ NMR spectra (THF, 188 MHz, externally referenced to $\text{CFCl}_3$ ) of the major species from the reaction between $[\text{CrCl}_3(\text{THF})_3]$ and 4 equivalents of Kpftb over the course of two days, showing an increase in intensity of the signal corresponding to Kpftb at $-75$ ppm, and the growth of a baseline peak at $-12$ ppm. ....	68
<b>Figure 3.1.4</b> $^{19}\text{F}$ NMR spectrum (THF, 188 MHz, externally referenced to $\text{CFCl}_3$ ) of the reaction between $[\text{CrCl}_3(\text{THF})_3]$ and 2 equivalents of Kpftb after 24 hours at 60 °C.....	69
<b>Figure 3.1.5</b> $^{19}\text{F}$ NMR spectrum (THF, 188 MHz, externally referenced to $\text{CFCl}_3$ ) of the reaction between $[\text{CrCl}_3(\text{THF})_3]$ and 2 equivalents of Kpftb after 24 hours at room temperature. ....	70
<b>Figure 3.1.6</b> $^{19}\text{F}$ NMR spectrum (THF, 188 MHz, externally referenced to $\text{CFCl}_3$ ) of the isolated product from the reaction between $[\text{VCl}_3(\text{THF})_3]$ and 4 equivalents of Kpftb. ..	71
<b>Figure 3.1.7</b> SCXRD crystal structure of $[(\eta^3\text{-Tol})\text{K}(\mu\text{-pftb})_2\text{V}(\text{pftb})_2]$ ( <b>6</b> (toluene)) with ellipsoids presented at 50% probability. Hydrogen atoms are omitted for clarity. Space group $\text{P2}_1/\text{c}$ , $R_1 = 8.19\%$ . ....	72

<b>Figure 3.1.8</b> $^{19}\text{F}$ NMR spectrum (THF, 188 MHz, externally referenced to $\text{CFCl}_3$ ) of complex <b>6</b> after being left in solution for 8 days, indicating growth of the peak at – 73 ppm corresponding to $\text{Kpftb}$ . .....	75
<b>Figure 3.2.1</b> PXRDs of $\text{Kpftb}$ (black) and the bulk sample of complex <b>6</b> (red). .....	76
<b>Figure 3.2.2</b> PXRD of the bulk sample of <b>6</b> which was not exposed to THF; (red) and the simulated powder pattern obtained from the crystal structure of <b>6</b> (toluene) (black). .....	77
<b>Figure 3.2.3</b> PXRD of the sample of complex <b>6</b> that was not exposed to THF post-crystallization (red) and the sample of complex <b>6</b> that was exposed to THF post-crystallization (black) indicating no variability in the solid state. ....	78
<b>Figure 3.3.1</b> $^{19}\text{F}$ NMR spectrum (THF, 188 MHz, externally referenced to $\text{CFCl}_3$ ) of the decomposition products formed from complex <b>6</b> after heating at 130 °C overnight. ....	80
<b>Figure 3.3.2</b> TGA data for complex <b>6</b> , and the derivative curve expressed as the rate of change of the percentage mass with respect to temperature. ....	81
<b>Figure 3.5.1</b> $^{19}\text{F}$ NMR spectrum (THF- $d_8$ , 565 MHz) of the reaction between $\text{K}[\text{V}(\text{pftb})_4]$ ( <b>6</b> ) and $\text{PhSiH}_3$ after 24 hours at 90 °C. ....	83
<b>Figure 3.5.2</b> $^1\text{H}$ NMR spectrum (THF- $d_8$ , 600 MHz) of the reaction between $\text{K}[\text{V}(\text{pftb})_4]$ ( <b>6</b> ) and $\text{PhSiH}_3$ after 24 hours at 90 °C. ....	84
<b>Figure 3.6.1</b> Cyclic Voltammograms of $\text{K}[\text{V}(\text{pftb})_4]$ ( <b>6</b> ) and the internal calibrant $[\text{FeCp}^*_2]^{+/0}$ ( $E_{1/2} = -597$ mV versus $[\text{FeCp}_2]^{+/0}$ in 1,2-difluorobenzene (DFB)). Working and counter electrodes: Pt; pseudo-reference electrode: $\text{Ag}^+/\text{Ag}$ ; base electrolyte: $[\text{NBu}_4][\text{B}(\text{C}_6\text{F}_5)]$ . ....	86
<b>Figure 3.6.2</b> Randles-Sevcik plot of the anodic current ( <i>ipf</i> ) of complex <b>6</b> versus the square root of the scan rate ( $\nu^{1/2}$ ) indicating linearity ( $R^2 = 0.9995$ ). ....	87

**Figure 3.6.3** Cyclic Voltammograms of  $[V(O^tBu)_4]$  (**2**) in a 0.1 M  $[NBu_4][B(C_6F_5)_4]$  solution in difluorobenzene (DFB) using  $[FeCp^*_2]^{+/0}$  ( $E_{1/2} = -597$  mV) as a calibrant referenced to  $[FeCp_2]^{+/0}$  externally. Working and counter electrodes: Pt; reference electrode:  $Ag^+/Ag$ . ..... 89

**Figure 3.6.4** Cyclic Voltammogram showing oxidation and reduction of  $[Cr(O^tBu)_4]$  (**1**) in a 0.1 M  $[NBu_4][B(C_6F_5)_4]$  solution in difluorobenzene (DFB) using  $[FeCp^*_2]^{+/0}$  ( $E_{1/2} = -597$  mV) as a calibrant referenced to  $[FeCp_2]^{+/0}$  externally. Working and counter electrodes: Pt; reference electrode:  $Ag^+/Ag$ ..... 91

## List of Tables

<b>Table 2.7.1</b> Summary of all attempted solution state reactivity between [Cr(O <sup>t</sup> Bu) <sub>4</sub> ] ( <b>1</b> ), [V(O <sup>t</sup> Bu) <sub>4</sub> ] ( <b>2</b> ), and potential co-reagents.....	57
<b>Table 3.1.1</b> Selected bond distances (Å) and angles (°) from the obtained crystal structure of [CrCl(pftb) <sub>2</sub> (THF) <sub>3</sub> ] ( <b>5</b> ) highlighting the distorted octahedral geometry.....	67
<b>Table 3.1.2</b> Selected bond distances (Å) and angles (°) from the obtained crystal structure of [(η <sup>3</sup> -Tol)K(μ-pftb) <sub>2</sub> V(pftb) <sub>2</sub> ] { <b>6</b> (toluene)}, highlighting the distorted tetrahedral geometry.....	74
<b>Table 3.6.1</b> Peak-to-peak separations (ΔE <sub>p</sub> ) for the calibrant, [FeCp* <sub>2</sub> ] <sup>+0</sup> , and complex <b>6</b> with respect to increasing scan rates.....	88
<b>Table 3.6.2</b> Peak-to-peak separations (ΔE <sub>p</sub> ) for the calibrant, [FeCp* <sub>2</sub> ] <sup>+0</sup> , and complex <b>2</b> with respect to increasing scan rates.....	90
<b>Table 3.6.3</b> Nicholson equation parameters calculated to determine the electrochemical reversibility of complex <b>2</b> using the 50 mV/s and 500 mV/s voltammograms.....	90
<b>Table 3.6.4</b> Peak-to-peak separations (ΔE <sub>p</sub> ) for the calibrant, [FeCp* <sub>2</sub> ] <sup>+0</sup> , and complex <b>1</b> with respect to increasing scan rates.....	92

## List of Appendix Tables

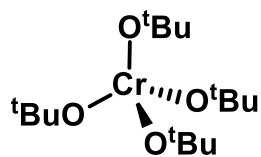
<b>Table A</b> Crystal and Structure refinement data for [CrCl(pftb) <sub>2</sub> (THF) <sub>3</sub> ] ( <b>5</b> ).....	106
<b>Table B</b> Crystal and Structure refinement data for [(η <sup>3</sup> -Tol)K(μ-pftb) <sub>2</sub> V(pftb) <sub>2</sub> ] { <b>6</b> (toluene)}.....	107

## List of Schemes

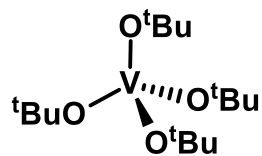
<b>Scheme 2.1.1</b> Hypothesized reaction pathways for the deposition of elemental metal through the reaction of a metal alkoxide with a hydrosilane ( $\text{PhSiH}_3$ ) and or a hydroborane (HBpin).....	32
<b>Scheme 2.1.2</b> Hypothesized reaction pathways for the deposition of elemental metal through the reaction of a metal alkoxide with silicon-containing compounds <b>3</b> and <b>4</b> . ...	34
<b>Scheme 2.2.1</b> Synthesis of $[\text{M}(\text{O}^t\text{Bu})_4]$ , $\text{M} = \text{Cr}$ ( <b>1</b> ) or $\text{M} = \text{V}$ ( <b>2</b> ).....	35
<b>Scheme 2.3.1</b> Proposed decomposition mechanism for $[\text{Cr}(\text{O}^t\text{Bu})_4]$ ( <b>1</b> ). .....	37
<b>Scheme 2.4.1</b> Possible decomposition mechanism for $[\text{V}(\text{O}^t\text{Bu})_4]$ ( <b>2</b> ) .....	43
<b>Scheme 2.5.1</b> Proposed pathway for the reaction between complex <b>1</b> and HBpin. ....	46
<b>Scheme 3.1.1</b> Proposed synthetic route to synthesize $[\text{M}(\text{pftb})_4]$ ( $\text{M} = \text{Cr}$ or $\text{V}$ ).....	64
<b>Scheme 5.2.1</b> Reactions involved in the synthesis of bis(pentamethylcyclopentadienyl) silicocene ( <b>3</b> ).....	99

## List of Compounds Synthesized

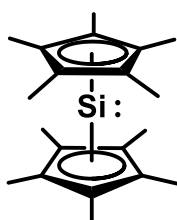
(Complexes **5** and **6** have not previously been reported)



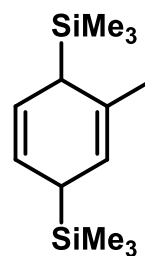
(1)



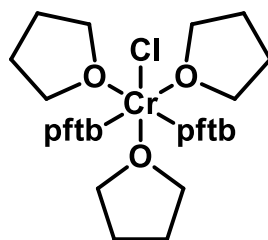
(2)



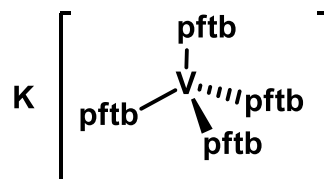
(3)



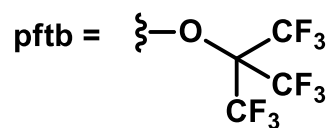
(4)



(5)



(6)



## List of Abbreviations

acac – acetylacetonate

<sup>act</sup>Pe – active pentyl; CH<sub>2</sub>CHMeEt

ALD – Atomic Layer Deposition

COSY – Correlated Spectroscopy

Cp – Cyclopentadienyl

Cp\* – Pentamethylcyclopentadienyl

CV – Cyclic Voltammetry

CVD – Chemical Vapour Deposition

Cy – cyclohexyl

DFB – Difluorobenzene

EPR – Electron Paramagnetic Resonance

FET – field effect transistor

GPC – Growth Per Cycle

HBpin – Pinacolborane

HSQC – Heteronuclear Single Quantum Correlation

<sup>i</sup>Pe – *iso*-pentyl; CH<sub>2</sub>CH<sub>2</sub><sup>i</sup>Pr

<sup>i</sup>Pr – *iso*-propyl

ITRS – International Technology Roadmap for Semiconductors

MOSFET – metal-oxide-semiconductor field effect transistor

<sup>n</sup>Pe – n-pentyl

<sup>n</sup>Bu – n-butyl

Nep – neopentyl; CH<sub>2</sub>CMe<sub>3</sub>

NMR – Nuclear Magnetic Resonance

nor – norbornyl

<sup>n</sup>Pr – n-propyl

PEALD – Plasma Enhanced Atomic Layer Deposition

pftb – perfluoro *tert*-butoxide

PXRD – Powder X-Ray Diffraction

QCM – Quartz Crystal Microbalance

<sup>s</sup>Bu – *sec*-butyl; CHMeEt

SCXRD – Single Crystal X-Ray Diffraction

SMT – semiconductor to metal transition

<sup>s</sup>Pe – *sec*-pentyl; CH(Me)CH<sub>2</sub>CH<sub>2</sub>Me

<sup>t</sup>Bu – *tert*-butyl

<sup>t</sup>BuO-Bpin – 2-*tert*-butoxy-4,4,5,5-tetramethyl-1,3,2-dioxaborolane

TFT – thin film transistors

TGA – Thermogravimetric Analysis

thd – 2,2,6,6-tetramethylheptane-3,5-dionate

THF – Tetahydrofuran

<sup>t</sup>Pe – *tert*-pentyl; CMe<sub>2</sub>Et

## Declaration of Academic Achievement

Dr. Jeffrey S. Price, and PhD candidate Novan A. G. Gray assisted in the acquisition of SCXRD data for  $[\text{CrCl}(\text{pftb})_2(\text{THF})_3]$  (**5**), and  $\text{K}[\text{V}(\text{pftb})_4]$  (**6**). Dr. Jeffrey S. Price assisted in the refinement and structure solution for complexes **5** and **6**. PhD candidate Majeda Al-Hareri assisted in the acquisition of PXRD data for  $[\text{Cr}(\text{O}^t\text{Bu})_4]$  (**1**), and  $[\text{V}(\text{O}^t\text{Bu})_4]$  (**2**). All other results were obtained by Aya Kadri, including the synthesis of new complexes **5** and **6**. To the best of the author's knowledge, this work does not infringe any copyrights and is the sole work of the author.

# 1 Introduction

Semiconductors are materials that exhibit electrical conductivity properties in between that of a conductor and an insulator. The development and observations of semiconducting materials dates to the early 19<sup>th</sup> century with the discovery of the Seebeck effect. In 1821, Thomas Jonathan Seebeck observed that a compass needle is deflected when two dissimilar metals or semiconducting materials at different temperatures were connected in a closed loop permitting the flow of electrons.<sup>1</sup> The flow of electrons between the two materials, with no external supply of power, resulted in the induction of a magnetic field around the closed loop, deflecting the needle of the compass. This was the first reported observation of the properties of semiconductors. Utilizing the unique properties of semiconductors, the invention of the first transistor was achieved in 1947 by John Bardeen and Walter Brattain.<sup>2</sup> Since then, the advent of silicon based semiconductors has resulted in an industrial revolution in the 1950s for the development of transistors. Moore's law, a speculative observation made in 1998 by Gordon E. Moore, states that the number of transistors on a circuit will double every two years.<sup>3</sup> This prediction has proven to be accurate and the number of transistors in an integrated circuit has followed closely with Moore's law. The most common type of transistor used in modern technology is the metal-oxide-semiconductor field effect transistor (MOSFET).

The manufacturing of a MOSFET is carried out using a doped silicon substrate with two distinct regions; the negatively charged n-type region and the positively charged p-type region.<sup>4</sup> In a MOSFET, the discrete n-type and p-type regions are separated, preventing the flow of electrons. The composition of an N-type top-gate MOSFET is

illustrated in **Figure 1.1**. This MOSFET consists of a p-type substrate that contains two distinct heavily doped n-type regions. These two n-type regions are the source and drain regions of the transistor. Over this substrate an oxide layer is deposited, acting as an insulator; over which a highly conducting metal film is deposited to behave as a gate. A simple P-N junction (the contact area between n-type and p-type regions) would result in the transfer of electrons from areas of high concentration to areas of lower concentration.<sup>4</sup> The diffusion of electrons in a P-N junction will eventually result in a depletion region where the electrons in the n-type region fill the holes in the p-type region (illustrated as negative charges in **Figure 1.1**).<sup>4</sup> Once this depletion region is formed, the transfer of electrons is no longer permitted unless a forward bias is applied to the junction. A positive potential is applied on the gate creating a field effect which induces the movement of holes in the p-type region (illustrated as white holes in **Figure 1.1**) creating a channel region which results in the formation of a depletion region across the channel between the two n-type regions.<sup>4,5</sup> This is the main principle behind the design of field effect transistors (FET). Due to this depletion region, an inversion layer of electrons begins to form over the depletion region which allows the flow of electrons between the two n-type regions.<sup>5</sup> With the application of this gate voltage potential across the source and drain regions, a current will flow through the inversion layer of electrons which can be modulated through the control of the gate voltage (illustrated as an arrow in **Figure 1.1**).<sup>5</sup> With the decrease in distance between the two n-type regions (the source and drain) the probability of quantum tunnelling increases. This phenomenon is known as direct source-to-drain tunneling and is an undesirable effect which was previously thought to be the limit of transistor size reduction.<sup>6</sup> However, IBM announced the production of a 2 nm

transistor in 2021 which would increase performance by 45% at the same power usage in comparison to the 7 nm transistors currently in use.<sup>7</sup>

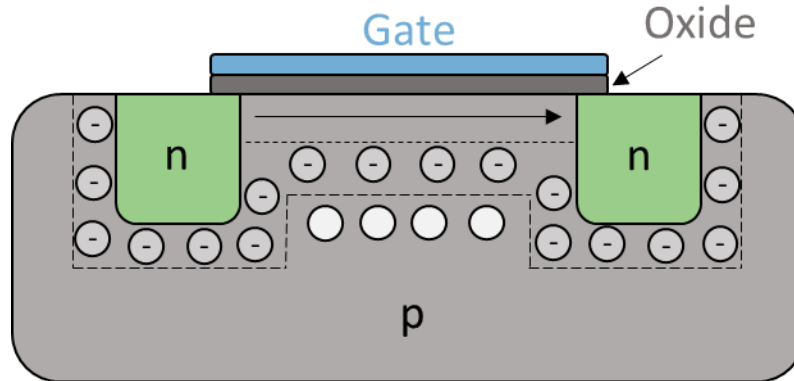


**Figure 1.1** Operation of a N-channel top-gate MOSFET. Electron flow in the inversion layer is depicted by the arrow in the channel region between the source and drain. Dashed lines indicate the depletion region in P-N junction. Charge carrier accumulation upon the application of a gate potential depicted by white circles past the depletion region.

Miniaturization in the semiconductor industry has motivated the development of thin film deposition methods resulting in atomically controlled accuracy. As such, the control of thin films deposited on complex three dimensional morphologies with continuous uniformity is critical. This is the main motivation for using atomic layer deposition (ALD; *vide infra*), as a method for the deposition of uniform films on high aspect ratio morphologies to be used in semiconductor devices such as transistors.

## 1.1 Atomic Layer Deposition

ALD is a chemical vapour deposition (CVD) method that differs from typical deposition methods in that the reactivity between the reagents is self-limiting and the

growth observed for the thin film can be accurately controlled by varying the number of cycles. A typical ALD cycle involves the sequential delivery (in a vacuum reaction chamber containing a heated substrate) of vapours of two reagents, which are commonly referred to as the ALD precursor and the co-reagent. The ALD process occurs under vacuum conditions in order to assist in the volatilization of the precursor and co-reagent.<sup>8</sup> The precursor is a metal complex, and ALD is dependent on the physisorption and/or chemisorption of the precursor on the substrate.<sup>9</sup> The co-reagent reacts with the adsorbed precursor in a way that converts it to the desired material, in the process creating a new surface for further reactivity in the next cycle. All reactions during ALD must be self-terminating, meaning that they proceed until all accessible surface sites have reacted, and then precursor/co-reagent adsorption ceases, so that longer precursor/co-reagent pulses do not afford thicker films. Any by-products of the reaction between the precursor and co-reagent must be volatile so that they can be removed from the substrate through an inert gas purge. A typical ALD cycle is presented in **Figure 1.1.1** illustrating the reactivity between a precursor and co-reagent.

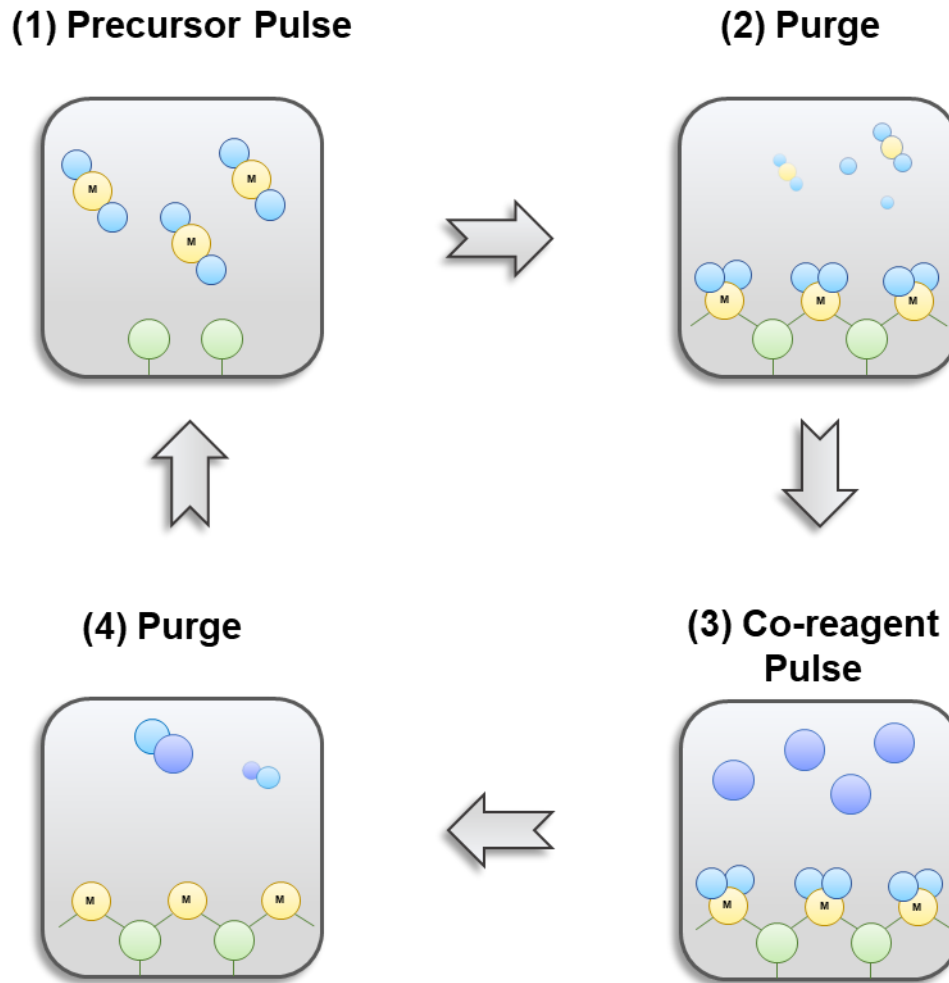


**Figure 1.1.1** Schematic illustration of an ALD cycle (in this case for metal ALD).

Generally, there are two types of ALD: thermal ALD and plasma-enhanced ALD (abbreviated as PEALD). The schematic presented in **Figure 1.1.1** is representative of thermal ALD. In thermal ALD, the co-reagent is a chemically stable species, and the reaction between the precursor and co-reagent is spontaneous at the deposition temperatures employed without the assistance of plasma.<sup>10</sup> Typical co-reagents used in thermal ALD include oxygen gas, ammonia, and water,<sup>11-15</sup> affording metal oxides and nitrides such as ZnO, TiN, TiO<sub>2</sub>, and HfO<sub>2</sub>.<sup>16-19</sup> The deposition of a single element through thermal ALD is more challenging, especially in the case of electropositive

metals.<sup>10</sup> Such films are more readily deposited using plasma ALD, typically using hydrogen plasma, where plasma generated hydrogen atoms reduce the metal in a precursor molecule to its elemental state. However, due to the high probability of radical recombination, self-limiting growth can be difficult to achieve on high aspect ratio morphologies. This is due to the attenuation of the supply of radicals in less accessible regions of the substrate such as at the bottom of trenches.<sup>10,20</sup> Additionally, the use of plasma adds to the manufacturing cost of the thin films in comparison to the costs when thermal ALD is employed.<sup>21</sup> The development of new methods for thermal ALD of pure elements is therefore required, especially in the case of elements (including Cr and V) which have not previously been accessed by thermal ALD, or can only be deposited under conditions that would limit industrial application.

A unique feature of ALD is the control of film thickness solely through the number of ALD cycles employed. In CVD, the precursors used to deposit the thin film either undergo decomposition or reactivity with co-reagents, producing thin films with non-uniform thickness and poor conformality. This is because the growth of the thin films is dependent on the flux and the exposure of the surface to the precursor. The difference between films grown using ALD and other vapour deposition methods is depicted in **Figure 1.1.2**. The flux controlled growth is typical of surface diffusion-controlled methods such as PVD and CVD. Deposition in these methods is not surface saturation-dependent, and continuous non-conformal growth of the thin film is typical.

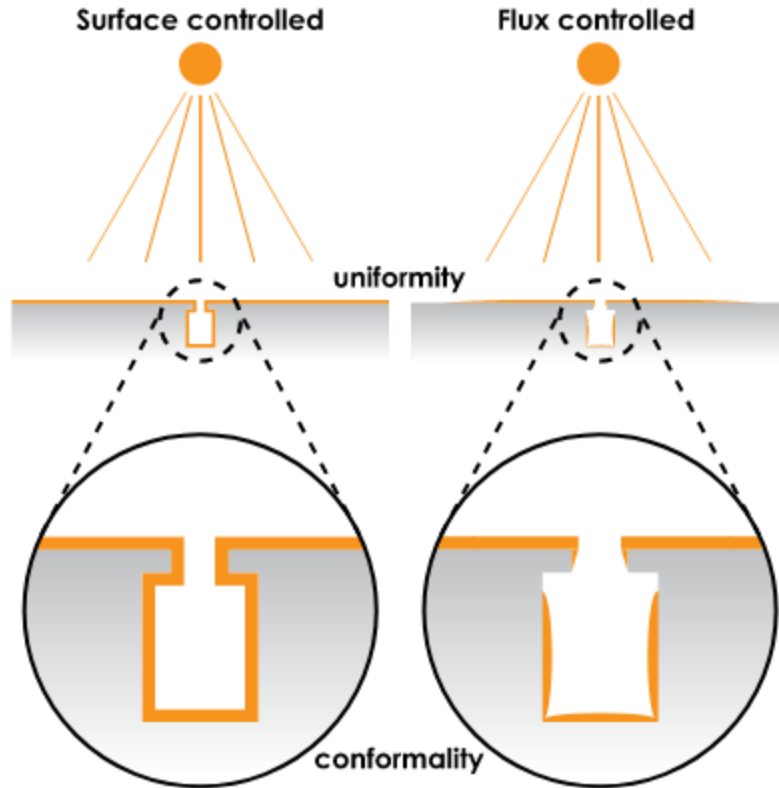


**Figure 1.1.2** Surface and flux controlled growth in a via; highlighting the difference in film conformality between ALD (left) and CVD/PVD (right). Figure adapted from H. Knoops.<sup>22,23</sup> Licensed under Creative Commons.

One of the main necessities for conformal growth in ALD is the sufficient supply of precursor to the surface for adsorption to occur. The surface coverage of a substrate is dependent on the irreversible adsorption of gas phase molecules on that surface. This is termed as the sticking probability ( $s$ ), and in the Langmuir model, the self-terminating surface coverage is modeled by Equation 1 where  $s_0$  depicts the initial sticking probability and the total surface coverage is denoted by  $\theta$  (ranging from 0 to 1).<sup>24</sup>

$$s = s_0(1 - \theta) \quad \text{Equation 1}$$

The initial sticking probability term varies based on the ALD process employed and can range from  $10^{-5}$  to  $10^{-1}$  which translates to 10 to 100,000 collisions of a molecule with the surface before irreversible adsorption occurs.<sup>25</sup> When surface saturation occurs,  $\theta$  is equal to 1 and the sticking probability ( $s$ ) is equal to zero, indicating no further adsorption can occur, limiting the thin film growth to a single monolayer. Due to this constraint, thin film growth by ALD should increase linearly with each cycle of precursor and co-reagent. However, experimentally, delayed growth is commonly observed.<sup>22,26-29</sup> There are three possible growth rates attainable by ALD; delayed growth rate (or substrate-inhibited), accelerated growth rate (or substrate-enhanced), and linear growth rate. The relation of these three growth rates with respect to the number of ALD cycles is illustrated in **Figure 1.1.3**.

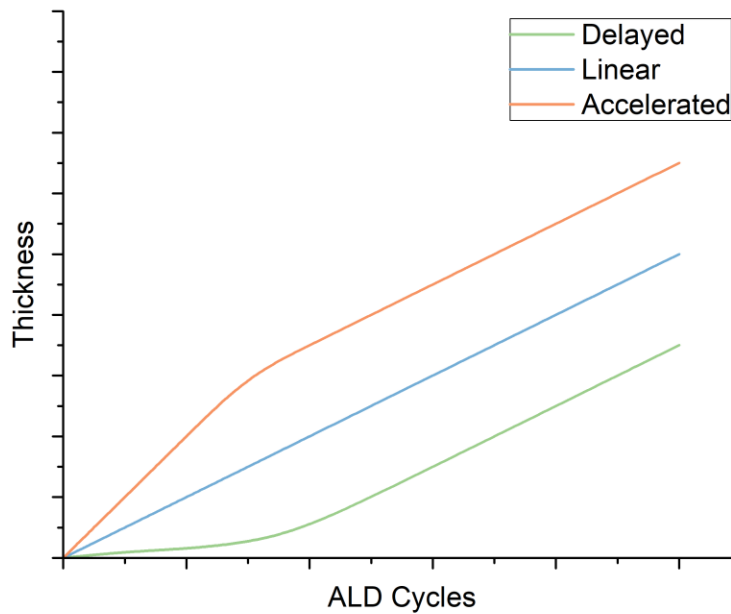


**Figure 1.1.3** Film thickness as a function of ALD cycles with emphasis on the different rates of growth.

The nature of the exposed surface of the substrate determines the growth dependency. In accelerated growth, the physisorption and chemisorption of the precursor occurs to a greater extent on the substrate than that on the surface of the growing film, permitting the growth of higher thickness films within the initial few ALD cycles. This property of accelerated growth has been utilized for area-selective deposition. In delayed growth, precursor adsorption is more favourable on the surface of the newly deposited material than the surface of the substrate, so the thickness increases slowly within the first few cycles of deposition. This often results in less conformal films and the development of island growth. As previously mentioned, this is dependent on the sticking probability onto the substrate (Equation 1). In thermal ALD (where co-reagent recombination

probability does not play a role in film growth), thin film growth and conformality is governed by two systems: surface reaction-limited growth and diffusion-limited growth. The difference in thin film growth between these two systems is illustrated in **Figure 1.1.4**.

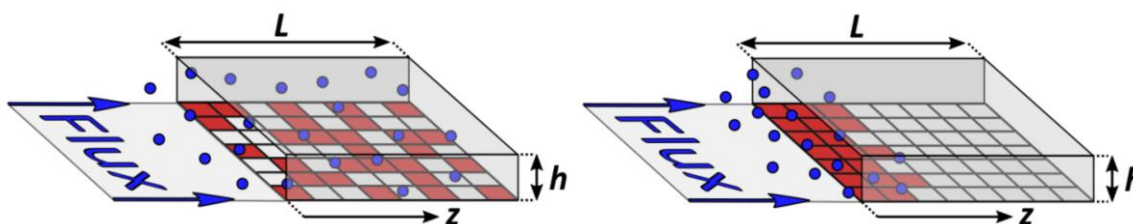


**Figure 1.1.4** Comparison of reaction-limited growth (left) and diffusion-limited growth (right) in a high aspect ratio morphology.<sup>25</sup> Licensed under Creative Commons.

The difference between reaction-limited and diffusion-limited ALD growth lies in the time scales required for surface adsorption or diffusion to occur. If adsorption occurs rapidly, thin film growth is governed by diffusion-limited growth, where molecules adsorb to the surface before the pulse of the reagent has reached the rest of the surface.<sup>30</sup> If the adsorption does not occur rapidly, film growth is governed by the rate of the surface reactions.<sup>30</sup> These two different growth regimes can potentially be controlled by the substrate temperature. In general, there is weak dependency of film growth rate per cycle (GPC) on the substrate temperature in ALD as compared to CVD, although this is not always the case.<sup>29</sup> For example, the GPC for ZnO ALD using  $\text{ZnEt}_2$  and  $\text{H}_2\text{O}$  is strongly temperature dependent.<sup>31</sup> Nevertheless, when the temperature dependence of ALD is low, as is often the case, the range of temperatures giving rise to a constant GPC is referred to as the “ALD window”.<sup>32</sup> At temperatures below the ALD window, non-ALD behaviour can occur because there is a higher probability of condensation of the

precursor on the surface, leading to a thicker film.<sup>25,33</sup> Alternatively, non-ALD behaviour can occur at low temperatures due to a lesser degree of reactivity between the precursor and co-reagent, limiting the growth rate of the film.<sup>33,34</sup> At higher temperatures, the decomposition of the precursor on the surface is much more probable and can lead to CVD growth, rather than ALD. Alternatively, higher temperatures can promote the desorption of the precursor from the surface, decreasing the GPC.<sup>33,34</sup> The “ALD window” refers to the range of temperatures where none of the aforementioned phenomena occur, and the film growth rate is only limited by the surface-based self-terminating reactivity.

A unique characteristic of ALD in comparison to CVD is the saturation of the growth per cycle with prolonged precursor pulsing (previously discussed as surface saturation in Equation 1). With the prolonged dosing of a precursor or co-reagent in an ALD cycle, the surface coverage ( $\theta$  in Equation 1) approaches a value of 1 indicating complete surface coverage.<sup>27</sup> In contrast, a value of  $\theta > 1$  is typically representative of CVD type growth.<sup>27</sup> The relationship between available surface sites and the GPC is presented in **Figure 1.1.5**.

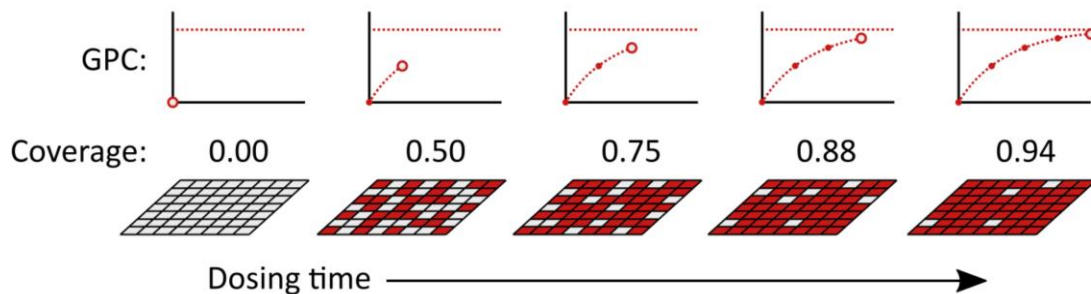


**Figure 1.1.5** Relationship between increasing dosage time and surface coverage ( $\theta$ ) resulting in a constant GPC due to surface saturation.<sup>25,27</sup> Licensed under Creative Commons.

In ALD, as saturation is approached, the GPC plateaus to a constant GPC, indicating the lack of remaining available surface reactive sites within each ALD cycle. The quantity of precursor required to saturate the surface and achieve a constant GPC is referred to as the saturative dose.<sup>35</sup> The amount of time required to achieve the saturative dose is correspondent to the point where a constant GPC is achieved, as depicted in **Figure 1.1.6**. By contrast, for CVD, the GPC increases linearly with increasing exposure of the surface to the precursor. The amount of material deposited and the resulting film thickness in CVD is a function of the exposure time, since no self-terminating reactivity occurs.<sup>32</sup>

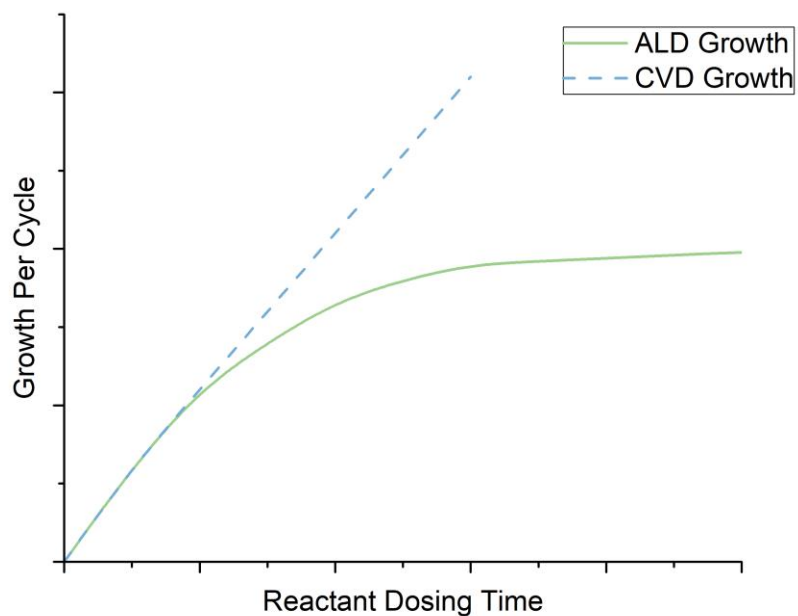


**Figure 1.1.6** Saturation curve of the growth per cycle of the deposited film as a function of reactant dosing time, illustrating the difference between CVD and ALD type growth.

From this discussion, it is evident that in contrast to other deposition methods such as PVD or CVD, ALD can afford highly uniform and conformal thin films of reproducible thickness, even on complex three-dimensional structures with high aspect ratios.

Development of an ALD process requires numerous considerations. A suitable combination of precursor and co-reagent displaying the desired reactivity is essential. Additionally, tuning and design of the precursor containing the desired element(s) to be deposited is critical for the development of a viable ALD process. The desirable characteristics of an ALD precursor are discussed below.

## 1.2 Properties of Potential ALD Precursors

In the earlier years of ALD, precursors were often sourced from successful CVD methods, and the deposition conditions were adapted to achieve self-terminating reactivity.<sup>36</sup> However, they are now often designed specifically for ALD. There are three major characteristics an ALD precursor must display: (1) volatility, (2) thermal stability, and (3) reactivity.<sup>37</sup>

The precursor must be sufficiently volatile at reduced pressures such that gas phase molecules can be delivered to the substrate surface for deposition, without decomposition, and with sufficient flux. Ideally, the precursor will be a liquid at the delivery (bubbler) temperature with a low volatilization temperature. Liquid precursors are advantageous because they (a) avoid particle incorporation in the thin film, and (b) provide a more consistent rate of precursor volatilization compared to solid precursors, where precursor volatilization rate is greatly affected by particle size.

An ideal vapour pressure for an ALD precursor is around 0.1 Torr.<sup>38</sup> Based on the Knudsen-Langmuir vapour pressure equation, the vapour pressure is inversely proportional to the square root of the molecular weight of the compound as presented in Equation 2.<sup>39</sup> In this equation,  $\frac{\Delta m}{\Delta t}$  is the rate of mass loss per unit surface area,  $\alpha_1$  is the vapourization coefficient (this value is unique to the instrumental parameters),  $T$  is the temperature at which volatilization occurs,  $R$  is the universal gas constant, and  $MW$  is the molecular weight of the complex.

$$p = \frac{\Delta m}{\alpha_1 \Delta t} \sqrt{\frac{2\pi RT}{MW}} \quad \text{Equation 2}$$

Based on this equation, it can be rationalized that lower molecular weight complexes are desirable, so that sufficient volatility is achieved. As such, monomeric ALD precursors are often more desirable than oligomers. Additionally, it is preferable to choose complexes that display limited intermolecular interactions such as hydrogen bonding or  $\pi$ -stacking, which decrease the volatility of the precursor.<sup>40</sup> The ligand choice is essentially what determines the volatility of the metal complexes. As a general rule, lower molecular weight and less symmetric compounds tend to be particularly volatile.<sup>22</sup> Higher volatility can often be achieved through the design of a heteroleptic precursor, although exceptions to this rule are possible.<sup>22</sup>

A method used in the Emslie group to estimate the delivery (bubbler) temperature required for a new precursor on one of the Emslie group's ALD reactors (which operate at around 250 mTorr) is to determine the sublimation temperature under high vacuum (10 mTorr) and add 40 °C to this temperature. A more quantitative method to assess the volatility (and thermal stability) of a precursor is through thermogravimetric analysis (TGA), although it is important to note that TGA measurements are typically carried out at a pressure of 760 Torr, which is far higher than that in an ALD reactor (typically 0.1 – 1.0 Torr). In a TGA experiment, a sample of the precursor is loaded to a pan and is heated at a specified ramp rate while the mass of the sample is recorded. An ideal ALD precursor would volatilize completely without any residual mass as the temperature is increased. The residual mass percentage ( $\%m_{res}$ ) is defined as the mass remaining in the pan after volatilization is completed. A zero residual mass percentage would indicate that the entirety of the mass loaded onto the pan has volatilized. Conversely, if some decomposition of the sample occurs as the sample is heated, this results in mass

decrease(s) associated with decomposition and loss of volatile decomposition products. Thermal decomposition of metal complexes also often affords non-volatile products resulting in residual mass. Mass changes due to decomposition (if precursor decomposition occurs without concurrent precursor volatilization) can provide insight into the possible decomposition pathways of the precursor, as the mass loss percentage with respect to the molecular weight of the precursor can allow the determination of the components lost during decomposition/volatilization, especially when TGA by-products are monitored by mass spectrometry. A non-zero residual mass does not eliminate the possibility of using the precursor for ALD, because volatilization in an ALD reactor will occur at far lower temperatures than in TGA, due to the lower pressure.

The precursor must also display sufficient thermal stability such that volatilization to the substrate is possible without any decomposition. Thermal stability is required at the delivery (bubbler) temperature on a timescale of weeks to months, and at the substrate temperature on a timescale of seconds. Decomposition of the precursor on the substrate surface would result in CVD growth, and may also lead to the introduction of contaminating species; both of which are undesirable features.<sup>38</sup> Organometallic compounds such as metal alkyl or metal carbonyl complexes display high reactivity and volatility. However, the low bond energy of many transition metal M–C bonds can result in low thermal stability, and transition metal ALD precursors featuring M–C bonds are uncommon.<sup>22</sup> By contrast, metal alkoxides and metal alkylamides have been employed for ALD with high success.<sup>41–43</sup> Metal alkoxides generally exhibit lower reactivity than metal alkyls, and complexes with sterically unencumbered alkoxide groups (e.g. methoxide) tend to oligomerize, which is unfavourable for ALD.<sup>22</sup> However, with larger

alkoxide groups, oligomerization is limited, and the complexes are generally more thermally stable than metal alkyl complexes, especially for alkoxide ligands lacking  $\beta$ -hydrogen atoms (e.g. *tert*-butoxide). However, more sterically bulky ligands could also hinder adsorption of the precursor to the surface, which could limit ALD growth.

The precursor must be chemically reactive towards the substrate surface, and the surface of the growing film. With higher reactivity towards the surface, a higher GPC can potentially be achieved at a lower deposition temperature. Additionally, any reactivity between the precursor and co-reagent should be thermodynamically favourable at the deposition temperature, and the by-products of their reaction should be volatile, such that film contamination is limited. An ideal ALD precursor would possess all three of the aforementioned qualities; high volatility, high thermal stability, and high reactivity with a selected co-reagent, resulting in volatile by-products.

Taking the aforementioned qualities of an ideal ALD precursor into consideration, the focus of this thesis is on developing homoleptic vanadium and chromium alkoxide ALD precursor candidates and exploring their suitability for ALD of chromium and vanadium metal. Initial work is focused on the *tert*-butoxide ligand because the  $[M(O^iBu)_4]$  ( $M = Cr, V$ ) complexes are already known, and the steric bulk of the *tert*-butoxide ligands is sufficient to prevent oligomerization. It was hypothesized these complexes would exhibit reactivity towards hydrosilanes and hydroboranes, as will be discussed in Sections 1.4 and 1.5.

### 1.3 Solution State Reactivity Analyses

As an initial test of the suitability of a new precursor/co-reagent combination, solution state reactivity studies can be employed to predict the likelihood of potential surface reactions during ALD. These studies can assist in identifying potential by-products of the reactions, through which the reaction mechanism can be inferred. This is an effective screening tool that can assist in determining the most promising combinations of precursor and co-reagent, cutting down on the time and cost associated with screening a range of potential precursors and co-reagents on an ALD tool. The soluble reaction by-products are monitored by NMR spectroscopy and any precipitated material (such as elemental metal) can be characterized by powder X-ray diffraction (PXRD) for identification.

Typically, these experiments are conducted on a small scale and in a deuterated solvent such as  $C_6D_6$ . A precursor candidate complex and a co-reagent are combined in a J-Young tube and any reactivity is monitored by NMR spectroscopy. If reactivity is not observed at room temperature, the reaction mixture is monitored for 24 hours at a higher temperature (e.g. 20-60 °C higher) until reactivity is observed, or until no reactivity is observed at 100 °C. Any reactivity that is slow at 100 °C is unlikely to occur rapidly (in seconds) at the substrate surface during ALD, at least not at moderate ALD temperatures (e.g. < 200 °C). If the co-reagent reacts rapidly (e.g. within seconds) with the precursor candidate in solution at low temperature (e.g. room temperature), then this combination is more likely to result in the successful development of a new ALD process.

## 1.4 Homoleptic Vanadium Alkoxide Complexes

In 1962, Bradley and Mehta synthesized numerous homoleptic vanadium(IV) alkoxides through the alcoholysis of  $[V(NEt_2)_4]$ .<sup>44</sup> The tetrakis(diethylamino)vanadium species was prepared through the reaction of  $VCl_4$  with  $LiNEt_2$ . This was then followed by the reaction with the appropriate alcohol to yield the corresponding vanadium tetraalkoxide. They noted that although the synthesis of these compounds is possible, they exhibit some instability (possibly due to their high air and moisture sensitivity) which is dependent on the degree of substitution of the alkoxide group (primary, secondary, or tertiary).<sup>44</sup> The properties of nine primary vanadium alkoxides (R = Me, Et, <sup>n</sup>Pr, <sup>n</sup>Bu, <sup>i</sup>Bu, <sup>n</sup>Pe, <sup>i</sup>Pe, <sup>act</sup>Pe, and Nep) were analyzed.<sup>44</sup> Vanadium tetramethoxide and tetraethoxide were isolated as brown solids, vanadium tetraneopentyloxide as a green solid, and all other compounds were isolated as dark brown liquids.<sup>44</sup> With the exception of vanadium tetramethoxide, all synthesized primary alkoxides were isolated by vacuum distillation/sublimation.<sup>44</sup> Vanadium tetramethoxide did not undergo sublimation at 200 °C at reduced pressure (50 mTorr) and underwent decomposition at higher temperatures.<sup>44</sup> The molecular weights of the primary complexes synthesized were assessed by ebullioscopic determination.<sup>44</sup> These measurements indicated that only  $V(ONep)_4$  was monomeric in nature, and interestingly, vanadium tetramethoxide was determined to be trimeric.<sup>44</sup> The degree of oligomerization was observed to decrease with increasing branching and steric bulk.<sup>44</sup>

Bradley and Mehta then diverted their attention to secondary alkoxides (R = <sup>i</sup>Pr, <sup>s</sup>Bu, <sup>s</sup>Pe,  $CHMe^iPr$ , and  $CHEt_2$ ).<sup>44</sup> Vanadium tetrakisopropoxide was isolated as a green solid and all other complexes were isolated as green liquids.<sup>44</sup> All secondary alkoxide

complexes were significantly more volatile than the primary alkoxide complexes.<sup>44</sup> Although a degree of oligomerization of 1.17 was calculated for vanadium tetraisopropoxide, the authors declared the complex to be a monomer and attributed the higher degree of oligomerization (measured by ebullioscopic molecular weight determination) to be due to loss of some of the complex by evaporation during the measurement.<sup>44</sup>

Finally, Bradley and Mehta explored the properties of tertiary alkoxides ( $R = {}^t\text{Bu}$ ,  $\text{CEtMe}_2$ ,  $\text{C}^n\text{PrMe}_2$ ,  $\text{C}^i\text{PrMe}_2$ ,  $\text{CEt}_3$ , and  $\text{CMeEt}^n\text{Pr}$ ).<sup>44</sup> All of these vanadium complexes were isolated as liquids, with  $[\text{V}(\text{O}^t\text{Bu})_4]$  as a blue liquid and the others as dark green liquids.<sup>44</sup> All tertiary complexes were determined to be monomeric through ebullioscopic molecular weight determination.<sup>44</sup> Of these complexes,  $[\text{V}(\text{O}^t\text{Bu})_4]$  exhibited the highest volatility.<sup>44</sup>

An interesting property of many vanadium alkoxides is their thermochromic behaviour. Soares *et al.* reported the synthesis of numerous vanadium alkoxides that exhibit thermochromic properties.<sup>45</sup> Most interestingly, they discovered that the vanadium(IV) tetraisopropoxide and vanadium tetraneopentyloxy complexes that were previously reported by Bradley and Mehta to be monomeric in solution, to be dimeric in the solid state by single crystal X-ray diffraction (SCXRD).<sup>45</sup>  $[\text{V}_2(\text{O}^i\text{Pr})_8]$  along with  $[\text{V}_2(\text{O}^s\text{Bu})_8]$ ,  $[\text{V}_2(\text{OCy})_8]$ , and  $[\text{V}_2(\text{ONep})_8]$  all exhibited thermochromic behaviour in solution when the temperature was varied from  $\geq 370 \text{ K}$  to  $< 200 \text{ K}$ .<sup>45</sup> However, more bulky  $[\text{V}(\text{O}^t\text{Bu})_4]$  and  $[\text{V}(\text{O}^t\text{Pe})_4]$  did not exhibit any thermochromic properties.<sup>45</sup> The authors observed an isosbestic point in the electronic spectra of  $[\text{V}_2(\text{ONep})_8]$  (indicative

of an equilibrium) and attributed the thermochromic behaviour of the complexes to be due to an equilibrium between the monomeric and dimeric species.<sup>45</sup>

For the purposes of this study, a highly volatile and thermally robust vanadium alkoxide complex is desirable and,  $[V(O^iBu)_4]$  was chosen due to its documented volatility and anticipated reactivity. In the reactions with a hydrosilane/hydroborane co-reagent, the vanadium alkoxide is expected to be fully reduced to its elemental state through the formation of an intermediary vanadium hydride species ( $VH_x$ ), which reductively eliminates hydrogen gas to result in the zero oxidation state metal center. This reaction pathway is discussed in further detail in Section 2.1, but it is worthwhile to consider at this point the nature and thermal stability of known homoleptic vanadium hydride species.

There is precedent in the literature for the theoretical usage of vanadium hydrides for hydrogen fuel storage<sup>46,47</sup> or as a catalyst in the Haber-Bosch process.<sup>48</sup> The first reported synthesis of stoichiometric  $VH_2$  was by Reilly and Wiswall in 1970 through the heating of vanadium metal to 450 °C under a pressure of 100 PSI of hydrogen gas atmosphere.<sup>49</sup> However,  $VH_2$  was found to be unstable at room temperature and pressure, and resulted in the slow evolution of hydrogen gas.<sup>49</sup> Vanadium hydrides are often formed in non-stoichiometric ratios due to the integration of hydrogen atoms within the vanadium crystal lattice rather than the formation of chemical bonds.<sup>48,50</sup> Maeland reported three distinct crystalline phases with varying hydride composition (body centered cubic for  $VH_{0.05}$ , body centered tetragonal for  $VH_{0.46}$  to  $VH_{0.90}$ , and a two-phase region for hydride compositions up to  $VH_{1.8}$ ) all of which exhibited decomposition and evolution of hydrogen gas at room temperature and pressure.<sup>49,51</sup>

## 1.5 Homoleptic Chromium Alkoxide Complexes

Most of the research that was conducted on synthesizing chromium alkoxides occurred between 1950 and 1990.<sup>53-58</sup> Limited information on the structural characteristics of these chromium alkoxides is available, as crystal structures were seldom reported. They were mostly characterized by elemental analysis, solubility, solid-state magnetic susceptibility measurements, and cryoscopic molecular weight determination.<sup>53,59</sup>

The most stable oxidation states of chromium are Cr(II) and Cr(III).<sup>60</sup> It wasn't until 1971 when Newing reported the synthesis of  $\text{Cr}(\text{O}^t\text{Bu})_2$  and  $\text{Cr}(\text{OMe})_2$  through the alcoholysis reaction of  $[\text{Cr}[\text{N}(\text{SiMe}_3)_2]_2(\text{THF})_2]$  that the accessibility of these complexes was readily achieved.<sup>53</sup> In 1979, Horvath and Horvath reported the synthesis of numerous Cr(II) alkoxides through this pathway with varying R groups which they characterized by elemental analysis, reflectance spectroscopy, solubility, and chemical behaviour.<sup>53</sup> They reported that all primary chromium(II) alkoxides ( $\text{R} = \text{Me}, \text{Et}, ^n\text{Pr}, 1\text{-pentyl}, \text{and } ^n\text{Bu}$ ) (with the exception of  $\text{Cr}(\text{OMe})_2$  which was violet) to be yellow or orange, all secondary chromium(II) alkoxides ( $\text{R} = ^i\text{Pr}, ^s\text{Bu}, 2\text{-pentyl}, \text{and } 3\text{-pentyl}$ ) to be purple or violet, and all tertiary alkoxides ( $\text{R} = ^t\text{Bu}, 1\text{-adamantyl}, \text{CET}_3, \text{and } \text{CPh}_3$ ) to be blue.<sup>53</sup> They determined the product isolated by Newing through this synthetic avenue, namely:  $\text{Cr}(\text{OMe})_2$ , to be polymeric in nature.<sup>52,53</sup> In 1990, Mahendra and Mehrotra reported the synthesis of  $\text{Cr}(\text{OR})_3$  ( $\text{R} = \text{Me}, \text{Et}, \text{and } ^n\text{Bu}$ ) through the reaction of  $[\text{CrCl}_3(\text{THF})_3]$  with the corresponding lithium alkoxide.<sup>61</sup>  $\text{Cr}(\text{OMe})_3$  was reported as a grey blue solid, and all others as grey green solids.<sup>61</sup> In their attempts to synthesize  $[\text{Cr}(\text{O}^t\text{Bu})_3]$ , they noted the formation of a soluble blue complex that was identified as the previously reported

[Cr(O<sup>t</sup>Bu)<sub>4</sub>].<sup>61</sup> Characterization of the chromium(III) complexes was done through elemental analysis, IR spectroscopy, and electron absorption spectroscopy.<sup>61</sup>

The first reported synthesis of [Cr(O<sup>t</sup>Bu)<sub>4</sub>] was by Hagihara and Yamazaki in 1959.<sup>57</sup> They accomplished this synthesis through the reaction of bis(benzene)chromium with di-*tert*-butyl peroxide in a sealed vessel at 90 °C for 20 hours.<sup>57</sup> They reported a melting point of 30-35 °C for the deep blue crystals that were isolated by sublimation (at 70-90 °C under reduced pressure).<sup>57</sup> An improved synthetic route was achieved by Caulton *et al.* in 1988 using [CrCl<sub>3</sub>(THF)<sub>3</sub>] with four equivalents of KO<sup>t</sup>Bu and one equivalent of CuCl as an oxidizing agent.<sup>59</sup> Numerous other chromium alkoxides were synthesized by Bradley *et al.* in 1971.<sup>55</sup> Namely: [Cr(O<sup>t</sup>Bu)<sub>2</sub>(OCMe<sub>2</sub>Et)<sub>2</sub>], [Cr(OCMeEt<sub>2</sub>)<sub>4</sub>], and [Cr(OCEt<sub>3</sub>)<sub>4</sub>].<sup>55</sup> However, [Cr(O<sup>t</sup>Bu)<sub>4</sub>] displayed the highest volatility among these chromium alkoxides.<sup>55</sup>

Based on the attractive volatility of [Cr(O<sup>t</sup>Bu)<sub>4</sub>], this complex was chosen as a potential ALD precursor in this research. Reactions of this complex with hydrosilanes or hydroboranes are expected to generate an intermediary chromium hydride species which would undergo reductive elimination of hydrogen gas to afford elemental chromium. Therefore, the accessibility and thermal stability of homoleptic chromium hydride species is outlined below. Three binary chromium hydrides have been prepared in the condensed phase: CrH, Cr<sub>2</sub>H<sub>3</sub>, and CrH<sub>2</sub>.<sup>62,63</sup> However, the latter two hydride species are only stable under very high pressures; above 17 and 24 GPa of H<sub>2</sub>, respectively.<sup>62</sup> CrH has also been isolated at room temperature under inert atmosphere utilizing electrodeposition, but is reported to be unstable towards slow loss of H<sub>2</sub>.<sup>63</sup>

## 1.6 Deposition of Vanadium- and Chromium-Containing Thin Films by ALD

To the best of the author's knowledge, there is no ALD method for the deposition of elemental vanadium thin films to date. Films of VO<sub>2</sub> and V<sub>2</sub>O<sub>5</sub> have been grown by ALD using vanadium precursors such as [VCl<sub>4</sub>],<sup>64</sup> [VOCl<sub>3</sub>],<sup>65</sup> [VO(acac)<sub>2</sub>],<sup>66</sup> [VO(thd)<sub>2</sub>] (thd = 2,2,6,6-tetramethylheptane-3,5-dionate),<sup>67</sup> [V(NEtMe)<sub>4</sub>],<sup>68-70</sup> and [V(NMe<sub>2</sub>)<sub>4</sub>].<sup>71</sup> The deposition of vanadium oxide thin films by ALD is achieved with the use of water, oxygen, or ozone as co-reagents.<sup>71</sup> Generally, the deposited vanadium oxide thin films are amorphous, and are treated with a post deposition annealing procedure which produces a monoclinic crystalline phase.<sup>64</sup> This is done by heating the thin film to temperatures greater than 500 °C under an atmosphere of forming gas (dilute H<sub>2</sub> in N<sub>2</sub>) for one hour.<sup>64</sup> In addition to inducing crystallinity, this post deposition annealing procedure also removes any possible residual contaminants from the thin film.<sup>64,70-72</sup>

VO<sub>2</sub> thin films exhibit a reversible semiconducting to metal transition (SMT) at 68 °C which can be cycled over a million times without any degradation to the quality of the film.<sup>64,71</sup> This thermally induced transition results in changes in the optical properties of the material (thermochromism) making VO<sub>2</sub> thin films favourable as potential optical or electrical switches that could be used for applications such as smart windows.<sup>64,73</sup> Another promising application of vanadium oxide thin films is their use in lithium-ion batteries as potential cathode materials with favourable electrochemical properties.<sup>69,74-76</sup>

Only one report of elemental chromium ALD has been developed by Winter *et al.*<sup>77</sup> The authors reported a multitude of metal complexes containing  $\alpha$ -imino alkoxide ligands as potential precursors, and tested their reactivity in solution with BH<sub>3</sub>(NHMe<sub>2</sub>)

as a co-reagent.<sup>77</sup> The chromium complex that was used to develop an ALD process was  $[\text{Cr}(\text{Me}^t\text{BuCOCN}^t\text{Bu})_2]$ .<sup>77</sup> This complex sublimed at 115 °C (50 mTorr) and decomposed at 230 °C.<sup>77</sup> Self-limiting ALD growth was observed, and a GPC of 0.08 Å/cycle at a deposition temperature of 180 °C was obtained.<sup>77</sup> The ALD window for this process was determined to be between 170-185 °C.<sup>77</sup> However, growth was only observed on a ruthenium coated substrate (5 nm Ru/100 nm SiO<sub>2</sub>/Si), and only after an initial nucleation promoting procedure that involved the pulsing of the precursor for 50 cycles of 20 second pulses.<sup>77</sup> The requirement for prolonged pulses during the nucleation promoting procedure indicates limited physisorption of the precursor to the substrate, suspected to be due to sterically hindered access to the chromium metal center. An interesting phenomenon observed during the development of this ALD process is the plateau obtained in the thickness of the chromium thin film after 1000 ALD cycles.<sup>77</sup> **Figure 1.6.1** presents the thickness of the chromium thin films obtained as a function of the number of ALD cycles. This phenomenon was rationalized by the authors to be due to some catalytic activity by ruthenium, which permitted the activation of the co-reagent.<sup>77</sup> The limited film growth at higher film thickness was rationalized as a consequence of inaccessible ruthenium activation sites.<sup>77</sup>

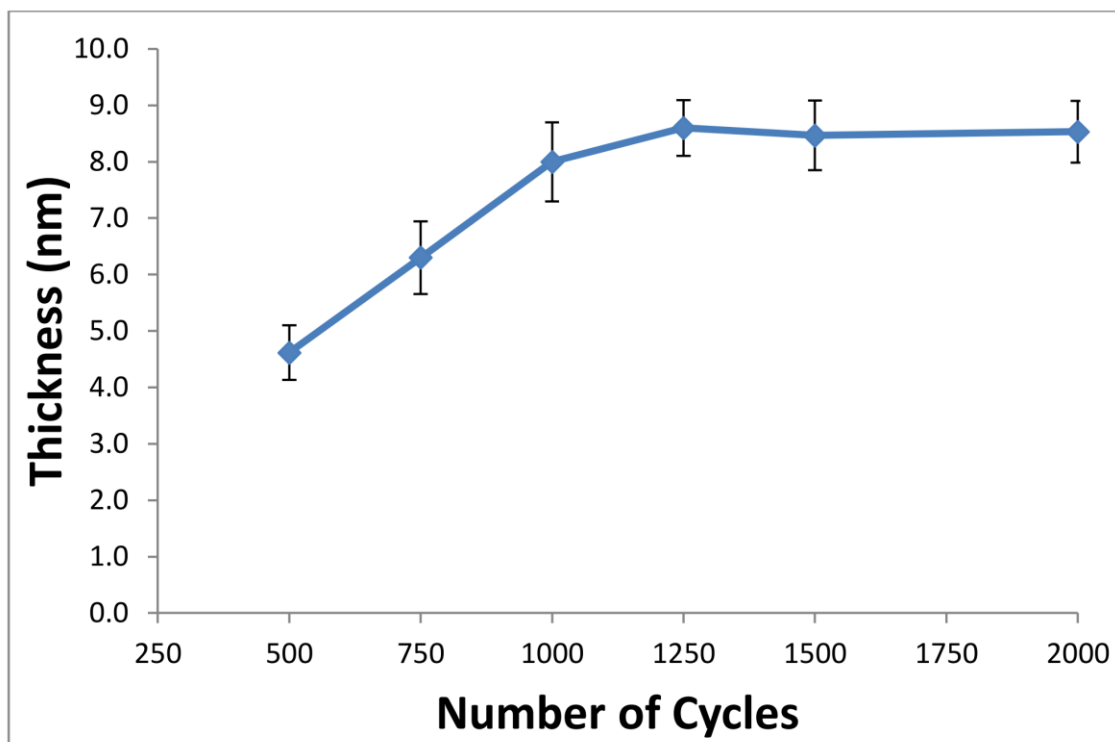


**Figure 1.6.1** Chromium film thickness obtained with respect to the number of ALD cycles at a deposition temperature of 180 °C indicating a plateau past 1000 ALD cycles. Reproduced with permission from Kalutarage, L. C.; Martin, P. D.; Heeg, M. J.; Winter, C. H. Volatile and Thermally Stable Mid to Late Transition Metal Complexes Containing  $\alpha$ -Imino Alkoxide Ligands, a New Strongly Reducing Coreagent, and Thermal Atomic Layer Deposition of Ni, Co, Fe, and Cr Metal Films. *J. Am. Chem. Soc.* **2013**, 135, 34, 12588–12591.<sup>77</sup>

Despite the success of growing thin films of elemental chromium by ALD achieved by Winter *et al.*, the volatility and surface reactivity of  $[\text{Cr}(\text{Me}^t\text{BuCOCN}^t\text{Bu})_2]$  is limited. As previously discussed in Section 1.5,  $[\text{Cr}(\text{O}^t\text{Bu})_4]$  exhibits significantly higher volatility, and the lack of significant steric bulk (in comparison to  $[\text{Cr}(\text{Me}^t\text{BuCOCN}^t\text{Bu})_2]$ ) may allow for enhanced surface reactivity.

## 1.7 Cyclic Voltammetry

In this thesis, cyclic voltammetry (CV) was utilized as an analytical technique to gain insight into the redox behaviour (redox potentials and electrochemical reversibility) of the synthesized complexes. In cyclic voltammetry, voltage is varied in a linear fashion (i.e. at a constant scan rate, in mV/s) and current is measured. A typical cyclic voltammogram of an analyte is presented in **Figure 1.7.1**. As an increasingly positive potential is applied, an increase in current is observed, rising to a peak at point 1 in **Figure 1.7.1**; this is termed the anodic peak potential ( $E_{pa}$ ). As the potential is linearly increased, the switching potential is eventually reached, where the scan direction is reversed; point 2 in **Figure 1.7.1**. With the decrease in the applied potential, the current begins to fall, becoming negative and reaching a downward-pointing peak; point 3 in **Figure 1.7.1**. This potential is termed the cathodic peak potential ( $E_{pc}$ ). The resulting voltammogram is commonly referred to as duck-shaped due to the resemblance.

The potential in the voltammogram at which the concentration of the oxidized and reduced species are approximately equal at the surface of the electrode is denoted as the  $E_{1/2}$  value of the analyte. This value is the average of  $E_{pa}$  and  $E_{pc}$  (the voltage at points 1 and 3 in **Figure 1.7.1**).<sup>78</sup> Provided that the analyte undergoes an electrochemically reversible process, where the activity coefficients and diffusion coefficients of the oxidized and reduced species are approximately equal, this calculation provides an estimation of the standard potential of the analyte ( $E^0$ ).<sup>78</sup>

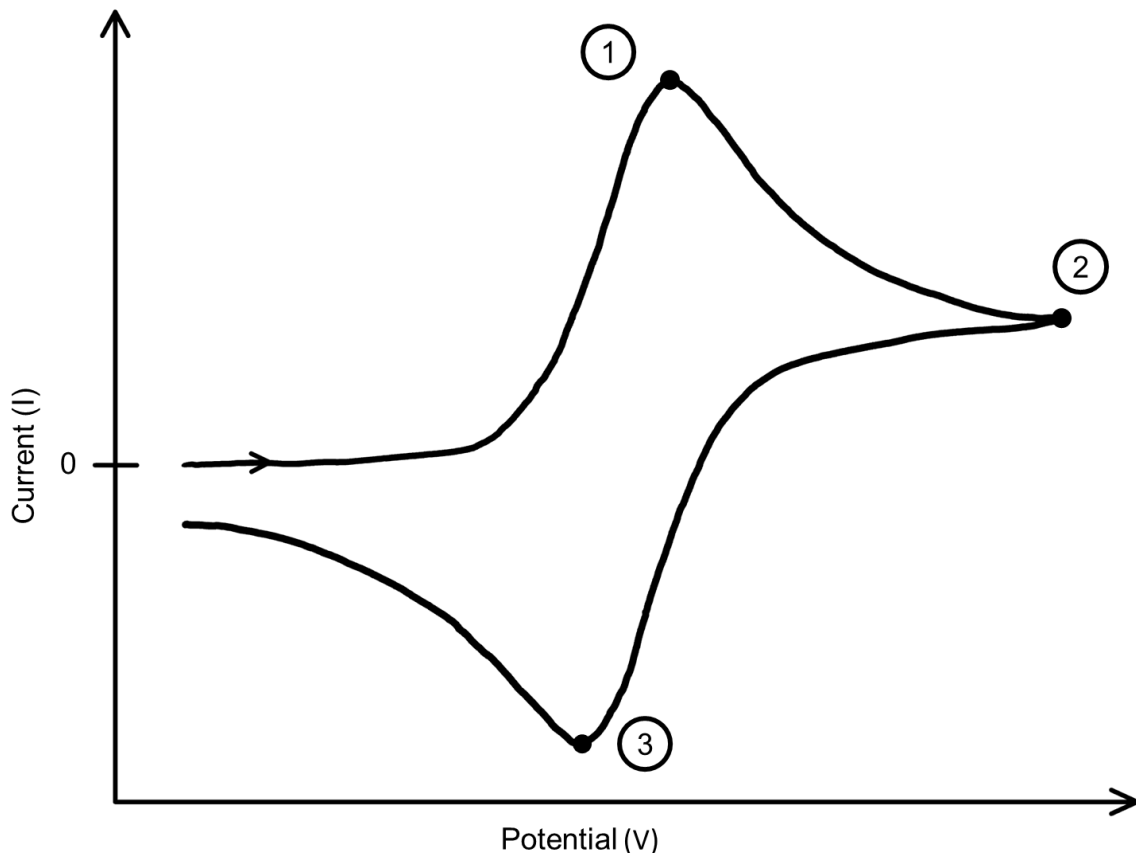


**Figure 1.7.1** Typical cyclic voltammogram of an electrochemically active analyte

The diffusion of the analyte to the electrode surface is an important aspect in cyclic voltammetry. The equilibrium between the oxidized or reduced species is described by the Nernst equation which relates the potential of an electrochemical cell to the activities of the oxidized and reduced analyte.<sup>78</sup> During a CV experiment, the concentration of analyte in solution near the electrode surface changes over time in accordance with the Nernst equation.<sup>78</sup> The electron transfer at the working electrode is expected to occur rapidly and is only limited by the diffusion of the analyte to the electrode surface.<sup>78</sup> At higher scan rates, the size of the diffusion layer decreases and higher currents are recorded.<sup>78,79</sup> For a diffusion controlled, electrochemically reversible process, the

Randles-Sevcik equation shows how the observed peak currents are influenced by various parameters (Equation 3).<sup>78,79</sup> In this equation, the magnitude of the peak current ( $i_p$ ) is directly proportional to the square root of the scan rate ( $\nu$ ).  $F$  denotes Faraday's constant,  $A$  is the surface area of the working electrode,  $C$  is the concentration of the analyte,  $n$  is the number of electrons transferred,  $D$  is the diffusion coefficient of the analyte,  $R$  is the universal gas constant, and  $T$  is the temperature of the system. If the system is operating under diffusion controlled conditions, then the ratio of the peak current and the square root of the scan rate  $\left(\frac{i_p}{\sqrt{\nu}}\right)$  would be constant.<sup>79</sup>

$$i_p = 0.4463nFAC \sqrt{\frac{nF\nu D}{RT}} \quad \text{Equation 3}$$

Under diffusion controlled systems where the analyte undergoes oxidation and reduction reversibly (electrochemical reversibility), the anodic current ( $i_{pa}$ ) and cathodic current ( $i_{pc}$ ) are equal in magnitude.<sup>79</sup> Depending on the system employed and the direction that the potential is applied, either reduction or oxidation will be the first observed redox process in the cyclic voltammogram. Thus, the peak currents are henceforth denoted as  $i_{pf}$  and  $i_{pr}$  for the forward peak current and the reverse peak current, respectively. Provided that the system is operating under Nernstian conditions, two important parameters can be obtained from the cyclic voltammogram: (1) the ratio of peak currents  $\left(\frac{i_{pr}}{i_{pf}}\right)$  and (2) the peak-to-peak separation of the anodic and cathodic peak potentials ( $\Delta E = E_{pa} - E_{pc}$ ).<sup>79</sup> For an electrochemically reversible process,  $\frac{i_{pr}}{i_{pf}}$  is equal

to 1, regardless of the scan rate.<sup>79,80</sup> However,  $E_{pr}$  must be measured relative to the baseline shown (approximately) in red on **Figure 1.7.2**, and this baseline cannot be accurately determined so close to the switching potential. Therefore, to determine the electrochemical reversibility of a system, Nicholson proposed that the ratio of  $\frac{i_{pr}}{i_{pf}}$  can be calculated using Equation 4.<sup>79,80</sup>

$$\frac{i_{pr}}{i_{pf}} = \frac{(i_{pr})_0}{i_{pf}} + 0.485 \frac{i_{\lambda}}{i_{pf}} + 0.086 \quad \text{Equation 4}$$

In this equation,  $i_{pf}$ ,  $i_{\lambda}$ , and  $(i_{pr})_0$  are measured with respect to the zero current baseline shown in green in **Figure 1.7.2**, which can be accurately determined.

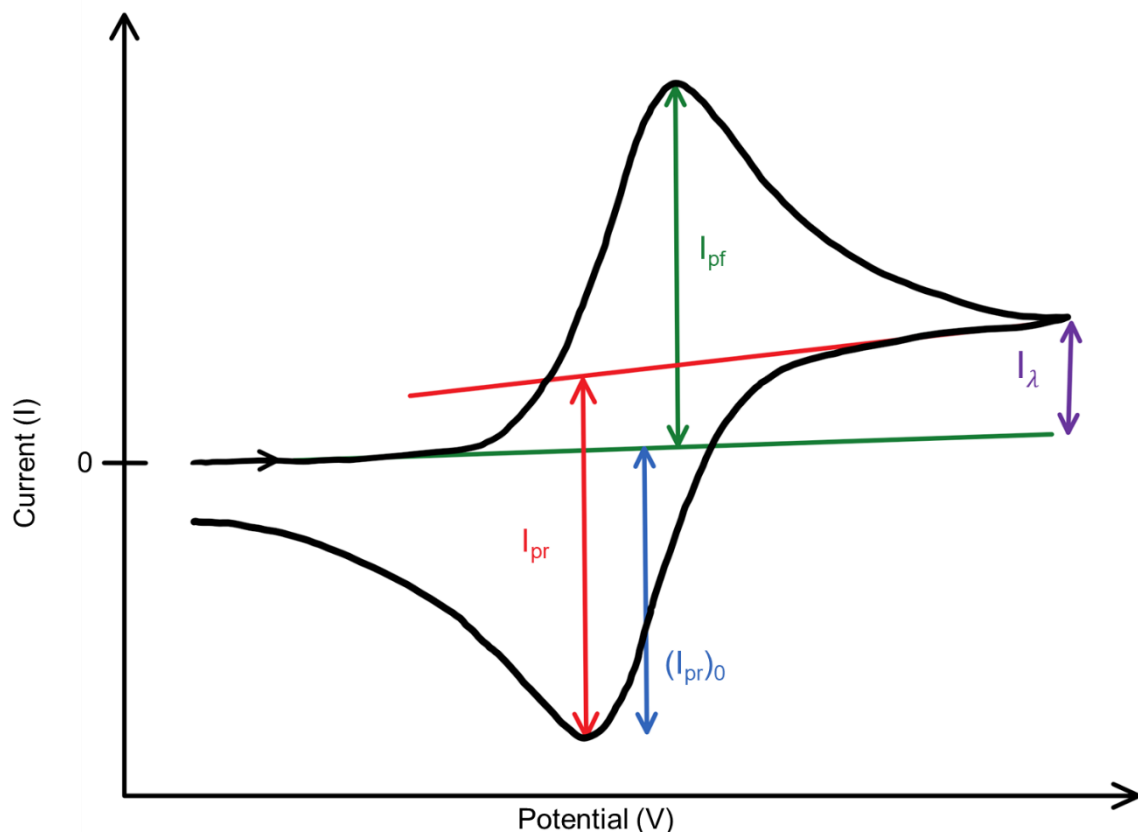


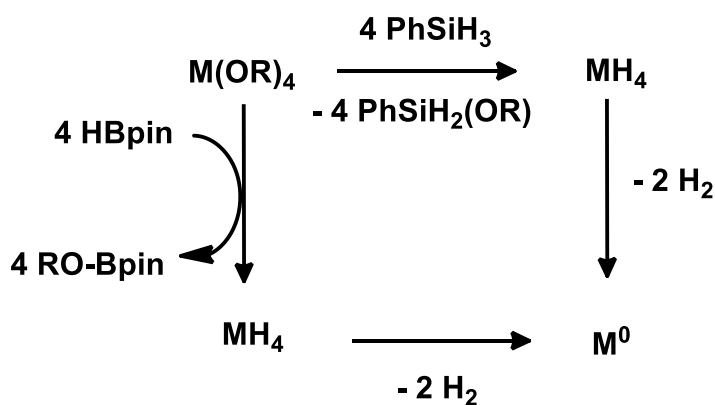
**Figure 1.7.2** Application of the Nicholson equation check to a typical cyclic voltammogram

Another qualitative analysis of the electrochemical reversibility of the analyte is the peak-to-peak separation ( $\Delta E_p = E_{pa} - E_{pc}$ ). Upon addition of a calibrant such as ferrocene to the CV, the peak-to-peak separation of the analyte can be compared with that for the calibrant, provided that the peak currents are roughly equal for the analyte and calibrant. A large analyte peak-to-peak separation (compared to that for the calibrant) is indicative of electrochemical irreversibility.<sup>78,79</sup> However, this is not a very accurate determination of the electrochemical reversibility as there are several factors which affect the peak-to-peak separation.<sup>79</sup>

## 2 Homoleptic *Tert*-butoxide Complexes of Vanadium and Chromium

### 2.1 Precursor Molecules, Co-reagents, and Proposed Reactivity

In order to develop a viable method for metal ALD, it is necessary to choose a precursor and a co-reagent that exhibit high reactivity toward one another, resulting in the production of elemental metal and volatile by-products. Motivated by the thermodynamically favourable formation of Si–O and B–O bonds, it was hypothesized that reactions of metal alkoxides with hydrosilanes or hydroboranes could result in the reduction of the metal to its elemental state, producing only highly volatile silane/borane by-products. The proposed reaction pathway for metal deposition using alkoxides in combination with a hydrosilane (PhSiH<sub>3</sub>) or a hydroborane (HBpin) as the co-reagent is presented in **Scheme 2.1.1**.



**Scheme 2.1.1** Hypothesized reaction pathways for the deposition of elemental metal through the reaction of a metal alkoxide with a hydrosilane (PhSiH<sub>3</sub>) and or a hydroborane (HBpin).

It was hypothesized that the metal alkoxides would react with these co-reagents via a sigma bond metathesis to afford a metal polyhydride. This metal hydride species could then undergo the reductive elimination of hydrogen gas to afford the elemental metal; the thermal stabilities of chromium and vanadium hydrides are discussed in Sections 1.4 and 1.5. It is also important to note that metal hydride species formed on the surface during ALD may be expected to have reduced thermal stability relative to a bulk hydride material. The alkoxy silane and alkoxy borane by-products are expected to be volatile, enabling efficient removal from the surface of the growing film during ALD. Metal alkoxides have often been used for the deposition of metal oxide thin films by ALD using water or oxygen as co-reagents.<sup>81-83</sup> However, by employing hydrosilane or hydroborane co-reagents, reduction to elemental metal is anticipated to be possible.

Two additional silicon-containing compounds were synthesized as potential co-reagents according to literature procedures: decamethylsilicocene (**3**) and 1,4-bis(trimethylsilyl)-2-methyl-2,5-cyclohexadiene (**4**), presented in **Figure 2.1.1**.

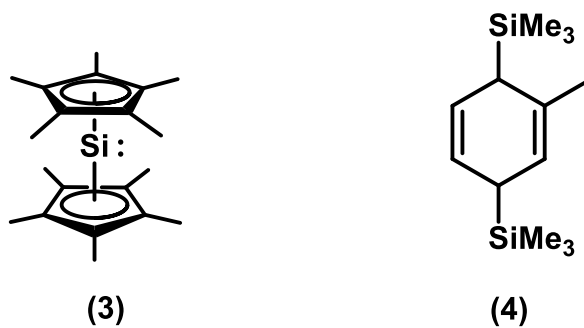
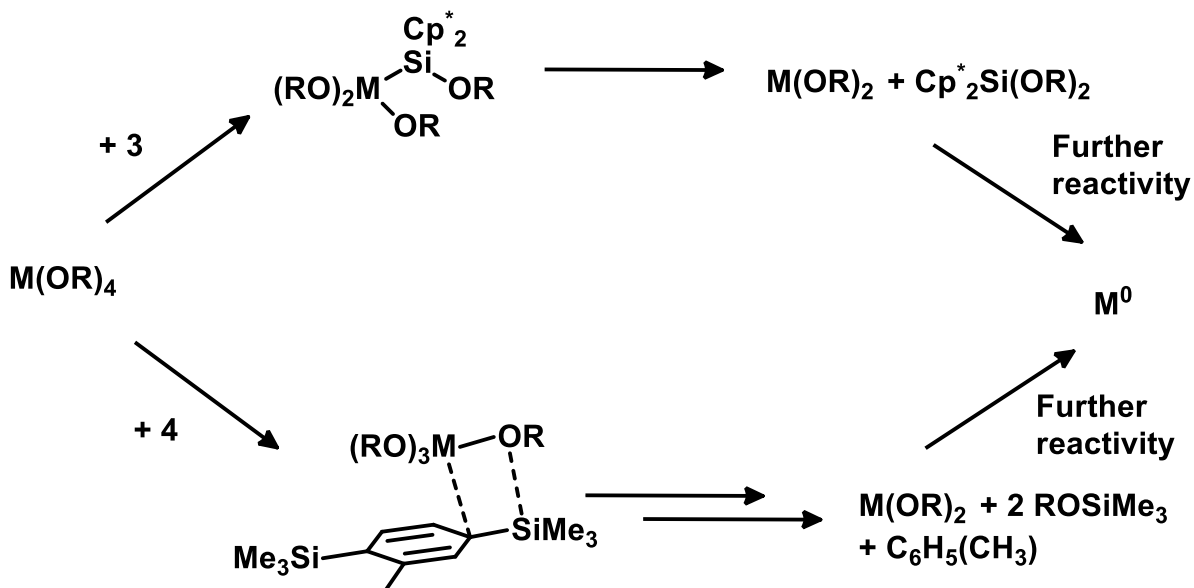


**Figure 2.1.1** Structures of the potential co-reagents decamethylsilicocene (**3**), and 1,4-bis(trimethylsilyl)-2-methyl-2,5-cyclohexadiene (**4**).

The proposed reaction pathway of compounds **3** and **4** with metal alkoxides is shown in **Scheme 2.1.2**.<sup>84–86</sup> Compound **3** is denoted as  $\text{SiCp}^*_2$  in this scheme.



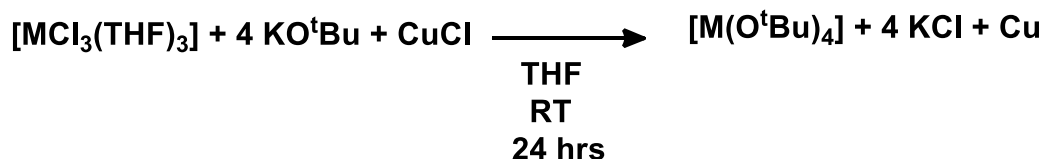
**Scheme 2.1.2** Hypothesized reaction pathways for the deposition of elemental metal through the reaction of a metal alkoxide with silicon-containing compounds **3** and **4**.

In this chapter, the syntheses of potential ALD precursors  $[\text{Cr}(\text{O}^t\text{Bu})_4]$  (**1**) and  $[\text{V}(\text{O}^t\text{Bu})_4]$  (**2**) is described, along with investigation of the thermal stability and volatility of these complexes. In addition, the solution reactivity of these complexes with potential ALD co-reagents is described, to assess whether a particular precursor/co-reagent combination shows promise for metal ALD.

## 2.2 Synthesis and Characterization of $[\text{Cr}(\text{O}^t\text{Bu})_4]$ (**1**) and $[\text{V}(\text{O}^t\text{Bu})_4]$ (**2**)

The syntheses of  $[\text{Cr}(\text{O}^t\text{Bu})_4]$  (**1**) and  $[\text{V}(\text{O}^t\text{Bu})_4]$  (**2**) were previously reported in literature via the reaction of the trivalent metal halide with four equivalents of  $\text{KO}^t\text{Bu}$  in

the presence of copper(I) chloride as an oxidizing agent. The reaction is indicated in **Scheme 2.2.1**. These syntheses were replicated with some modifications (room temperature reactivity and purification by sublimation/distillation without prior filtration).



**Scheme 2.2.1** Synthesis of  $[\text{M}(\text{O}^t\text{Bu})_4]$ ,  $\text{M} = \text{Cr}$  (**1**) or  $\text{M} = \text{V}$  (**2**).

Complex **1** was isolated in 66% yield and complex **2** was isolated in 47% yield. These complexes are volatile at room temperature which complicated their isolation, due to loss of the product during solvent removal under vacuum. Complex **1** is a deep blue solid and complex **2** is a bright blue solid or liquid depending on the ambient temperature. The  $^1\text{H}$  NMR spectra of these complexes show just a single paramagnetically broadened and shifted peak at 3.02 ppm for **1** and 3.07 ppm for **2** in  $\text{C}_6\text{D}_6$ . These complexes display extensive solubility in all organic solvents tested (THF, diethyl ether, toluene, benzene, hexanes, and pentane).

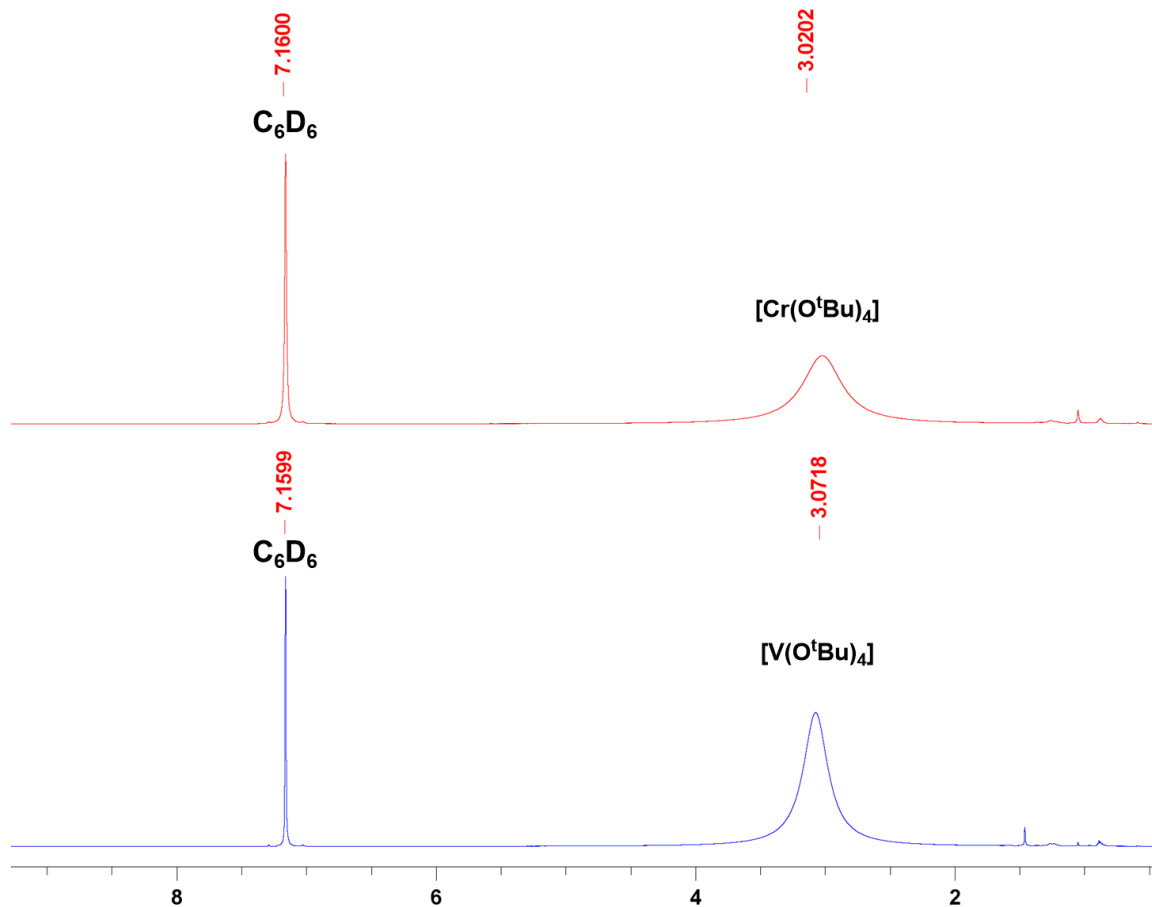


**Figure 2.2.1**  $^1\text{H}$  NMR spectra ( $\text{C}_6\text{D}_6$ , 600 MHz) of  $[\text{Cr}(\text{O}^t\text{Bu})_4]$  (**1**) (top) and  $[\text{V}(\text{O}^t\text{Bu})_4]$  (**2**) (bottom).

### 2.3 Thermal Stability and Volatility of $[\text{Cr}(\text{O}^t\text{Bu})_4]$ (**1**)

The thermal stability of  $[\text{Cr}(\text{O}^t\text{Bu})_4]$  (**1**) was evaluated by heating a neat sample in a J-Young tube until decomposition was observed, evident through the discolouration of the sample. Complex **1** exhibited slight decomposition when heated for 24 hours at 110 °C; prolonged heating (for 3 days) allowed the sample to fully decompose. The decomposition products were identified as *tert*-butanol and isobutylene by  $^1\text{H}$  NMR spectroscopy (**Figure 2.3.1**).

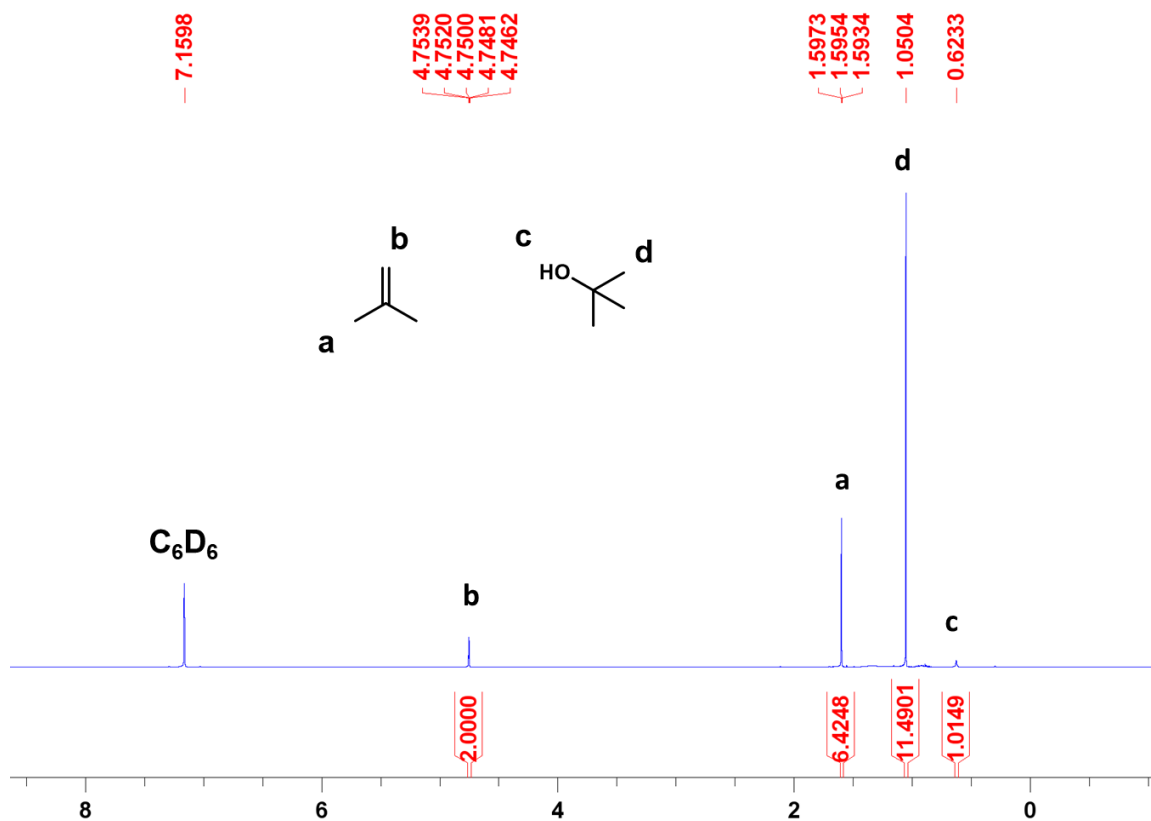
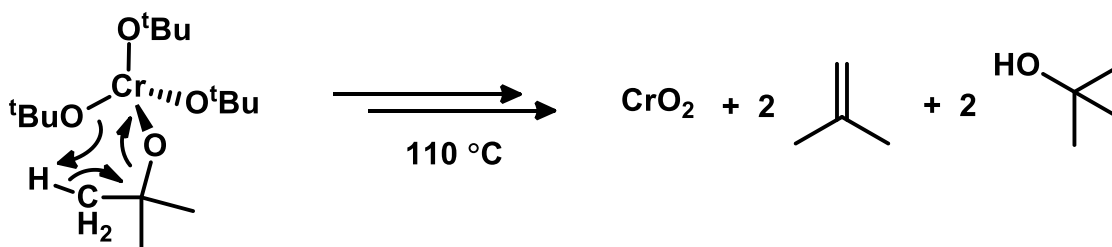


**Figure 2.3.1**  $^1\text{H}$  NMR spectrum ( $\text{C}_6\text{D}_6$ , 600 MHz) of the decomposition products after heating neat  $[\text{Cr}(\text{O}^t\text{Bu})_4]$  (**1**) at  $110\text{ }^\circ\text{C}$  for 3 days.

The identification of these decomposition products suggests decomposition to  $\text{CrO}_2$  via the mechanism proposed in **Scheme 2.3.1**.



**Scheme 2.3.1** Proposed decomposition mechanism for  $[\text{Cr}(\text{O}^t\text{Bu})_4]$  (**1**).

In order to analyze the insoluble decomposition product(s) by PXRD, a sample of **1** was heated in a thick-walled Schlenk flask at 140 °C for one week. A long reaction time and high temperature was required due to the sample subliming to the Teflon tap sealing the flask. Prolonged heating was necessary to ensure the sample was entirely decomposed. A green film with black spots was observed on the walls of the flask. In order to isolate the decomposition material, hexanes was introduced to the flask, which was then subjected to sonication for an extended period of time. The suspension was centrifuged and washed with hexanes three times. The powder was then dried *in vacuo* overnight and was packed in a capillary for analysis by PXRD. The powder was found to be amorphous by PXRD. However, due to the green colour of the film, it is suspected to contain Cr<sub>2</sub>O<sub>3</sub> which is a green powder, often used as a pigment. However, the mechanism by which reduction to Cr(III) takes place is not clear. The black powder might be CrO<sub>2</sub> as previously predicted in **Scheme 2.3.1**. While packing the powder into the capillary for analysis by PXRD, the powder was found to stick to the metal spatula providing supporting evidence for the presence of CrO<sub>2</sub> due to the ferromagnetic nature of this compound.

Thermal decomposition studies are important for understanding the pathways by which decomposition can occur, such that it could be avoided when designing a new precursor for ALD. Additionally, if the presence of oxygen is detected in the deposited thin films, then it would be an indication that decomposition of the precursor is occurring on the substrate leading to CVD rather than ALD.

Complex **1** undergoes sublimation at 25 °C at 10 mTorr. As a crude approximation, the temperature required to deliver a precursor to the substrate in an ALD

reactor is 40 °C above the sublimation temperature on the vacuum line (the pressure in an ALD reactor is higher than that of the vacuum line: 250 mTorr as opposed to 10 mTorr). Thus, the useful range of bubbler temperatures for **1** is between 65-100 °C.

The volatility and thermal stability of complex **1** was also evaluated using inert atmosphere thermogravimetric analysis (TGA). In this technique, which provides information on a short timescale, and at atmospheric pressure (760 Torr), the complex is weighed on a platinum pan and is heated under a stream of inert gas at a ramp rate of 10 °C/min. The mass loss due to volatilization or thermal decomposition is recorded as a function of increasing temperature. The most promising ALD precursors would exhibit volatility at low temperatures, such that extensive heating is not required to deliver the precursor to the substrate. Additionally, the precursor should not decompose prior to, or during, volatilization, although it is important to remember that the pressure in an ALD reactor will be much lower than 760 Torr, so decomposition during TGA does not necessarily mean that a precursor cannot be delivered on an ALD reactor without decomposition. Clean precursor volatilization results in a single mass loss event. By contrast, decomposition typically results in multiple mass loss events, potentially accompanied by mass loss due to precursor volatilization. When volatilization occurs without decomposition, a residual mass of zero can be expected; in practice, a residual mass percentage <5% is often considered to be indicative of clean volatilization. The TGA for **1** is displayed in **Figure 2.3.2**.

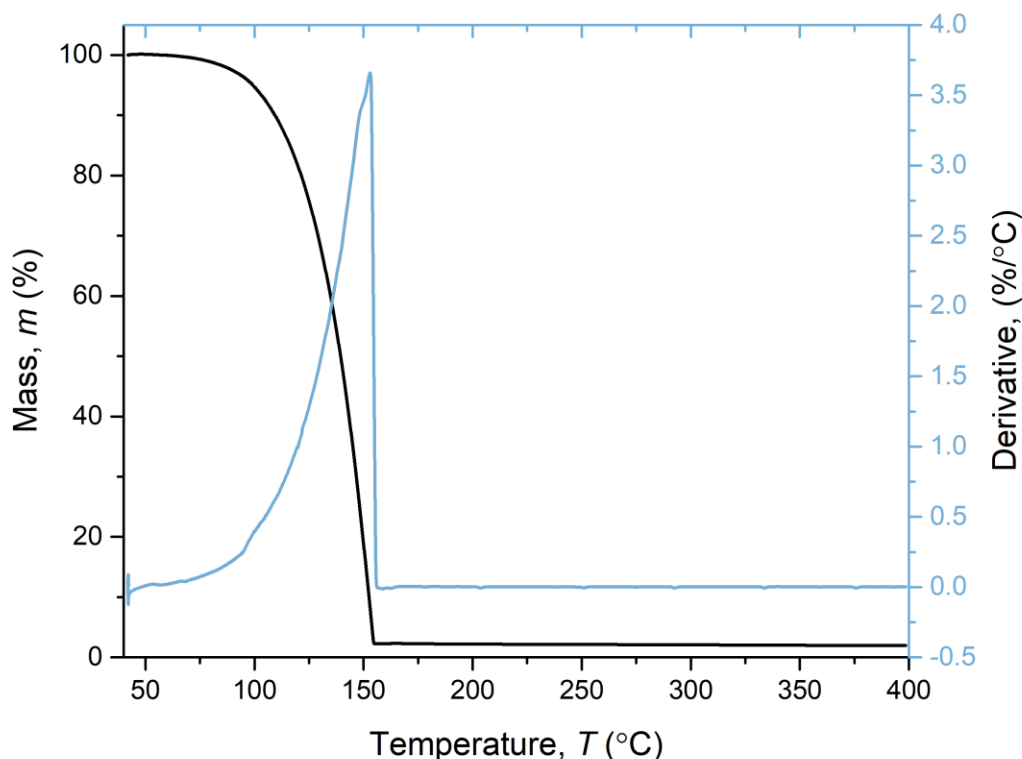


**Figure 2.3.2** TGA data for complex **1**, and the derivative curve expressed as the rate of change of the percentage mass with respect to temperature.

The residual mass percentage ( $\%m_{res}$ ) of **1** is 1.95%, indicating that most of the precursor volatilizes without decomposition. The rate of volatilization is also presented as the derivative of the percentage mass loss with respect to the temperature. A perfectly uniform volatilization event would result in an exponential increase in mass loss until the entirety of the sample is lost – at which point the rate of mass loss drops rapidly to zero in the derivative curve. As can be observed in the TGA experiment, the derivative curve indicates complete volatilization of the precursor candidate.

## 2.4 Thermal Stability and Volatility of [V(O<sup>t</sup>Bu)<sub>4</sub>] (**2**)

A neat sample of **2** was heated in the presence of light in a J-Young tube at 75 °C for 3 days until a dark brown residue was observed on the walls of the tube. C<sub>6</sub>D<sub>6</sub> was then added in the glovebox and a <sup>1</sup>H NMR spectrum of soluble decomposition products was acquired; **Figure 2.4.1**.

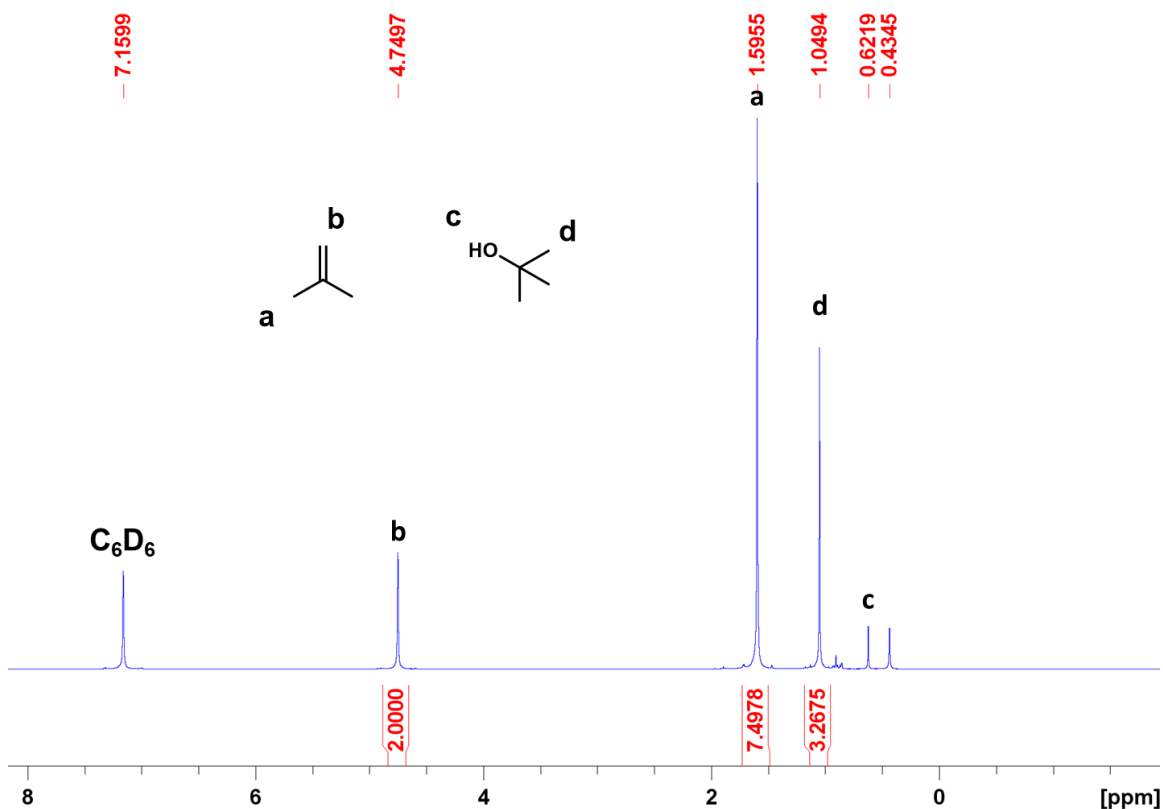


**Figure 2.4.1** <sup>1</sup>H NMR spectrum (C<sub>6</sub>D<sub>6</sub>, 600 MHz) of the decomposition products of neat [V(O<sup>t</sup>Bu)<sub>4</sub>] (**2**) after heating at 75 °C overnight.

This spectrum shows the generation of isobutylene and *tert*-butanol, as observed in the thermal decomposition of **1**. However, the amount of *tert*-butanol is much less than expected relative to isobutylene. Given this unexpected result, the analysis was repeated, and the evolution of isobutylene was indicated by <sup>1</sup>H NMR spectroscopy (**Figure 2.4.2**).

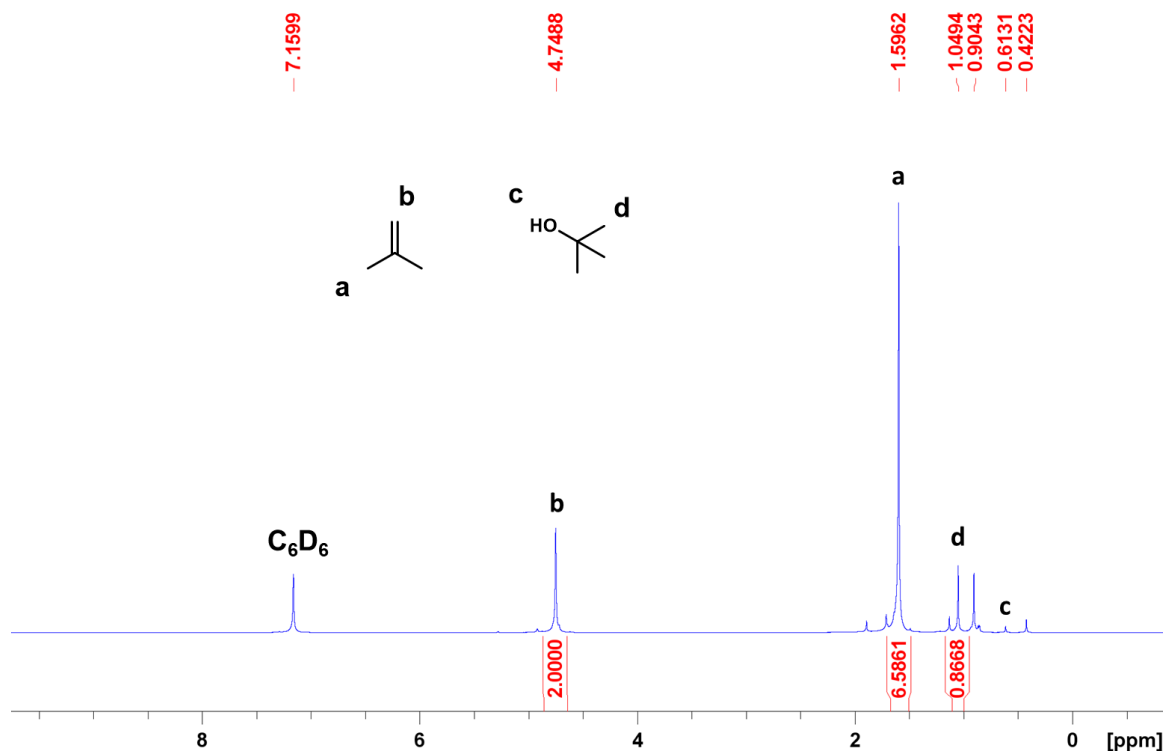
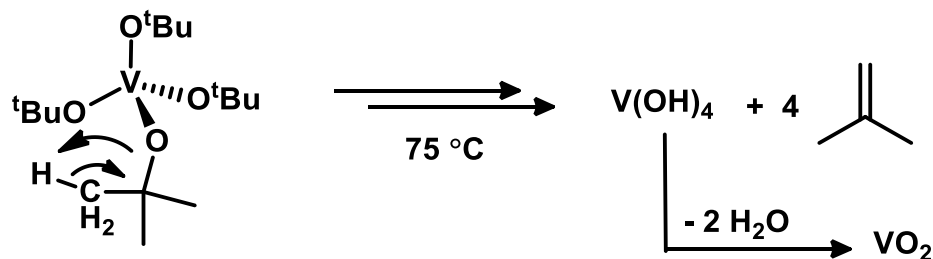


**Figure 2.4.2** <sup>1</sup>H NMR spectrum (C<sub>6</sub>D<sub>6</sub>, 600 MHz) of the repeated analysis of the decomposition products of [V(O<sup>t</sup>Bu)<sub>4</sub>] (**2**) after heating at 75 °C overnight.

However, the ratio between *tert*-butanol and isobutylene was even lower than in the first attempt. This result suggests a competing decomposition pathway which affords isobutylene but not *tert*-butanol; perhaps that shown in **Scheme 2.4.1**, although, H<sub>2</sub>O was not conclusively identified as a reaction by-product in the <sup>1</sup>H NMR spectrum. Additionally, previous literature proposes that the decomposition pathway of **2** proceeds as proposed in **Scheme 2.3.1** for the chromium analogue; so the ratio of the *tert*-butanol and isobutylene by-products in this work is surprising.<sup>87</sup>



**Scheme 2.4.1** Possible decomposition mechanism for  $[\text{V}(\text{O}^t\text{Bu})_4]$  (**2**)

The decomposition of **2** was repeated, and the dark brown powder was isolated. The powder was washed with toluene and hexanes three times each. The powder was then dried *in vacuo* overnight and was packed in a capillary tube for analysis by PXRD. The powder was determined to be amorphous by PXRD.

Suspecting that the presence of light may catalyze the decomposition of **2** at lower temperatures, the decomposition of **2** was repeated in the absence of light. A neat sample of **2** was heated in a J-Young tube up to 100 °C for 24 hours without any visible decomposition. Decomposition was observed when the sample was heated to 110 °C for 24 hours. As a test of the long term thermal stability of **2**, a neat sample was heated to 100 °C for 72 hours without any observed decomposition. However, after one week, the sample was completely decomposed. The decomposition products in this analysis could not be identified by NMR spectroscopy as the nature of the sample prohibited shimming of the NMR spectrometer. The sudden onset of decomposition may be indicative of an autocatalytic mechanism. It is possible that **2** would exhibit thermal stability at 90 °C in the absence of light for longer periods of time, although, this analysis was not conducted.

Complex **2** is highly volatile and can be isolated by distillation at 25 °C (10 mTorr). Applying the approximation that the minimum temperature for an ALD

process is 40 °C above the distillation temperature, the temperature for delivery of **2** is 65 °C. Provided that decomposition of **2** is observed at 100 °C in the absence of light when the sample is heated for extended periods of time, the range of bubbler temperatures for the delivery of **2** is 65-90 °C. A sample of complex **2** was analyzed by TGA and was found to exhibit complete volatilization with minimal decomposition. The TGA data for **2** is presented **Figure 2.4.3**. The % $m_{res}$  of **2** is 2.35% and the derivative curve indicates uniform volatilization.

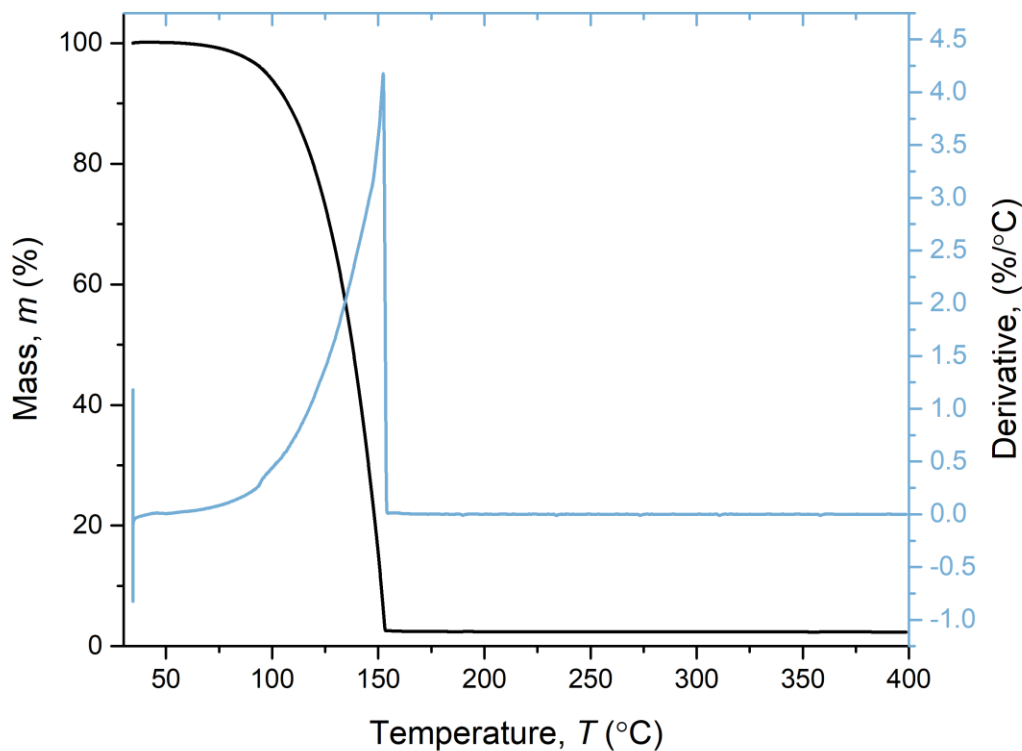


**Figure 2.4.3** TGA data for complex **2**, and the derivative curve expressed as the rate of change of the percentage mass with respect to temperature.

The TGA of **2** has previously been reported in literature with a  $\%m_{res}$  of 33%,<sup>87</sup> and the authors attributed the observed mass loss event to be due to the decomposition of  $[V(O^tBu)_4]$  to  $VO_2$  with residual carbon content. It is suspected that this analysis was not conducted under sufficiently inert conditions.

## 2.5 Reactivity Studies with HBpin

Reactivity studies were conducted between complex **1** and 5 equivalents of HBpin, in  $C_6D_6$  in a J-Young tube. The evolution of a gas (presumably hydrogen gas) was noted roughly 1 hour after addition. The solution was left to react overnight at room temperature, which afforded a very thick black suspension. In order to record NMR spectra of the reaction products, the suspension was centrifuged, and the colourless supernatant was decanted. The  $^1H$  NMR spectrum of the decanted supernatant is presented in **Figure 2.5.1**.



In an attempt to identify the powder that was collected, the reaction was repeated on a larger scale. The resulting black suspension was then centrifuged, the mother liquors were decanted, and the solid was washed with toluene three times. To remove the possibility of any grease contamination, the black powder was then washed with hexanes three times. The powder was then dried *in vacuo* overnight. A pestle and mortar were used to produce a fine powder prior to packing in a capillary for analysis by PXRD. However, the powder was found to be amorphous. Suspecting that chromium might be acting as a beam stop for the incoming X-rays, the analysis was repeated using graphite as a diluent. However, the only signals that were observed were those due to graphite.

In case the black powder might be a chromium hydride species (i.e.  $\text{CrH}_2$ ), a portion of the powder was heated in  $\text{C}_6\text{D}_6$  in a J-Young tube at 100 °C overnight, given that chromium hydrides are reported to decompose below this temperature; see Sections 1.4 and 1.5. The evolution of hydrogen gas was not observed by NMR spectroscopy. A sample of the black powder was also heated to 200 °C overnight while exposed to dynamic vacuum (10 mTorr). However, PXRD analysis of this powder still showed that the solid was amorphous.

Similarly, solution reactivity analysis was performed between HBpin and **2**, in order to determine whether this combination of precursor candidate and co-reagent may be suitable for an ALD process. In a J-Young tube, **2** was combined with 5 equivalents of HBpin in  $\text{C}_6\text{D}_6$ . Upon the addition of HBpin, the solution changed colour from bright blue to teal green within a few seconds. The evolution of gas bubbles was observed, and within an hour at room temperature, the mixture became dark black, as depicted in **Figure 2.5.2**.

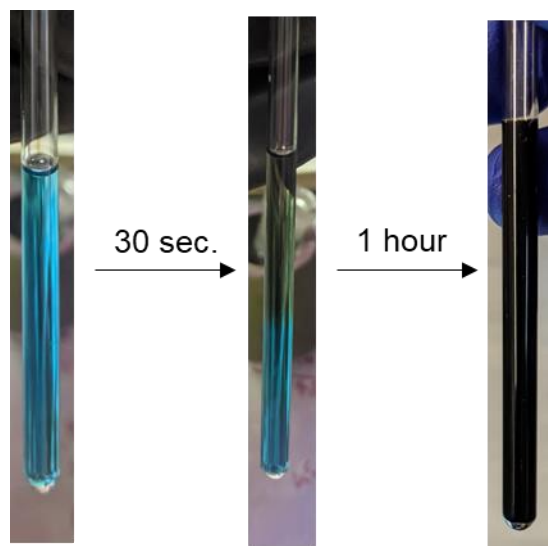


**Figure 2.5.2** Colour changes associated with the reaction of complex **2** with HBpin in  $C_6D_6$ .

A  $^1H$  NMR spectrum of the reaction solution was acquired after one hour and the presence of hydrogen gas was identified, as indicated in the spectrum below. Excess HBpin is still present in the  $^1H$  NMR spectrum, which is expected given that one extra equivalent was utilized in the reaction. The  $^tBuO$ -Bpin species that was previously identified in **Figure 2.5.1** was also observed in this spectrum.

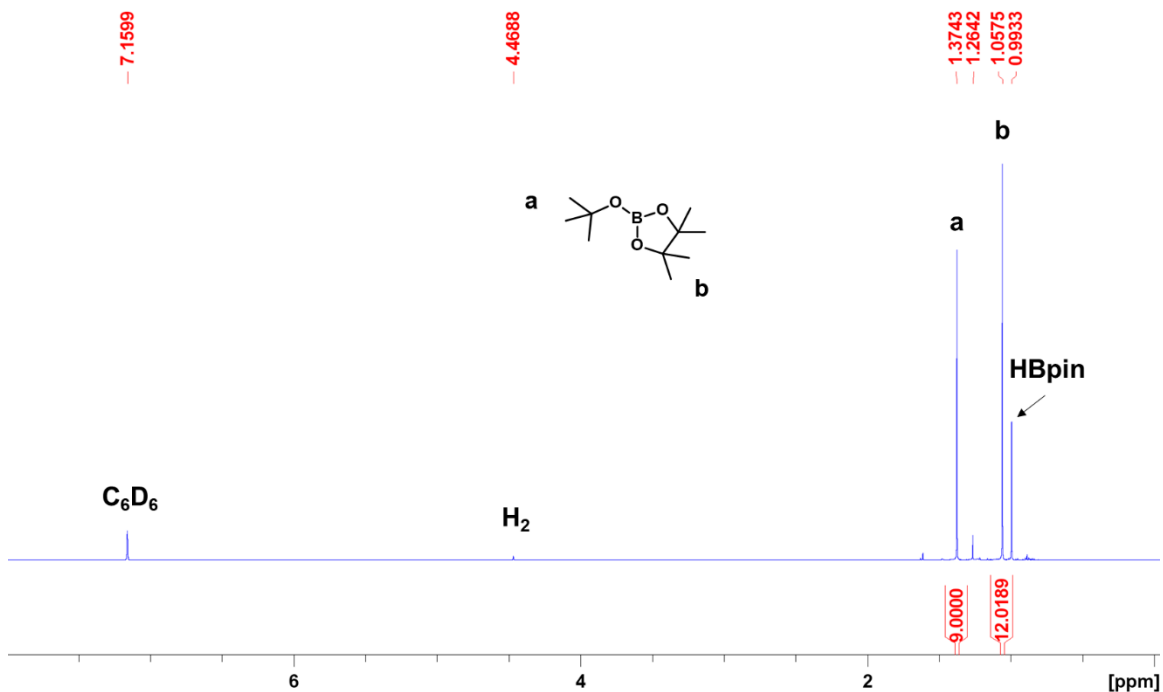


**Figure 2.5.3** <sup>1</sup>H NMR spectrum (C<sub>6</sub>D<sub>6</sub>, 600 MHz) of the reaction between [V(O<sup>t</sup>Bu)<sub>4</sub>] (**2**) and HBpin in a J-Young tube after 1 hour at room temperature.

These observations suggest that the reaction of [V(O<sup>t</sup>Bu)<sub>4</sub>] (**2**) with HBpin proceeds analogously to the reaction of [Cr(O<sup>t</sup>Bu)<sub>4</sub>] (**1**) with this co-reagent, as proposed in **Scheme 2.5.1**. The black colour of the solution could indicate the precipitation of an insoluble vanadium species, potentially vanadium metal. However, attempts to separate the powder by centrifugation were unsuccessful. Consequently, this reaction was repeated on a larger scale, and the volatile by-products were removed by distillation. The residual black powder was washed with hexanes three times and dried *in vacuo* overnight. The powder was then packed in a capillary and was determined to be amorphous by PXRD.

Investigating the possibility that the black precipitate is a vanadium hydride species, a portion of the sample in C<sub>6</sub>D<sub>6</sub> was heated in a J-Young tube overnight at

100 °C, given that vanadium hydrides are reported to thermally decompose to vanadium metal below this temperature; see Section 1.4. The evolution of hydrogen gas was not observed by NMR spectroscopy. A sample of the black powder was also heated to 200 °C overnight while exposed to dynamic vacuum (10 mTorr), but PXRD analysis of this powder determined it to be amorphous.

## 2.6 Reactivity Studies with PhSiH<sub>3</sub>

Given the promising reactivity that was observed with HBpin, solution reactivity tests were also conducted between complexes **1** and **2** with PhSiH<sub>3</sub> in a J-Young tube in C<sub>6</sub>D<sub>6</sub>. For compound **1**, no reactivity was observed at room temperature when left overnight. The reaction was heated to 60 °C overnight and the solution adopted a black colour. However, <sup>1</sup>H NMR spectrum indicated the presence of only starting material. The reaction solution was then heated to 60 °C for an additional two days until the broad singlet at 3 ppm (due to complex **1**) was fully consumed. The products of the reaction after three days at 60 °C are indicated in the <sup>1</sup>H NMR spectrum in **Figure 2.6.1**.

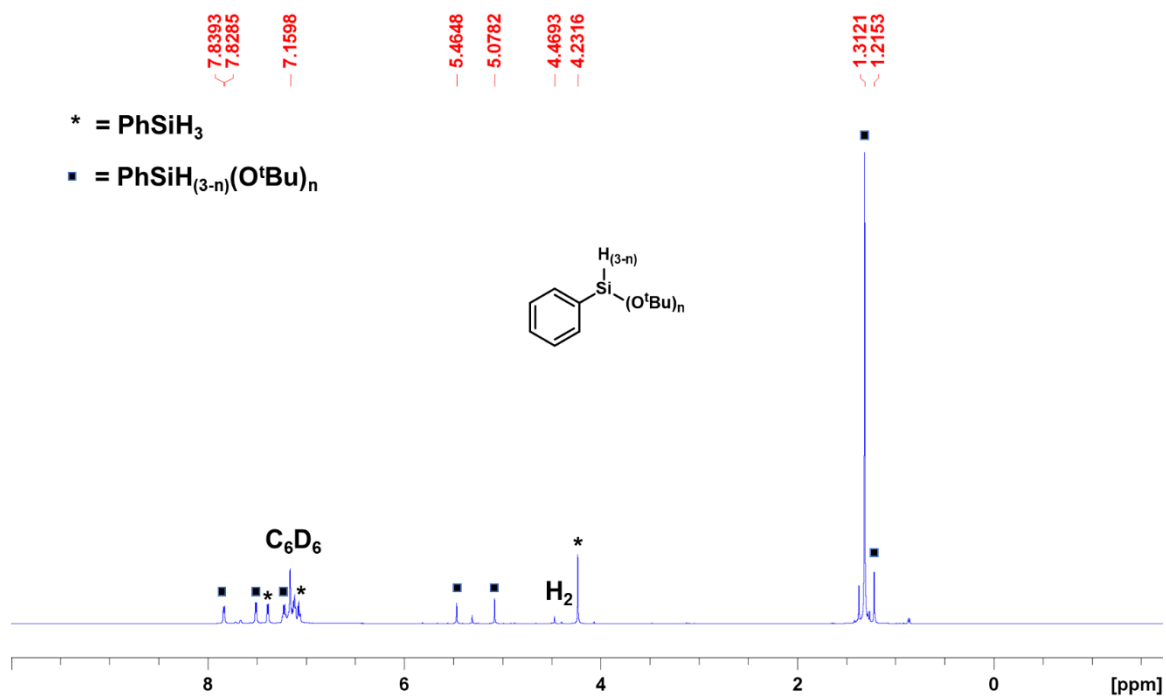


**Figure 2.6.1** <sup>1</sup>H NMR spectrum (C<sub>6</sub>D<sub>6</sub>, 600 MHz) of the reaction between [Cr(O<sup>t</sup>Bu)<sub>4</sub>] (**1**) and PhSiH<sub>3</sub> in a J-Young tube after 3 days at 60 °C.

In order to isolate the precipitate that was generated from the reaction mixture, the reaction was repeated on a larger scale, and the volatile by-products were removed by vacuum distillation (10 mTorr) using moderate heating. The remaining brown powder was then dried *in vacuo* overnight. The PXRD pattern obtained for this sample is presented in **Figure 2.6.2**.

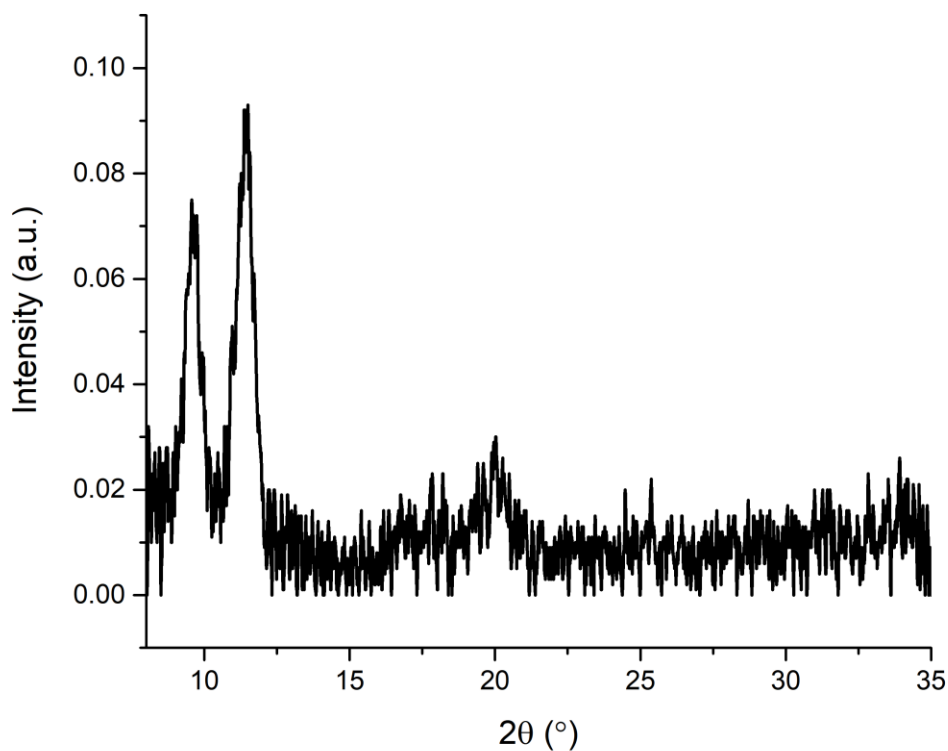


**Figure 2.6.2** PXRD diffractogram of the brown powder isolated from the reaction of  $[\text{Cr}(\text{O}^t\text{Bu})_4]$  (**1**) and  $\text{PhSiH}_3$ .

The observed peaks at  $2\theta$  values of  $9.6^\circ$  and  $11.5^\circ$  are not suspected to be diffraction peaks due to the sample. The low intensity of these peaks and the low angle values at which they are present suggest they may be due to air-scattering or possible organic contaminants in the sample as there was no match with any known chromium metal or chromium hydride species. The sample was deemed to be amorphous by PXRD.

The reactivity of  $[\text{V}(\text{O}^t\text{Bu})_4]$  (**2**) with 5 equivalents of  $\text{PhSiH}_3$  in a J-Young tube in  $\text{C}_6\text{D}_6$  was also investigated. No reactivity was observed when the solution was left at

room temperature. However, reactivity was observed when the sample was heated to 70 °C overnight. The reaction was monitored over time, and it was found that the starting material, **2**, was still present by NMR spectroscopy after two days of heating. The reaction solution was monitored over the course of five days at 70 °C until the starting material (**2**) was fully consumed, affording an opaque black mixture. The progression of the reaction is displayed in **Figure 2.6.3** over the course of five days, indicating the formation of hydrogen gas as well as new hydrosilanes, presumably  $\text{PhSiH}_{(3-n)}(\text{O}^t\text{Bu})_n$

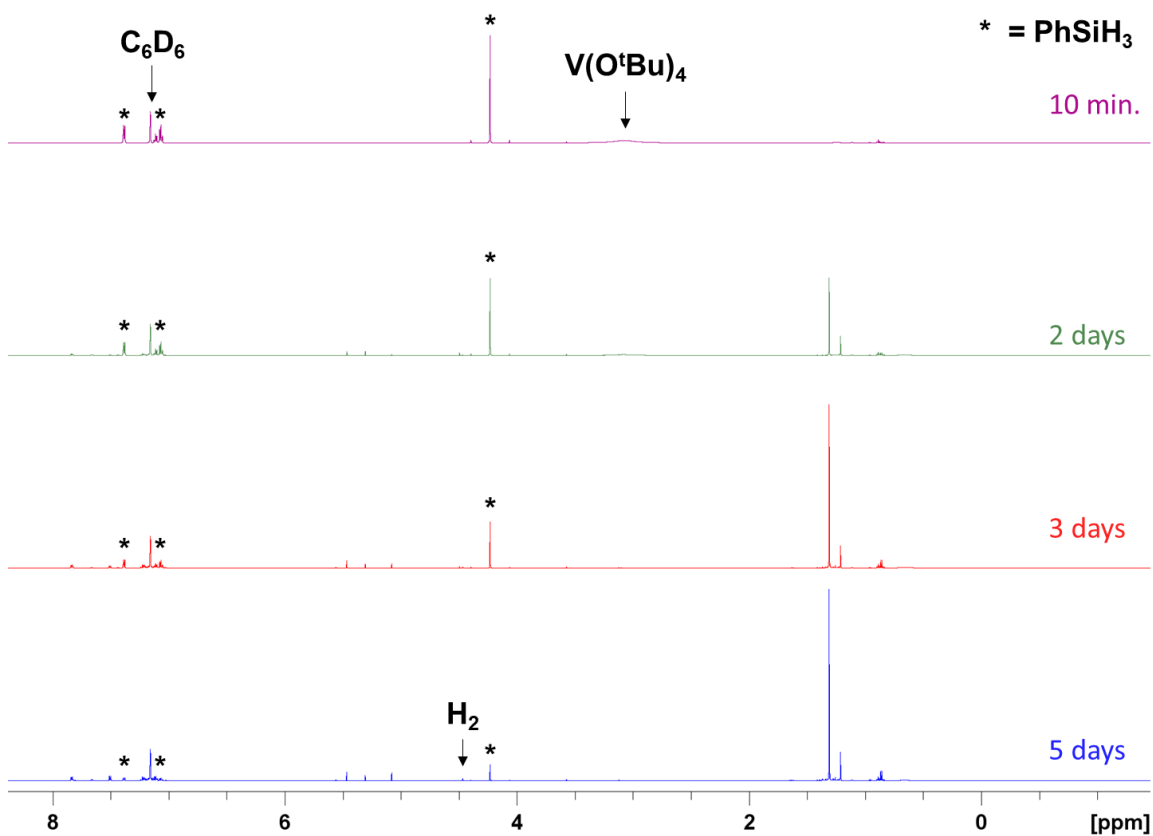


**Figure 2.6.3**  $^1\text{H}$  NMR spectra ( $\text{C}_6\text{D}_6$ , 600 MHz) of the reaction between  $[\text{V}(\text{O}^t\text{Bu})_4]$  (**2**) and  $\text{PhSiH}_3$  in a J-Young tube over the course of 5 days at 70 °C.

To identify the major reaction by-product, a 2D NOESY NMR experiment (**Figure 2.6.4**) was recorded. Specifically, the objective was to identify which ortho phenyl CH peaks (located between 7.3 and 7.9 ppm), SiH peaks, and O<sup>t</sup>Bu peaks belong to the same molecule, so that relative integrations of these peaks can be used to determine the identity of the major by-products.

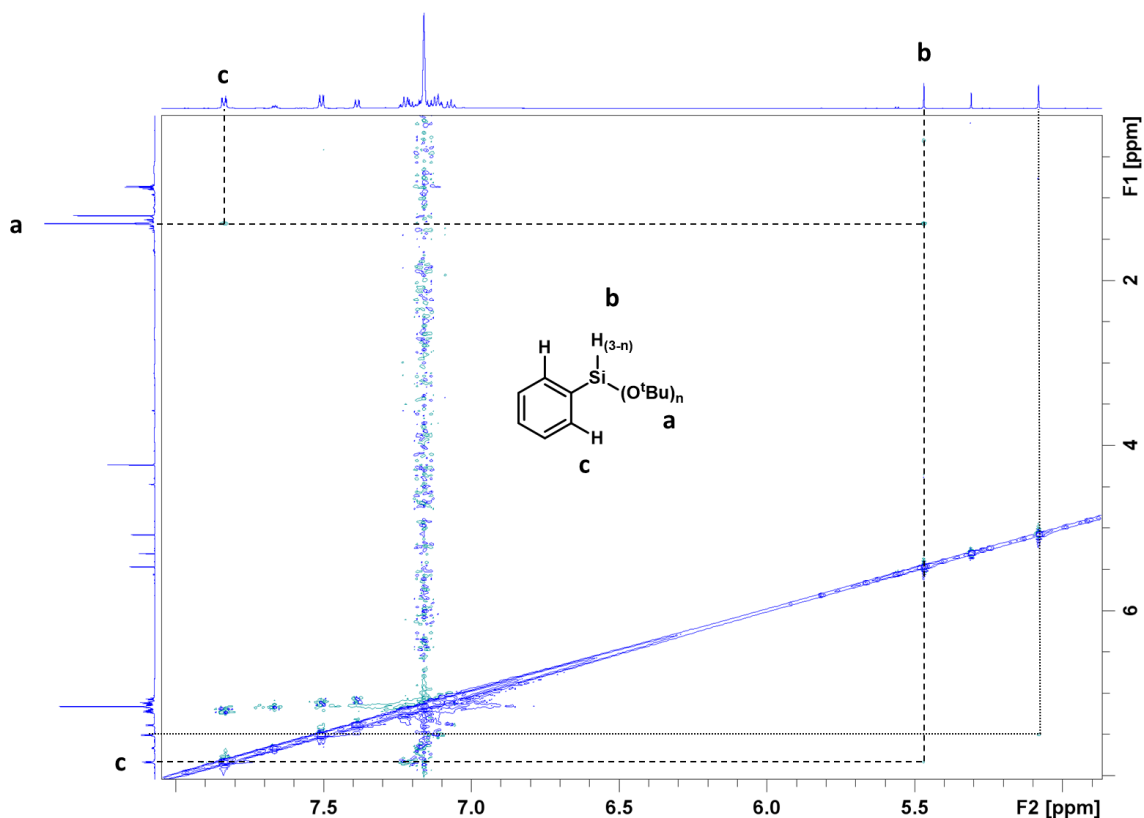


**Figure 2.6.4** Nuclear Overhauser Effect Spectroscopy (NOESY) NMR spectrum of the reaction between PhSiH<sub>3</sub> and complex **2** after five days at 70 °C highlighting the aromatic region and the correspondence to the Si-H moiety and the *tert*-butoxide substituted ligand.

The ortho-CH peak at 7.83 ppm shows NOESY cross peaks to the SiH peak at 5.47 ppm and the *tert*-butoxide peak at 1.31 ppm. The relative integration of these peaks (presented in **Figure 2.6.5**) is 2:1:18, corresponding to di(*tert*-butoxy)phenylsilane in agreement with the  $^1\text{H}$  NMR data for this compound.<sup>92</sup> Additionally, the presence of hydrogen gas is noted at 4.47 ppm, indicating that reductive elimination of  $\text{H}_2$  proceeds as hypothesized. Other hydrosilanes are evident in **Figure 2.6.5**, with SiH peaks at 5.31 ppm and 5.08 ppm. One of these is presumably  $\text{PhSiH}_2(\text{O}^t\text{Bu})$ , but the NOESY peaks required for more definitive identification of this compound were not observed. However, the peak shifts observed in the  $^1\text{H}$  NMR spectrum are in agreement with the literature  $^1\text{H}$  NMR data for  $\text{PhSiH}_2(\text{O}^t\text{Bu})$ .<sup>93,94</sup>

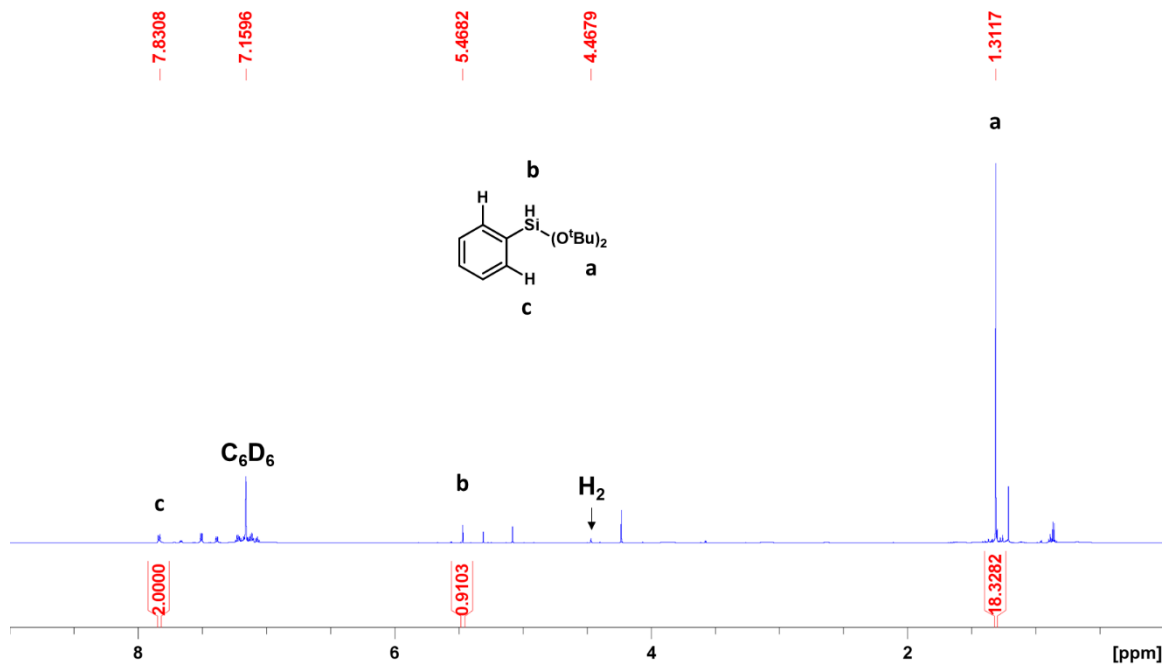


**Figure 2.6.5**  $^1\text{H}$  NMR spectrum ( $\text{C}_6\text{D}_6$ , 600 MHz,  $d_1=30\text{s}$ ) of the reaction between  $[\text{V}(\text{O}^t\text{Bu})_4]$  (**2**) and  $\text{PhSiH}_3$  in a J-Young tube after 5 days at  $70^\circ\text{C}$  indicating the major product of the reaction to be bis(*tert*-butoxy) phenyl silane.

Despite prolonged centrifugation, minimal precipitate was collected. In order to obtain a powder sample for analysis by PXRD, the reaction mixture was subjected to vacuum distillation (10 mTorr) using moderate heating. The distillate was collected, and the remaining black material was isolated. However, when attempting to scrape the black material from the round bottom flask, the material was found to be a sticky substance, making it clump together and stick to the metal spatula. Consequently, it could not be packed in a capillary for analysis by PXRD.

## 2.7 Reactivity Studies with decamethylsilicocene (**3**), and 1,4-bis(trimethylsilyl)-2-methyl-2,5-cyclohexadiene (**4**)

Provided that the reactivity of complexes **1** and **2**, with PhSiH<sub>3</sub> occurred at elevated temperatures and required extended periods of time to proceed to completion, PhSiH<sub>3</sub> may not be an ideal co-reagent for the development of an ALD process. As previously mentioned in Section 2.1 and presented in **Figure 2.1.1**, decamethylsilicocene (**3**), and 1,4-bis(trimethylsilyl)-2-methyl-2,5-cyclohexadiene (**4**) were also synthesized, for investigation as potential co-reagents. However, neither of these potential co-reagents reacted with **1** or **2**, even at elevated temperatures (60-90 °C) in C<sub>6</sub>D<sub>6</sub>. A summary of all attempted solution state reactivity studies is presented in **Table 2.7.1**.

**Table 2.7.1** Summary of all attempted solution state reactivity between [Cr(O<sup>t</sup>Bu)<sub>4</sub>] (**1**), [V(O<sup>t</sup>Bu)<sub>4</sub>] (**2**), and potential co-reagents

Experiment	Conditions	Reactivity	Precipitation	PXRD
<b>1</b> + HBpin	RT/overnight	Yes	Yes	Amorphous
<b>2</b> + HBpin	RT/overnight	Yes	Yes	Amorphous
<b>1</b> + PhSiH <sub>3</sub>	60 °C/3 days	Yes	Yes	Amorphous
<b>2</b> + PhSiH <sub>3</sub>	70 °C/5 days	Yes	No	-
<b>1</b> + <b>3</b>	70 °C/overnight	No	-	-
<b>2</b> + <b>3</b>	60 °C/overnight	No	-	-
<b>1</b> + <b>4</b>	90 °C/overnight	No	-	-
<b>2</b> + <b>4</b>	65 °C/overnight	No	-	-

The reactions of complexes **1** and **2** with HBpin seem to be the most promising for the purposes of developing an ALD process. Therefore, these reactions were investigated in more detail, in the presence of an internal standard, *vide infra*.

## 2.8 Reactivity Studies with HBpin in the Presence of an Internal Standard

In reactions involving paramagnetic **1** and **2**, it is difficult to determine whether all *tert*-butoxide groups are released from the metal center because the very broad *tert*-butoxide signals for the starting material prevent accurate integration relative to the internal standard. Therefore, the following experiment was carried out: (1) an equimolar solution of **1** and hexamethylbenzene was prepared in C<sub>6</sub>D<sub>6</sub>, (2) the solution was divided into two NMR tubes, (3) excess trifluoroacetic acid (TFA) was added to one tube in order to release all four *tert*-butoxide groups as *tert*-butanol, (4) the solution in the other tube was reacted with excess HBpin. Both solutions were allowed to react overnight, at which point the reaction products were integrated relative to the internal standard (hexamethylbenzene), enabling accurate determination of the number of equivalents of <sup>1</sup>BuO-Bpin in the reaction with HBpin. This experiment is visually illustrated in **Figure 2.8.1**.

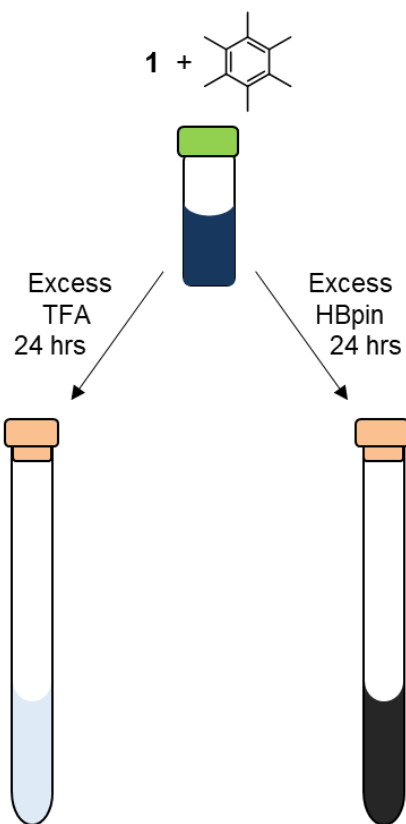


**Figure 2.8.1** Diagram illustrating the method for use of an internal standard to monitor the degree of reactivity between **1** and HBpin.

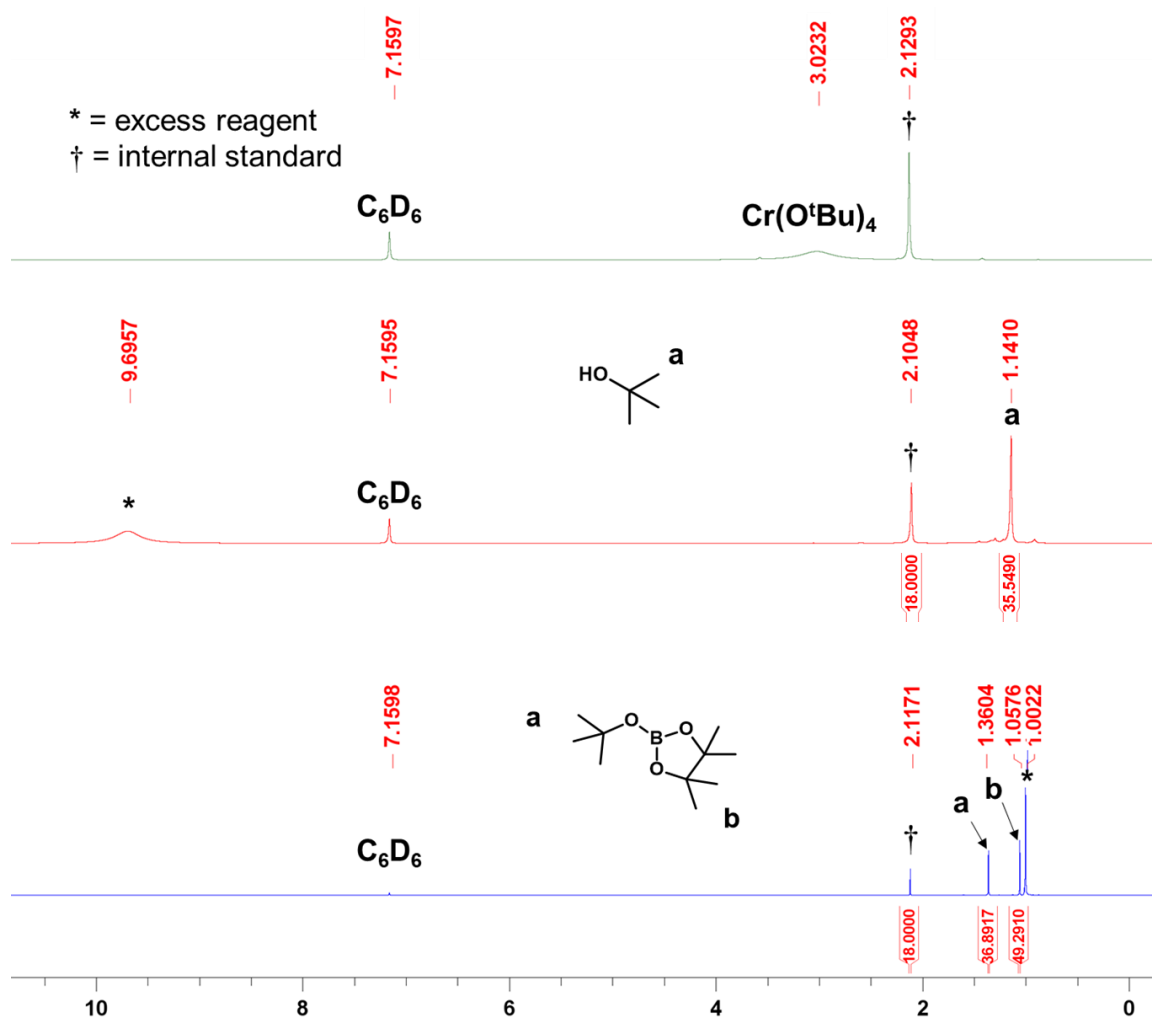


**Figure 2.8.2**  $^1\text{H}$  NMR spectra ( $\text{C}_6\text{D}_6$ , 600 MHz) of  $[\text{Cr}(\text{O}^t\text{Bu})_4]$  (**1**) and hexamethylbenzene as an internal standard (top, green), the reaction between  $[\text{Cr}(\text{O}^t\text{Bu})_4]$  (**1**) and excess TFA in the presence of an internal standard in a J-Young tube after 24 hours at room temperature (middle, red), and the reaction between  $[\text{Cr}(\text{O}^t\text{Bu})_4]$  (**1**) and excess HBpin in the presence of an internal standard in a J-Young tube after 24 hours at room temperature (bottom, blue).

As indicated in the  $^1\text{H}$  NMR spectra in **Figure 2.8.2**, the reaction of **1** with excess TFA afforded *tert*-butanol with an integration of 36H relative to hexamethylbenzene (18H). This is indicative of the generation of four equivalents of *tert*-butanol with respect

to one equivalent of the internal standard, indicating that the reaction with TFA is successful in removing all four *tert*-butoxide ligands from the metal center. In the reaction of **1** with HBpin, the *tert*-butoxide and the C(CH<sub>3</sub>)<sub>2</sub> protons of the <sup>t</sup>BuO-Bpin product integrate to 37H and 49H, respectively, relative to hexamethylbenzene (18H). The observed integrations are very close to the expected values of 36H and 48H indicating that the reaction proceeds to remove all four *tert*-butoxide ligands from complex **1**, presumably forming either a chromium hydride or chromium metal.

This analysis was replicated using vanadium complex **2** and HBpin using hexamethylbenzene as an internal standard. However, the reaction between **2** and TFA resulted in the precipitation of a viscous polymer like material that prohibited shimming of the NMR spectrometer. This prevented the adequate analysis of the integrations of the products generated with respect to the internal standard. However, the reaction between **2** and HBpin was allowed to proceed overnight, after which time the suspension was centrifuged, and the supernatant was decanted affording the <sup>1</sup>H NMR spectrum in **Figure 2.8.3**.

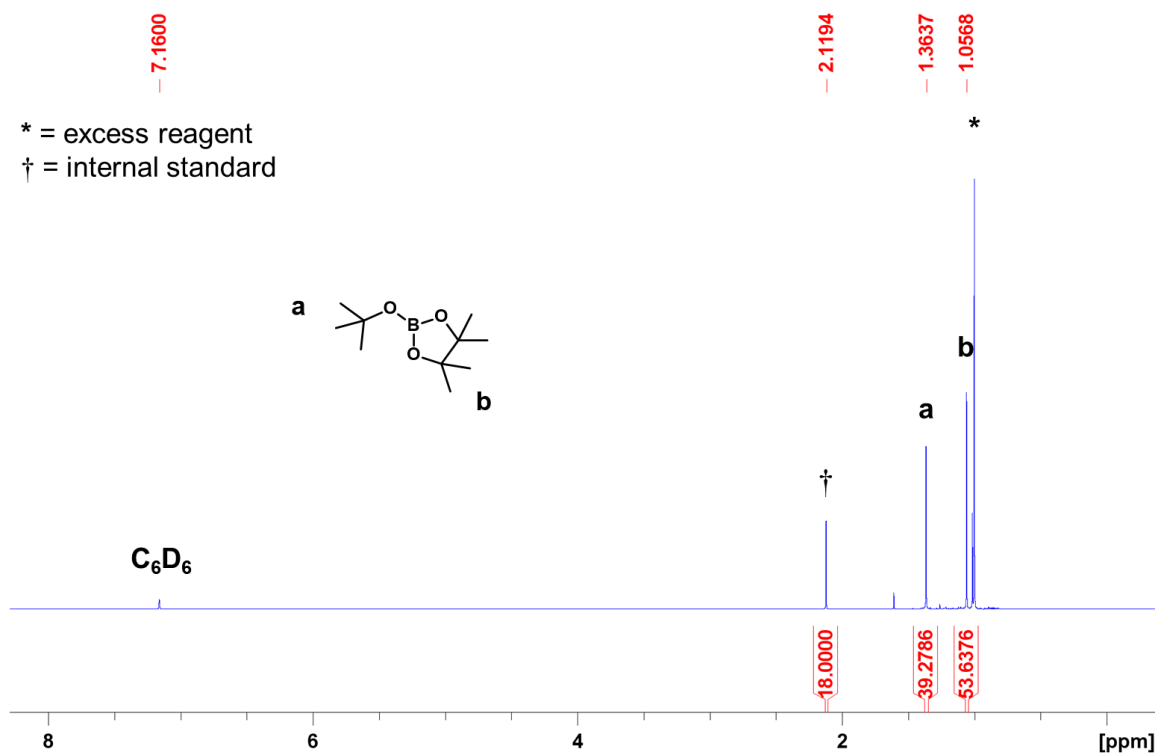


**Figure 2.8.3**  $^1\text{H}$  NMR spectrum ( $\text{C}_6\text{D}_6$ , 600 MHz) of the reaction between  $[\text{V}(\text{O}^t\text{Bu})_4]$  (**2**) and excess HBpin with hexamethylbenzene as an internal standard in a J-Young tube after 24 hours at room temperature.

As in the reaction of **1** with HBpin, integrations of the *tert*-butoxide and the  $\text{C}(\text{CH}_3)_2$  protons of the  $^t\text{BuO-Bpin}$  product are expected to be 36H and 48H, respectively. The observed values are 39H and 54H, relative to hexamethylbenzene (18H), which are 10% higher than expected, likely due to minor errors in the masses of **2** and hexamethylbenzene used in the experiment. This experiment suggests that all *tert*-butoxide ligands are displaced in the reaction of **2** with HBpin, as required in the proposed reaction pathway for vanadium ALD (**Scheme 2.1.1**).

### 3 Perfluoro-*tert*-butoxide Complexes of Vanadium and Chromium

Chapter 2 described promising reactivity between  $[M(O^tBu)_4]$  ( $M = Cr$  (**1**) or  $V$  (**2**)) and HBpin. However, the thermal stability of these complexes was somewhat limited. Decomposition of **1** and **2** afforded isobutene with varying amounts of *tert*-butanol (more for **1** than **2**), and was proposed to involve initial deprotonation at the  $\gamma$ -position of the *tert*-butoxide ligand. This chapter explores the synthesis of perfluoro-*tert*-butoxide (pftb) complexes of chromium and vanadium, since pftb ligands will not be susceptible to the aforementioned  $\gamma$ -deprotonation. Additionally, fluorinated ligands often afford complexes with increased volatility, which would be beneficial for an ALD precursor.<sup>95</sup>

Perfluoro-*tert*-butoxide (pftb) ligands are expected to differ considerably from *tert*-butoxide ligands in terms of their electronic and steric properties. Specifically, they will be much less electron-donating and significantly bulkier, likely influencing metal-ligand bond strength, the potential to install four alkoxide ligands on the metal center, redox chemistry of the central metal, and reactivity with co-reagents.

#### 3.1 Synthesis and Characterization

In an initial attempt to synthesize  $[Cr(pftb)_4]$  and  $[V(pftb)_4]$ , the non-fluorinated complexes,  $[Cr(O^tBu)_4]$  (**1**) and  $[V(O^tBu)_4]$  (**2**), were reacted with the fluorinated alcohol (Hpftb). It was suspected the strongly acidic nature of Hpftb ( $pK_a$  5.2; cf. 16.5 for *tert*-butanol)<sup>96,97</sup> would result in complete substitution of the *tert*-butoxide ligands, as illustrated in **Scheme 3.1.1**. However, attempts to synthesize the target compounds

through this pathway were unsuccessful; minimal consumption of the starting materials was observed even after 48 hours at 60 °C.



**Scheme 3.1.1** Proposed synthetic route to synthesize  $[\text{M}(\text{pftb})_4]$  ( $\text{M} = \text{Cr}$  or  $\text{V}$ ).

As an alternative, reactions of  $\text{Kpftb}$  with  $[\text{CrCl}_3(\text{THF})_3]$  and  $[\text{VCl}_3(\text{THF})_3]$  were explored. These reactions were unaffected by the addition of  $\text{CuCl}$ , so only reactions carried in the absence of  $\text{CuCl}$  are described.

The reaction of  $[\text{CrCl}_3(\text{THF})_3]$  (250 mg) with 4 equivalents of  $\text{Kpftb}$  (732 mg) was carried out in THF at 60 °C. After 24 hours, the purple solution had become a deep blue colour, and  $\text{KCl}$  was removed by filtration. The filtrate was evaporated to dryness *in vacuo* to afford a deep blue residue which was dissolved in a minimal volume of warm toluene and then cooled to -30 °C. This afforded a blue solid and a pale blue supernatant, and the crystallization procedure was repeated two more times. Utilizing this purification method, 439 mg of a blue solid material was isolated. A  $^{19}\text{F}$  NMR spectrum of this solid is presented in **Figure 3.1.1**.

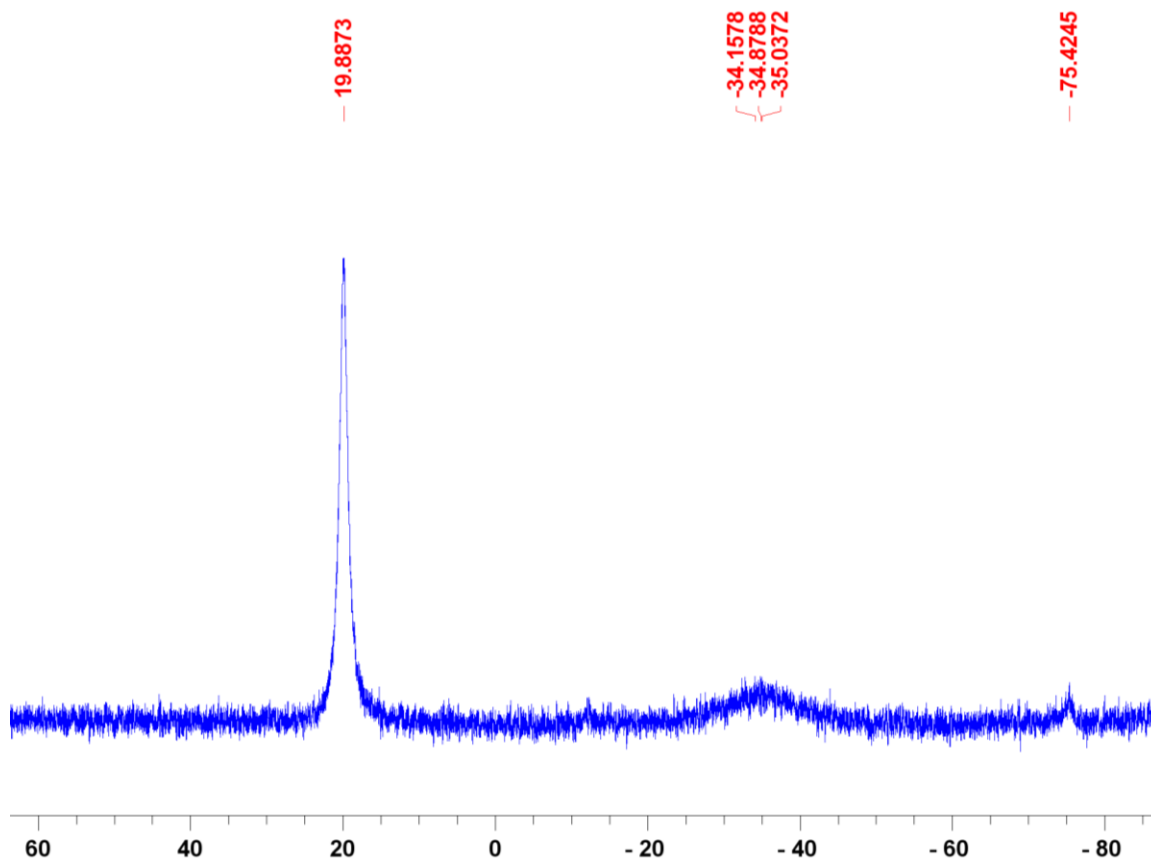


**Figure 3.1.1**  $^{19}\text{F}$  NMR spectrum (THF, 188 MHz, externally referenced to  $\text{CFCl}_3$ ) of the isolated material from the reaction between  $\text{CrCl}_3 \cdot 3\text{THF}$  and 4 equivalents of Kpftb after 24 hours at 60 °C.

The signal at  $-75$  ppm is due to residual Kpftb which seems to persist in solution despite the accurate control of stoichiometry. The purification of the material through fractional crystallization seems to reduce the concentration of Kpftb. However, the material is always present in small concentrations by NMR spectroscopy. This observation will be discussed further on page 68.

Crystallization of the blue residue from toluene at  $-30$  °C afforded large purple blocks which gave rise to a  $^{19}\text{F}$  NMR signal at  $-35$  ppm. These crystals were analyzed by



bonds are significantly shorter, as expected for an anionic ligand. The Cr–Cl bond (2.2489(5) Å) is shorter than the Cr–Cl bonds in [CrCl<sub>3</sub>(THF)<sub>3</sub>] (2.3130(6), 2.2931(6), and 2.3205(6) Å) likely due to a more electron-deficient metal center, due to the strong electron-withdrawing character of the pftb ligands.<sup>98</sup> Additionally, the structure is distorted from ideal octahedral geometry as indicated by the O(2)–Cr–O(4) bond angle (166.80(5)° versus the ideal 180° bond angle). Selected bond distances and angles for **5** are presented in **Table 3.1.1**.

**Table 3.1.1** Selected bond distances (Å) and angles (°) from the obtained crystal structure of [CrCl(pftb)<sub>2</sub>(THF)<sub>3</sub>] (**5**) highlighting the distorted octahedral geometry

	Bond Distance (Å)		Bond Angle (°)	
Cr–O(1)	2.045(1)	O(1)–Cr–O(3)	175.56(5)	
Cr–O(2)	1.954(1)	O(2)–Cr–O(4)	166.80(5)	
Cr–O(3)	2.041(1)	Cl–Cr–O(1)	93.07(3)	
Cr–O(4)	1.946(1)	Cl–Cr–O(2)	96.80(4)	
Cr–O(5)	2.089(1)	Cl–Cr–O(3)	91.30(3)	
Cr–Cl	2.2489(5)	Cl–Cr–O(4)	96.22(4)	
		Cl–Cr–O(5)	176.31(3)	

The supernatant from the crystallization of **5** was allowed to remain at ambient glovebox temperature (roughly 22 °C), which permitted the growth of new crystals. The crystals obtained were long deep blue needles but could not be solved due to extensive twinning. Differing solvent systems and growth conditions did not yield crystals of

higher quality for analysis. These crystals may correspond to the major species at 20 ppm in the  $^{19}\text{F}$  NMR spectrum, but this major product could not be identified.

Our inability to completely remove  $\text{Kpftb}$  from the reaction mixture was surprising, so a solution of the sample in THF was analyzed by NMR spectroscopy over a period of time (**Figure 3.1.3**). It was noted that the peak corresponding to  $\text{Kpftb}$  grew in intensity over time, which seems to indicate that the major species ( $^{19}\text{F}$   $\delta$  19.9 ppm) slowly dissociates  $\text{Kpftb}$  in conjunction with the growth of a small peak at  $-12$  ppm. This observation (and the formation of  $\text{K}[\text{V}(\text{pftb})_4]$  from the analogous reaction with  $[\text{VCl}_3(\text{THF})_3]$ ; *vide infra*) indicates that the major product may be  $\text{K}[\text{Cr}(\text{pftb})_4]$ .

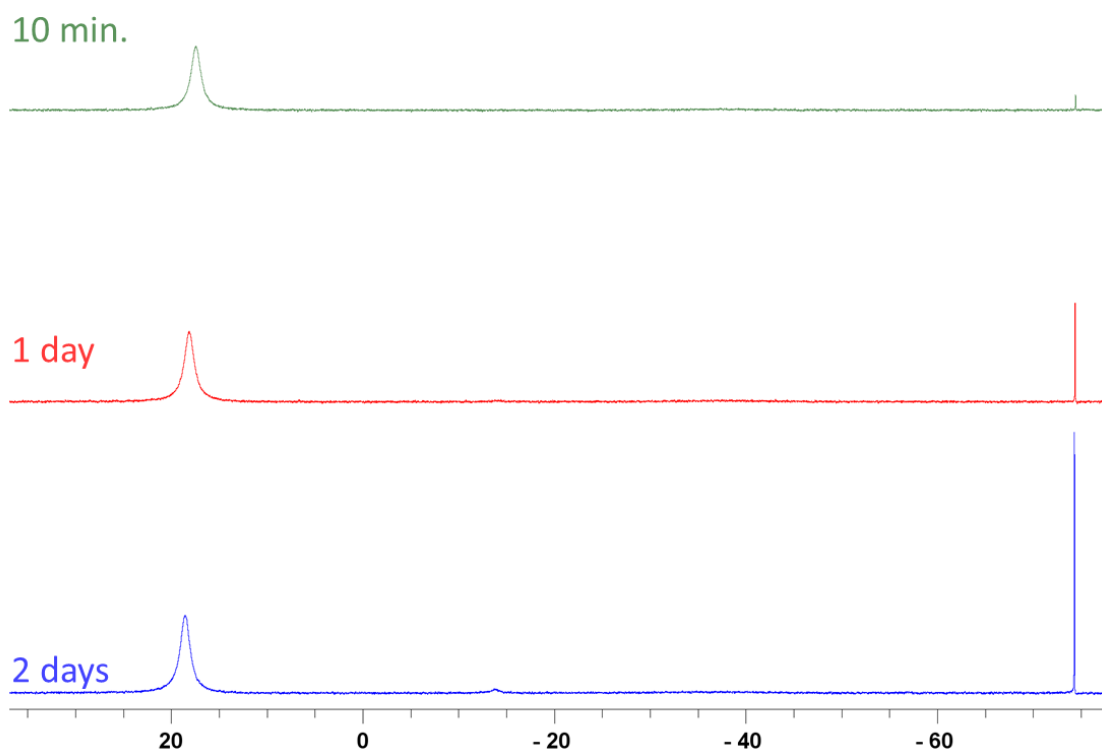


**Figure 3.1.3**  $^{19}\text{F}$  NMR spectra (THF, 188 MHz, externally referenced to  $\text{CFCl}_3$ ) of the major species from the reaction between  $[\text{CrCl}_3(\text{THF})_3]$  and 4 equivalents of  $\text{Kpftb}$  over

the course of two days, showing an increase in intensity of the signal corresponding to Kpftb at  $-75$  ppm, and the growth of a baseline peak at  $-12$  ppm.

In an attempt to isolate the minor species at  $-35$  ppm corresponding to  $[\text{CrCl}(\text{pftb})_2(\text{THF})_3]$  (**5**), the reaction between  $[\text{CrCl}_3(\text{THF})_3]$  and Kpftb was repeated using 2 equivalents of Kpftb. The reaction was conducted at  $60$  °C in an effort to replicate the previous synthesis parameters. However, this seemed to push the reaction to the major product in a similar manner to the reaction using four equivalents of Kpftb. The  $^{19}\text{F}$  NMR spectrum of this experiment is presented in **Figure 3.1.4**.

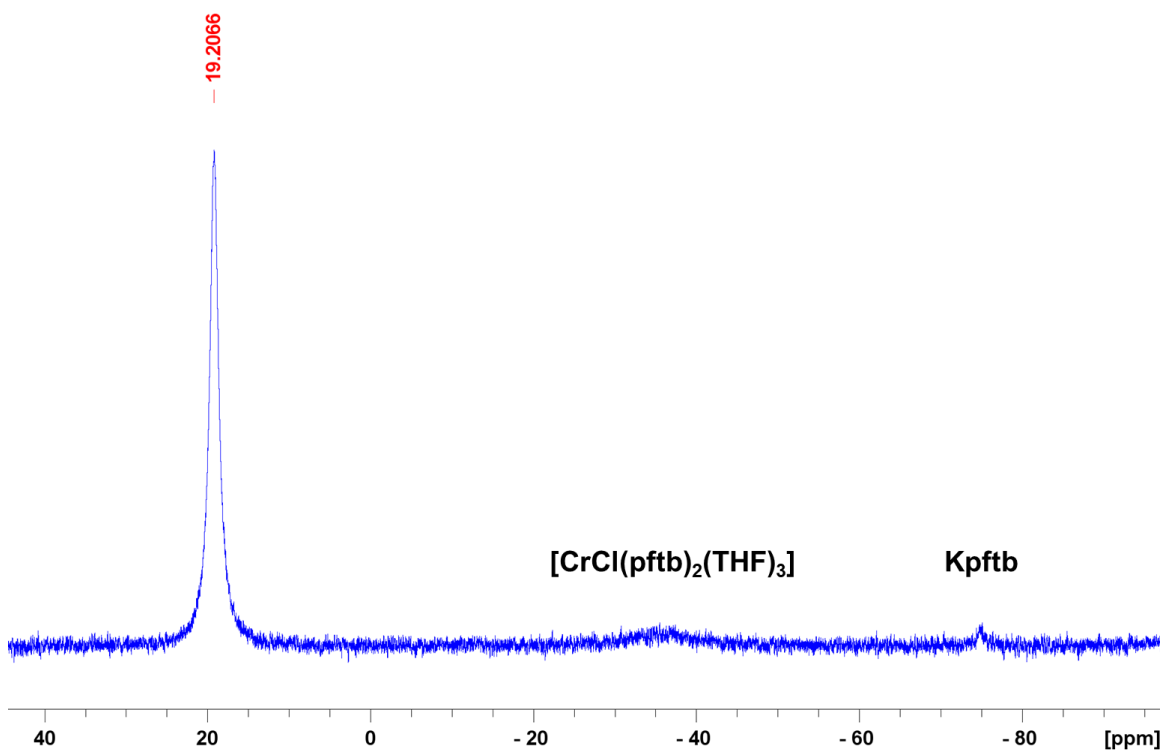


**Figure 3.1.4**  $^{19}\text{F}$  NMR spectrum (THF, 188 MHz, externally referenced to  $\text{CFCl}_3$ ) of the reaction between  $[\text{CrCl}_3(\text{THF})_3]$  and 2 equivalents of Kpftb after 24 hours at  $60$  °C.

The reaction was then repeated at room temperature using 2 equivalents of Kpftb, which also resulted in the formation of a mixture of both species but now complex **5** was the major product. The  $^{19}\text{F}$  NMR spectrum of this experiment is presented in **Figure 3.1.5**. Sublimation was employed in an attempt to isolate complex **5**. However, both species sublimed simultaneously, despite accurate control of the sublimation temperature over a range of temperatures (40-90 °C) at 10 mTorr. Attempts to isolate pure samples of complex **5** were not successful because the other product (that giving rise to a  $^{19}\text{F}$  NMR signal at 20 ppm) always co-precipitated as a powder under the crystallization conditions employed.

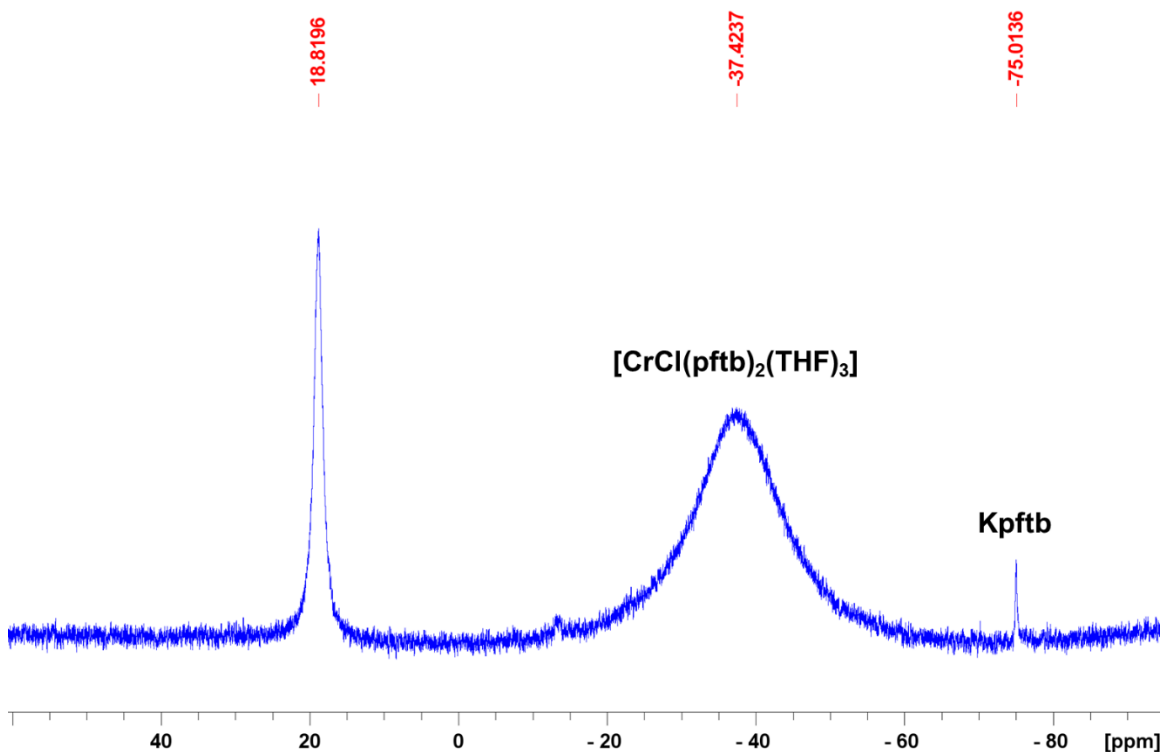


**Figure 3.1.5**  $^{19}\text{F}$  NMR spectrum (THF, 188 MHz, externally referenced to  $\text{CFCl}_3$ ) of the reaction between  $[\text{CrCl}_3(\text{THF})_3]$  and 2 equivalents of Kpftb after 24 hours at room temperature.

Switching focus to vanadium, reaction of  $[\text{VCl}_3(\text{THF})_3]$  (250 mg) with four equivalents of Kpftb (734 mg) in THF at room temperature resulted in an immediate solution colour change from pink to deep blue. After 1 hour, the solution was filtered to remove KCl, and recrystallized three times by cooling a warm toluene solution to  $-30^\circ\text{C}$ , affording 703 mg of a purple solid.

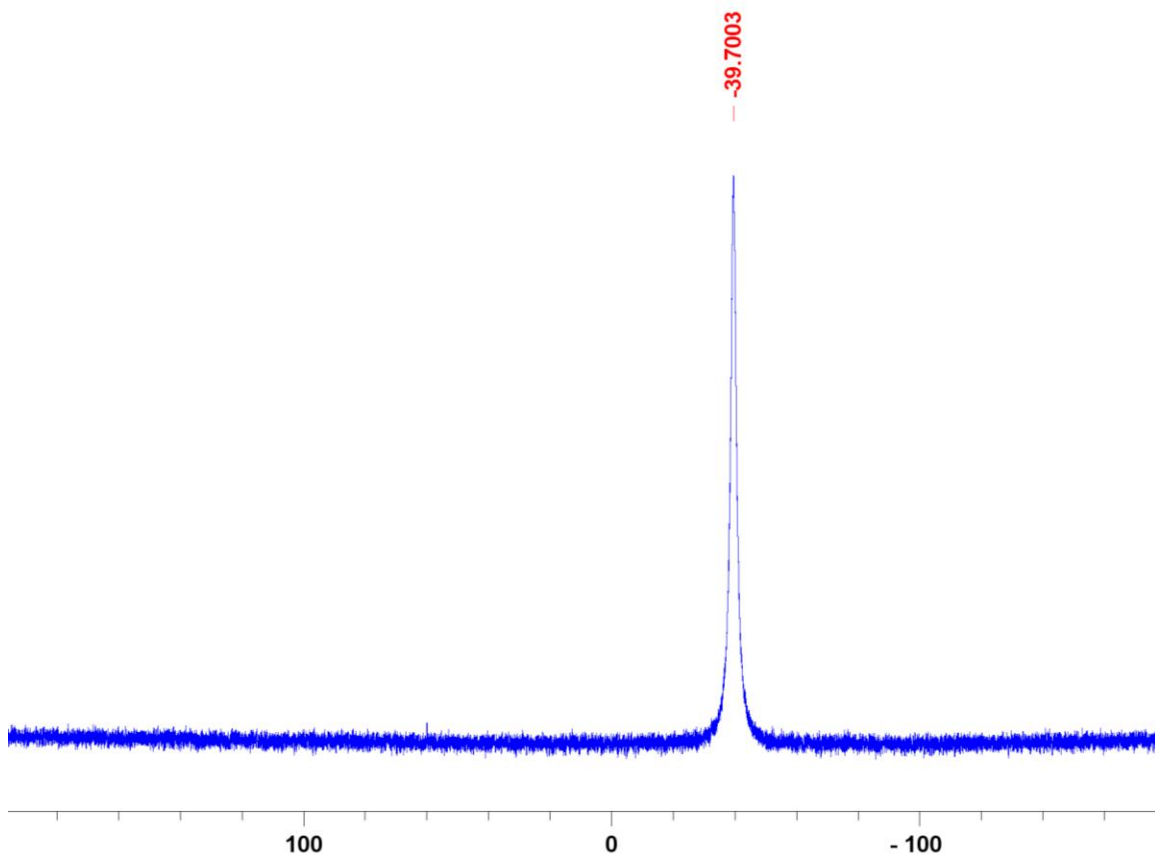


**Figure 3.1.6**  $^{19}\text{F}$  NMR spectrum (THF, 188 MHz, externally referenced to  $\text{CFCl}_3$ ) of the isolated product from the reaction between  $[\text{VCl}_3(\text{THF})_3]$  and 4 equivalents of Kpftb.

The  $^{19}\text{F}$  NMR spectrum of the isolated material is presented in **Figure 3.1.6** showing that the isolated material is free from any residual Kpftb or any other contaminants. Additionally, the  $^1\text{H}$  NMR spectrum in  $d_8$ -THF showed only trace amounts



Vanadium is coordinated to four pftb ligands, two of which bridge to a potassium cation. The potassium cation is  $\eta^3$ -coordinated to toluene (K–C = 3.219(9) Å (para), 3.36(1) and 3.28(1) Å (meta), 3.56(1) and 3.452(9) Å (ortho), and 3.63(1) Å (ipso)), and also engages in intramolecular and intermolecular K $\cdots$ F contacts (K $\cdots$ F = 3.214(5) and 2.697(6) Å (intramolecular), and 3.126(6) and 3.199(5) Å (intermolecular)). The V–O distances are shorter (1.843(5) and 1.833(4) Å) for the terminal pftb ligands and longer (1.919(6) and 1.894(4) Å) for the bridging pftb ligands. Additionally, the geometry of the obtained structure is distorted from the ideal tetrahedral geometry at vanadium. Specifically, the O(1)–V–O(2) bond angle involving the two bridging pftb ligands is 95.2(2)°, which is much smaller than expected (109.5°) for the given geometry. This distortion may occur in order to maximize interactions with the potassium cation. The V–O–C angles are also significantly different for the terminal versus the bridging pftb ligands; 149.5(5)° and 149.0(5)° for the former, and 138.2(4)° and 136.2(4)° for the latter.

**Table 3.1.2** Selected bond distances (Å) and angles (°) from the obtained crystal structure of  $[(\eta^3\text{-Tol})\text{K}(\mu\text{-pftb})_2\text{V}(\text{pftb})_2] \cdot \mathbf{6}(\text{toluene})$ , highlighting the distorted tetrahedral geometry

	Bond Distance (Å)		Bond Angle (°)	
V–O(1)	1.894(4)	O(1)–V–O(2)	95.2(2)	
V–O(2)	1.919(6)	O(1)–V–O(3)	105.2(2)	
V–O(3)	1.833(4)	O(1)–V–O(4)	110.4(2)	
V–O(4)	1.843(5)	O(2)–V–O(3)	113.3(2)	
K–O(1)	3.148(6)	O(2)–V–O(4)	119.8(2)	
K–O(2)	3.069(5)	O(3)–V–O(4)	110.8(2)	
K–C(para)	3.219(9)	V–O(1)–C	177.3(3)	
K–C(meta)	3.36(1), 3.28(1)	V–O(2)–C	136.2(4)	
K–C(ortho)	3.56(1), 3.452(9)	V–O(3)–C	149.5(5)	
K–C(ipso)	3.63(1)	V–O(4)–C	149.0(5)	

Solutions of complex **6** were observed, by  $^{19}\text{F}$  NMR spectroscopy, to slowly regenerate Kpftb over time as shown in **Figure 3.1.8**. This phenomenon was previously observed for the chromium pftb complex with a  $^{19}\text{F}$  chemical shift of 20 ppm (hypothesized to be  $\text{K}[\text{Cr}(\text{pftb})_4]$ ; *vide supra*). Additionally, a small peak at –45 ppm is observed to grow over time, concurrent with Kpftb formation.

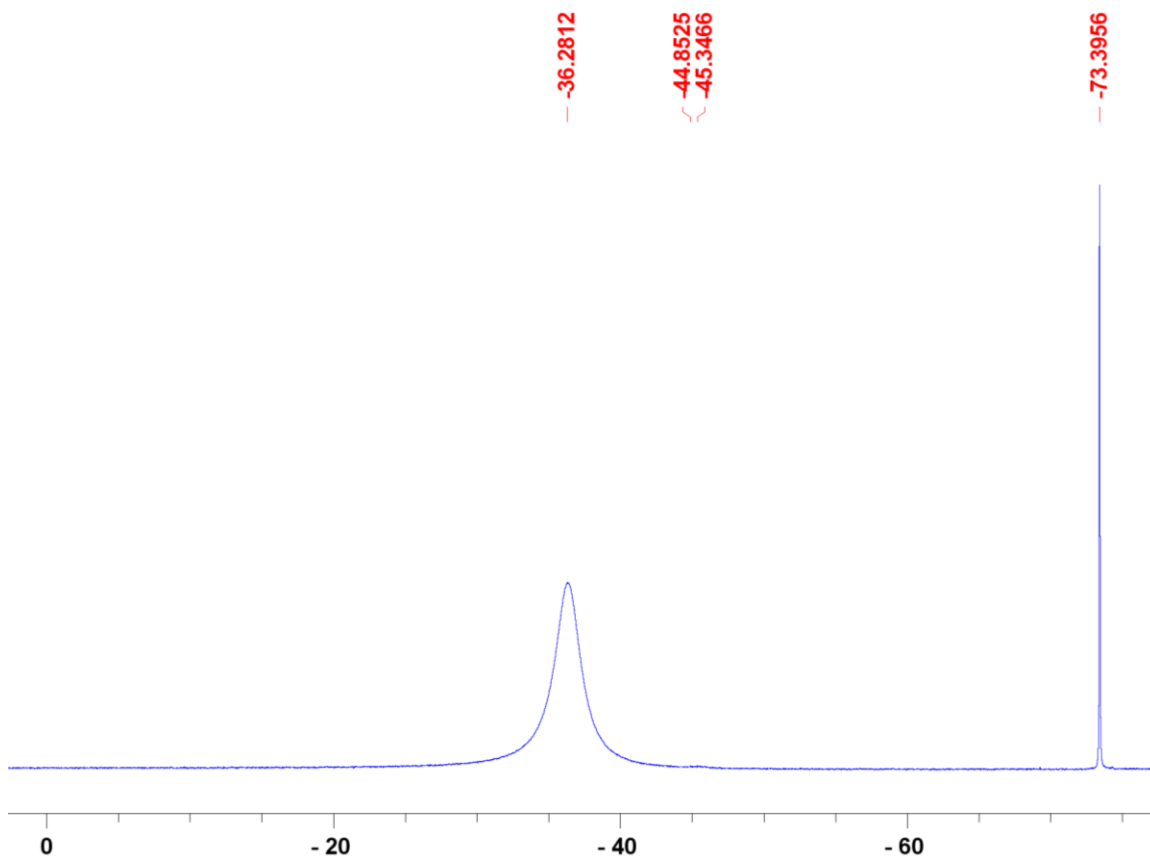


**Figure 3.1.8**  $^{19}\text{F}$  NMR spectrum (THF, 188 MHz, externally referenced to  $\text{CFCl}_3$ ) of complex **6** after being left in solution for 8 days, indicating growth of the peak at  $-73$  ppm corresponding to  $\text{Kpftb}$ .

### 3.2 Elemental Analysis and PXRD of $\text{K}[\text{V}(\text{pftb})_4]$ (**6**)

Elemental analysis of the bulk sample of **6** afforded a %C value of 18.33% and a %H value of 0.07%, very close to the calculated values of 18.65% and 0.00% for toluene-free  $\text{K}[\text{V}(\text{pftb})_4]$  (**6**). Powder X-ray diffraction (PXRD) was also utilized to (1) verify that samples of **6** do not contain residual free  $\text{Kpftb}$ , (2) verify that samples of **6** do not contain significant amounts of **6**(toluene), and (3) determine whether samples of **6** which

had been dissolved in THF differ from those which had not been exposed to THF. **Figure 3.2.1** shows PXRDs for **6** and Kpftb. Although some peaks in the PXRDs overlap, the major peak for Kpftb at  $2\theta = 9.5^\circ$  is absent in the PXRD of **6**, indicating that isolated **6** does not contain free Kpftb.

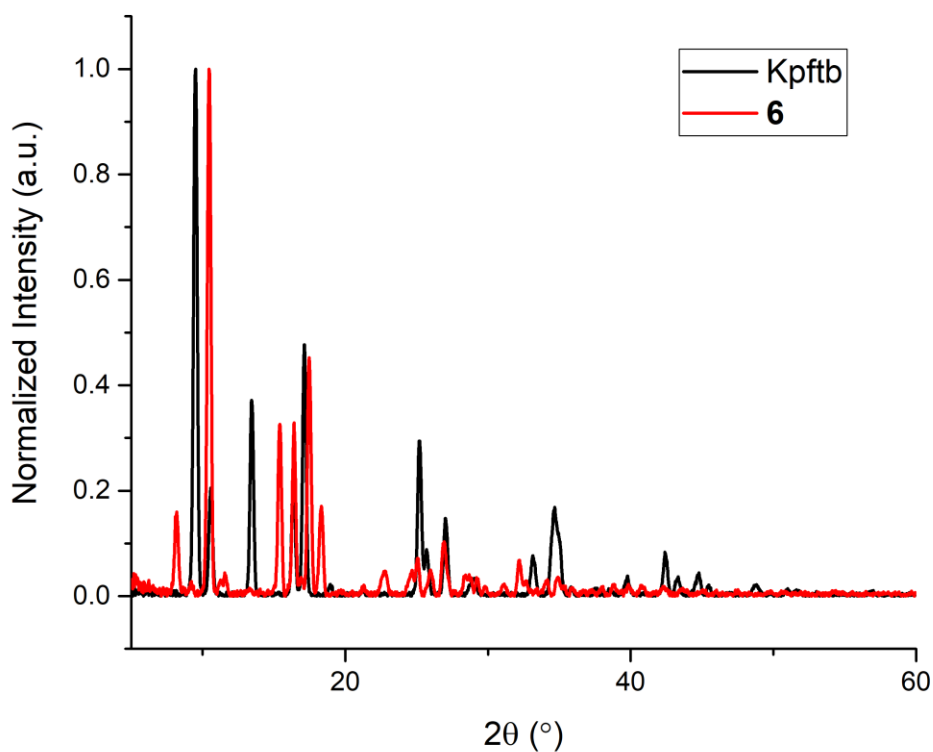


**Figure 3.2.1** PXRDs of Kpftb (black) and the bulk sample of complex **6** (red).

**Figure 3.2.2** compares the PXRD of **6** with the powder pattern calculated from the single crystal X-ray structure of **6**(toluene), and as expected based on  $^1\text{H}$  NMR spectroscopy and elemental analysis, samples of **6** do not contain **6**(toluene).

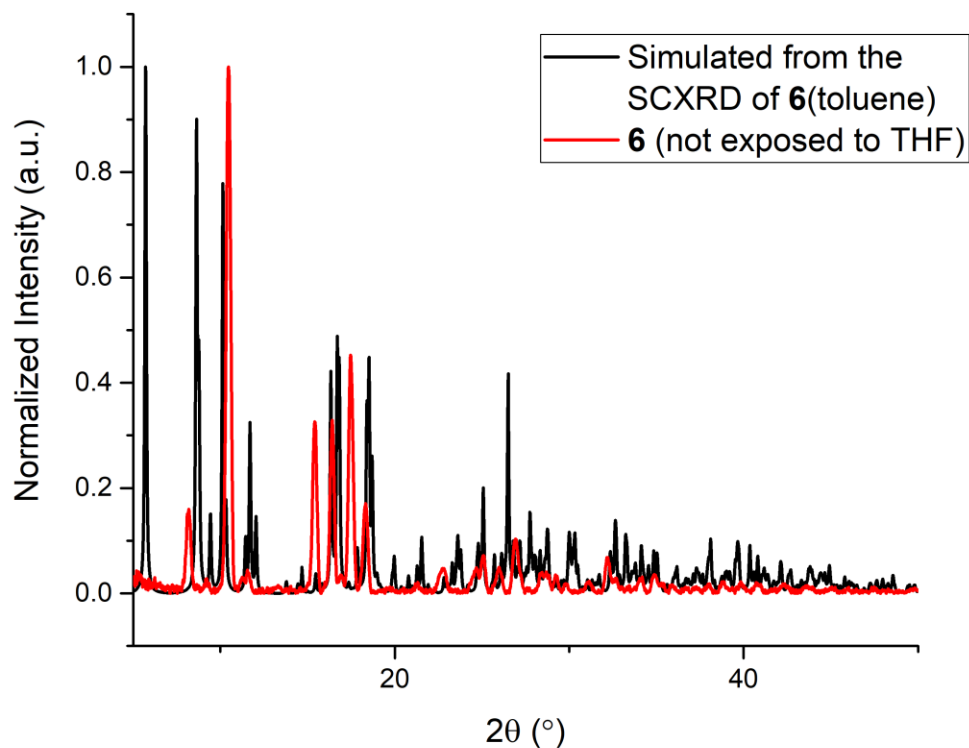


**Figure 3.2.2** PXR D of the bulk sample of **6** which was not exposed to THF; (red) and the simulated powder pattern obtained from the crystal structure of **6**(toluene) (black).

Finally, PXR Ds of samples of **6** which had or had not been exposed (dissolved post-crystallization and then evaporated to dryness *in vacuo*) to THF are shown in **Figure 3.2.3**. These PXR Ds overlap, indicating that samples of **6** which have been exposed to THF do not retain THF after drying *in vacuo*.

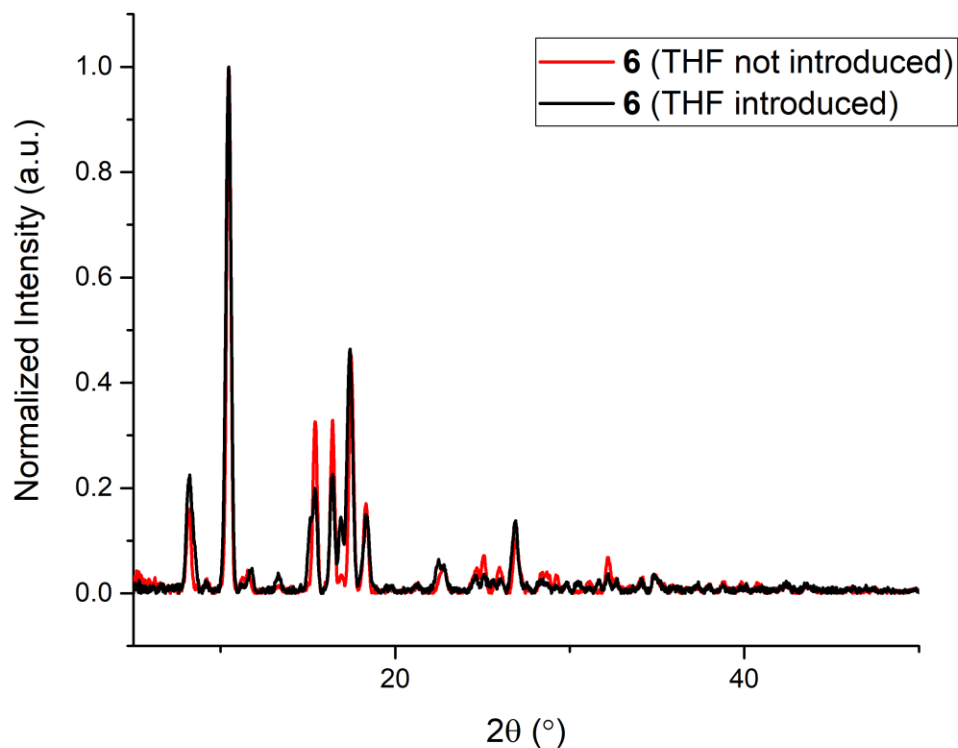


**Figure 3.2.3** PXRD of the sample of complex **6** that was not exposed to THF post-crystallization (red) and the sample of complex **6** that was exposed to THF post-crystallization (black) indicating no variability in the solid state.

### 3.3 Thermal Properties of $K[V(pftb)_4]$ (**6**)

The target vanadium complex at the outset of this work was  $[V(pftb)_4]$ , containing vanadium(IV). The isolated product,  $K[V(pftb)_4]$  (**6**) is structurally related to the target complex in that there are four pftb ligands on vanadium, but it is a complex of vanadium(III). It will not be useful as a precursor for vanadium metal ALD due to the presence of potassium in the structure. Nevertheless, the thermal stability of **6** was

evaluated to gain a preliminary understanding of whether facile decomposition pathways exist for pftb ligands in the coordination sphere of vanadium. Also, although not the focus of this work, **6** could potentially be useful for ALD of materials containing 1:1 ratio of K and V, such as  $\text{KVO}_3$ .

The thermal stability of complex **6** was determined by gradually heating a neat sample in a J-Young tube until visual decomposition was observed (discolouration) or reactivity was observed by NMR spectroscopy. Decomposition was observed after heating to 130 °C overnight, but even prolonged (72 hours) heating at 130 °C did not result in the complete decomposition. The temperature was increased to 140 °C, and the sample was still not fully decomposed after 24 hours. However, given that the onset of decomposition occurred at 130 °C, this is the limit of useful temperatures for precursor delivery in an ALD process. The  $^{19}\text{F}$  NMR spectrum of the products formed from thermal decomposition of complex **6** is displayed in **Figure 3.3.1**.

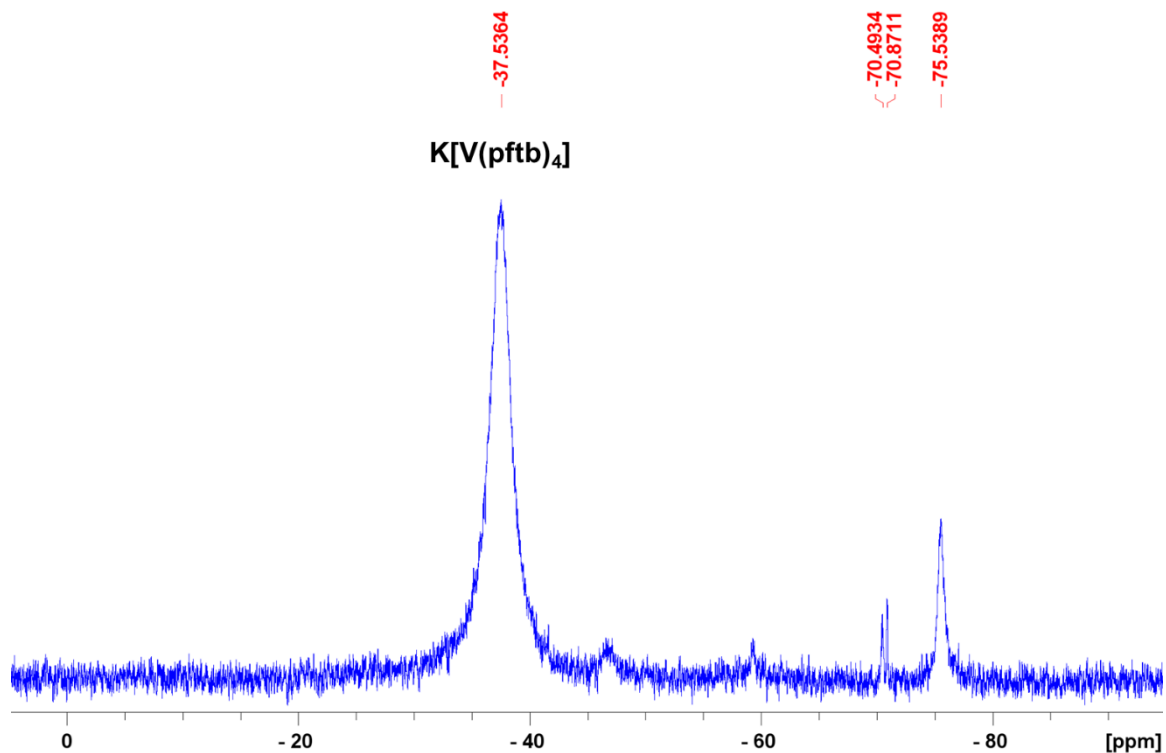


**Figure 3.3.1**  $^{19}\text{F}$  NMR spectrum (THF, 188 MHz, externally referenced to  $\text{CFCl}_3$ ) of the decomposition products formed from complex **6** after heating at 130 °C overnight.

The volatility of **6** was also assessed, resulting in sublimation at 75-85 °C (10 mTorr). The temperature required to deliver a precursor on an ALD reactor is typically around 40 °C above the sublimation temperature at 10 mTorr (because ALD reactors typically operate at pressures between 100 and 1000 mTorr). Applying this approximation, a delivery temperature of 115-125 °C may be feasible, given that this is 5-15 °C below the onset of decomposition (130 °C). To further probe the volatility and thermal stability of **6**, albeit at much higher pressure (760 Torr) and on a shorter timescale, a sample of complex **6** was analyzed by inert-atmosphere TGA, and is presented in **Figure 3.3.2**.

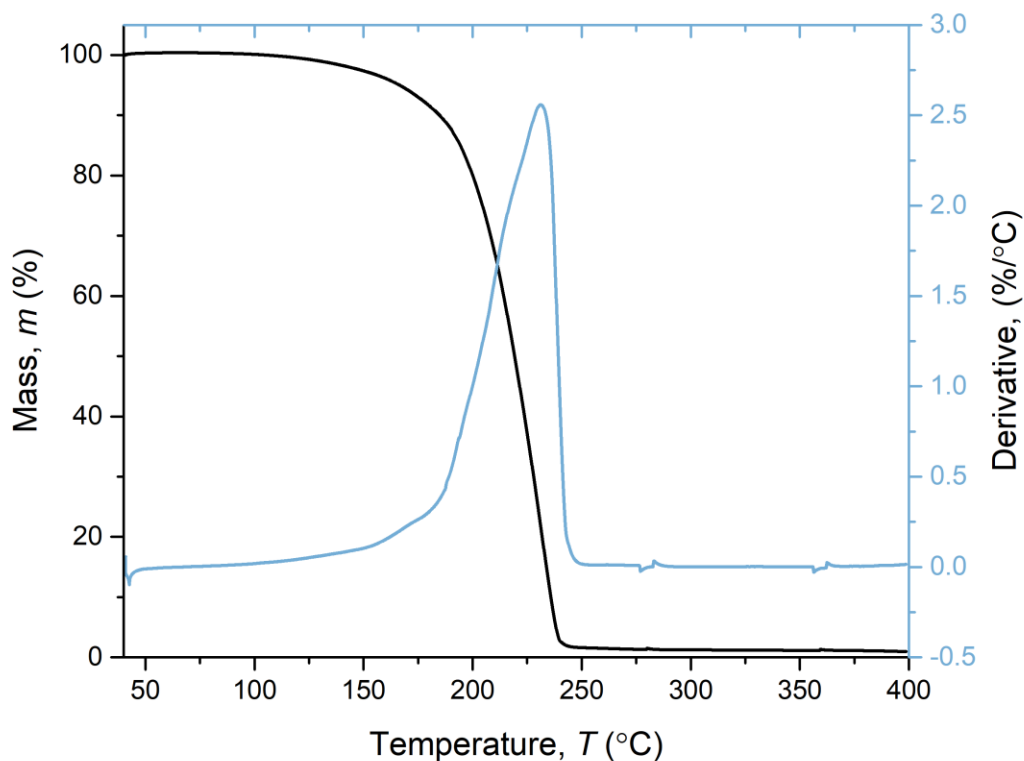


**Figure 3.3.2** TGA data for complex **6**, and the derivative curve expressed as the rate of change of the percentage mass with respect to temperature.

Analysis by TGA indicates that complex **6** exhibits complete volatilization with minimal decomposition. The  $\%m_{res}$  of **6** is 0.95% and the derivative curve indicates uniform volatilization.

### 3.4 Reactivity Studies with HBpin

Despite the unsuitability of **6** as an ALD precursor for metal deposition, complex **6** was reacted with HBpin in order to study the potential reactivity of the pftb ligands in comparison to the *tert*-butoxide ligands. As previously discussed in Section 2.5, the reaction between  $[V(O^tBu)_4]$  (**2**) and HBpin proceeds within 30 seconds at room temperature. By contrast, solutions of  $K[V(pftb)_4]$  (**6**) in THF-*d*<sub>8</sub> did not react with excess HBpin at 100 °C after 24 hours. The much lower reactivity of  $K[V(pftb)_4]$  (**6**) relative to  $[V(O^tBu)_4]$  may be due to substantially increased steric hindrance in **6**, the much more electron withdrawing nature of pftb versus *tert*-butoxide ligands, or differences in the reactivity of vanadium(III) versus vanadium(IV).

### 3.5 Reactivity Studies with PhSiH<sub>3</sub>

Solution reactivity studies between  $K[V(pftb)_4]$  (**6**) and excess PhSiH<sub>3</sub> were also attempted. No reactivity was observed by <sup>1</sup>H and <sup>19</sup>F NMR spectroscopy when the reaction mixture was left at room temperature. However, the starting complex had mostly been consumed after heating at 90 °C for 24 hours, affording several new peaks in the <sup>19</sup>F NMR spectrum between -73 and -78 ppm; **Figure 3.5.1**.

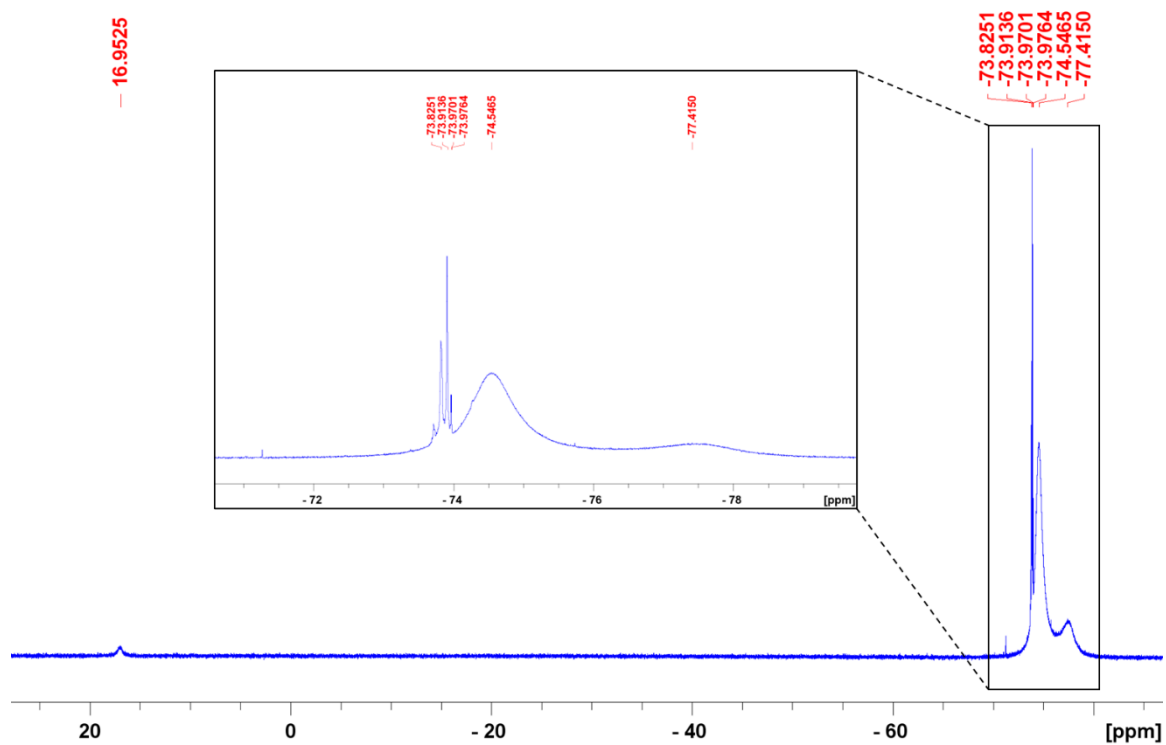


**Figure 3.5.1**  $^{19}\text{F}$  NMR spectrum ( $\text{THF-}d_8$ , 565 MHz) of the reaction between  $\text{K}[\text{V}(\text{pftb})_4]$  (**6**) and  $\text{PhSiH}_3$  after 24 hours at 90 °C.

The reaction did not result in any precipitation or colour changes (the solution maintained a deep purple colour). This reactivity is not indicative of any metal deposition. Additionally, neither new hydrosilane species nor dihydrogen were observed by  $^1\text{H}$  NMR spectroscopy (**Figure 3.5.2**). Consequently, the observed reactivity was not considered to be valuable for the purpose of metal ALD and was not investigated further.

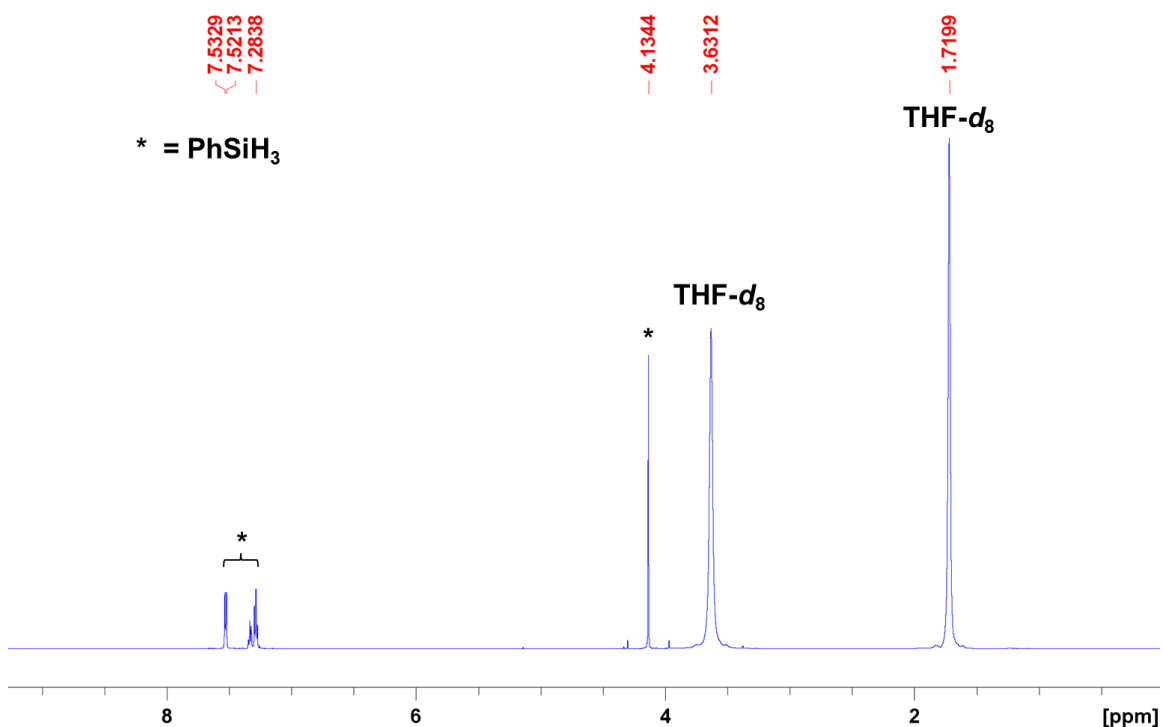


**Figure 3.5.2** <sup>1</sup>H NMR spectrum (THF-*d*<sub>8</sub>, 600 MHz) of the reaction between K[V(pftb)<sub>4</sub>] (**6**) and PhSiH<sub>3</sub> after 24 hours at 90 °C.

### 3.6 Cyclic Voltammograms of Complexes **6**, **1**, and **2**

The vanadium(III) complex K[V(pftb)<sub>4</sub>] (**6**) could be converted to the target neutral vanadium(IV) complex, [V(pftb)<sub>4</sub>], by one-electron oxidation. However, all attempts to access this complex by carrying out reactions between Kpftb (4 equivalents) and [VCl<sub>3</sub>(THF)<sub>3</sub>] in the presence of CuCl as an oxidizing agent were unsuccessful. In order to determine a more appropriate oxidizing agent, the redox potential of **6** must be determined. Cyclic voltammetry (CV) was utilized for this venture.

The CV of **6** was obtained in 1,2-difluorobenzene (DFB) using a 1 mM concentration of **6** and a 0.1 M concentration of the base electrolyte [NBu<sub>4</sub>][B(C<sub>6</sub>F<sub>5</sub>)<sub>4</sub>]. The working electrode was a 1.6 mm diameter platinum disk, the counter electrode was a platinum wire, and a silver wire was used as a pseudo-reference electrode. [FeCp\*<sub>2</sub>] was added as an internal calibrant at the end of the experiment (a separate CV of a mixture of [FeCp\*<sub>2</sub>] and [FeCp<sub>2</sub>] in DFB established that E<sub>1/2</sub> for [FeCp\*<sub>2</sub>]<sup>+0</sup> is -0.60 V versus [FeCp<sub>2</sub>]<sup>+0</sup>). All potential values are quoted relative to [FeCp<sub>2</sub>]<sup>+0</sup>.

Cyclic voltammograms of **6** are obtained at scan rates of 50, 100, 200, 500, and 1000 mV/s; presented in **Figure 3.6.1**. A plot of the anodic current (*i<sub>pf</sub>*) for the oxidation of **6** versus the square root of scan rate ( $\sqrt{v}$ ) is also provided in **Figure 3.6.2**. The plot shows a linear relationship, as expected based on the Randles-Sevcik equation (Equation 3), confirming that the CV was run under diffusion-controlled conditions.

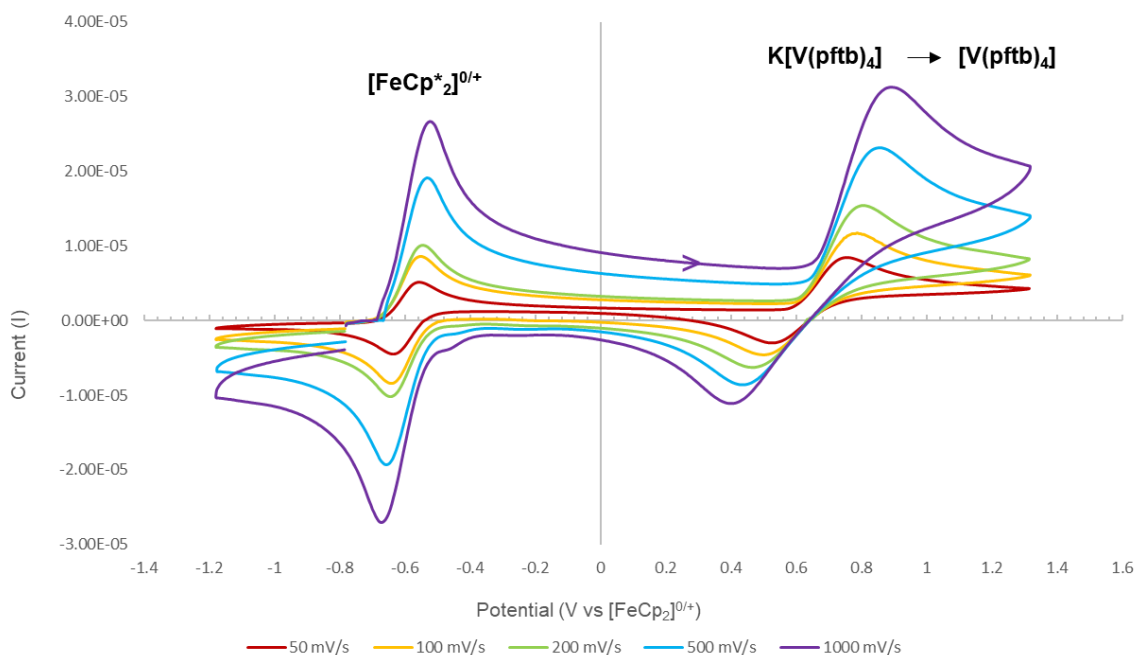


**Figure 3.6.1** Cyclic Voltammograms of  $K[V(pftb)_4]$  (**6**) and the internal calibrant  $[FeCp^*_2]^{+/0}$  ( $E_{1/2} = -597$  mV versus  $[FeCp_2]^{+/0}$  in 1,2-difluorobenzene (DFB)). Working and counter electrodes: Pt; pseudo-reference electrode:  $Ag^+/Ag$ ; base electrolyte:  $[NBu_4][B(C_6F_5)_4]$ .

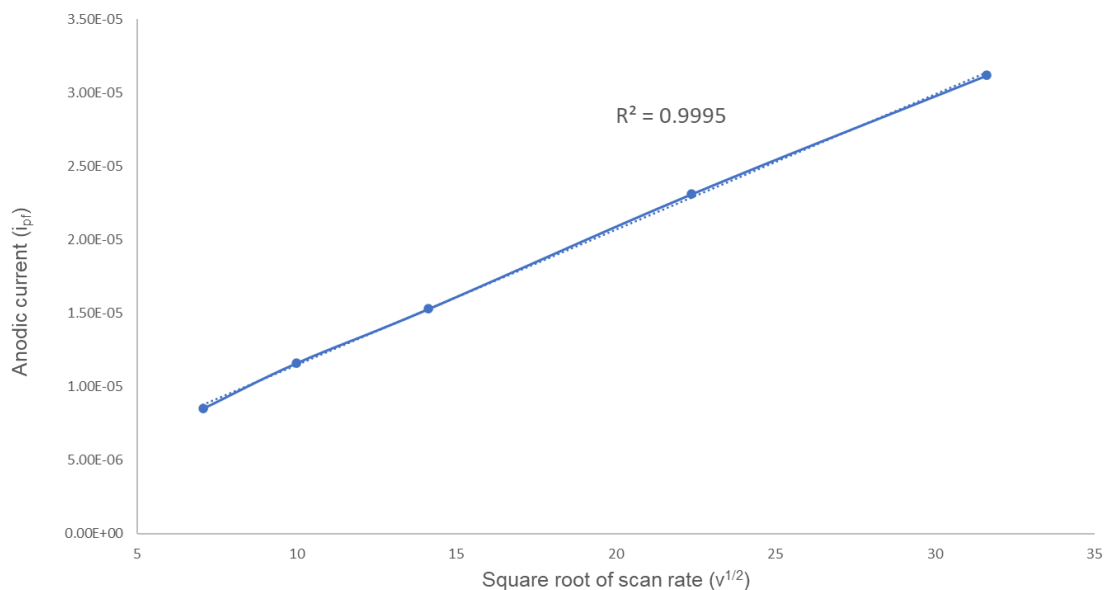


**Figure 3.6.2** Randles-Sevcik plot of the anodic current ( $i_{pf}$ ) of complex **6** versus the square root of the scan rate ( $v^{1/2}$ ) indicating linearity ( $R^2 = 0.9995$ ).

The CVs in **Figure 3.6.1** show that  $K[V(pftb)_4]$  (**6**) undergoes chemically reversible oxidation, given that both a forward and reverse peak are observed. However, compared with the wave for reversible oxidation of  $[FeCp^*_2]$ , that for **6** has a significantly greater peak-to-peak separation ( $\Delta E_p$ , **Table 3.6.1**), even though the forward peak currents for  $[FeCp^*_2]$  and **6** are approximately equal relative to the baseline, and the current associated with  $E_{pa}$  increases in magnitude more than  $E_{pc}$  as the scan rate is increased. This behaviour is typically an indication of electrochemical irreversibility arising from slow electron transfer due to a significant structural change that accompanies the redox process. In this case, this is likely due to loss and perhaps re-association of the coordinated potassium cation in **6**.

**Table 3.6.1** Peak-to-peak separations ( $\Delta E_p$ ) for the calibrant,  $[\text{FeCp}^*_2]^{+/0}$ , and complex **6** with respect to increasing scan rates.

Scan Rate (mV/s)	$\Delta E_p([\text{FeCp}^*_2])$ (mV)	$\Delta E_p(\mathbf{6})$ (mV)
50	81	232
100	91	287
200	101	342
500	125	421
1000	147	488

For a quasi-reversible wave (one which is chemically reversible but electrochemically irreversible),  $E_{1/2}$  will not be exactly the average of  $E_{pa}$  and  $E_{pc}$  values. However, this can be used as an approximation, and for **6**, a value of  $E_{1/2} \approx 0.64$  V versus  $[\text{FeCp}_2]^{+/0}$  was obtained. This  $E_{1/2}$  value is similar to that of  $\text{Ag}^+$  in  $\text{CH}_2\text{Cl}_2$  (0.65 V versus  $[\text{FeCp}_2]^{+/0}$ ).<sup>99</sup> These findings are consistent with the observed inability of  $\text{CuCl}$  to oxidize **6**, given that  $\text{Cu(I)}$  is less oxidizing than  $\text{Ag(I)}$ .<sup>100</sup>

For the sake of comparison,  $[\text{V}(\text{O}^t\text{Bu})_4]$  (**2**) was similarly analyzed by CV. This CV shows a qualitatively reversible wave for reduction of **2**, albeit with a somewhat larger peak-to-peak separation than that for  $[\text{FeCp}^*_2]$ ; **Table 3.6.2**. The  $E_{1/2}$  for reduction of **2** was determined to be  $-2.13$  V versus  $[\text{FeCp}_2]^{+/0}$ . The sharp contrast in the  $E_{1/2}$  values for complexes **2** and **6**, which differ by approximately 2.77 V, is attributed to the strong electron withdrawing capability of the fluorinated ligands, rendering the vanadium center in **6** far less electron rich than that in complex **2**.

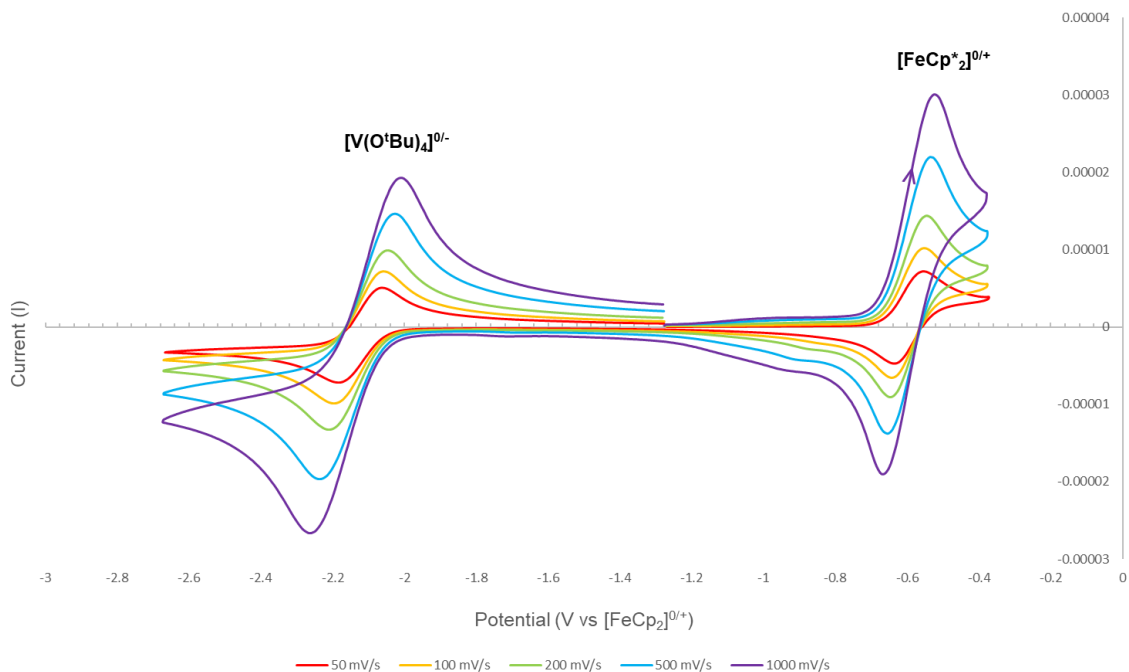


**Figure 3.6.3** Cyclic Voltammograms of  $[\text{V}(\text{O}^t\text{Bu})_4]$  (**2**) in a 0.1 M  $[\text{NBu}_4][\text{B}(\text{C}_6\text{F}_5)_4]$  solution in 1,2-difluorobenzene (DFB) using  $[\text{FeCp}^*_2]^{+/0}$  ( $E_{1/2} = -597$  mV) as a calibrant referenced to  $[\text{FeCp}_2]^{+/0}$  externally. Working and counter electrodes: Pt; reference electrode:  $\text{Ag}^+/\text{Ag}$ .

**Table 3.6.2** Peak-to-peak separations ( $\Delta E_p$ ) for the calibrant,  $[\text{FeCp}^*_2]^{+/0}$ , and complex **2** with respect to increasing scan rates

Scan Rate (mV/s)	$\Delta E_p([\text{FeCp}^*_2])$ (mV)	$\Delta E_p(\mathbf{2})$ (mV)
50	76	121
100	91	136
200	101	166
500	120	210
1000	147	253

To further analyze the reversibility of **2**, the Nicholson equation (Equation 4) was employed to determine if the anodic and cathodic peak currents of **2** were of comparable amplitude. Based on this calculation (presented in **Table 3.6.3**), the reduction of **2** is seemingly reversible.

**Table 3.6.3** Nicholson equation parameters calculated to determine the electrochemical reversibility of complex **2** using the 50 mV/s and 500 mV/s voltammograms

	50 mV/s	500 mV/s
$(i_{pr})_0$	$4.94 \times 10^{-6}$	$1.40 \times 10^{-5}$
$i_{pf}$	$7.06 \times 10^{-6}$	$1.46 \times 10^{-5}$
$i_\lambda$	$3.11 \times 10^{-6}$	$8.19 \times 10^{-6}$
$\frac{i_{pr}}{i_{pf}}$	1.00	1.02

As a final comparison,  $[\text{Cr}(\text{O}^t\text{Bu})_4]$  (**1**) was analyzed by CV. Reduction of **1** occurs at roughly  $-1.7$  V versus  $[\text{FeCp}_2]^{+/0}$ , indicating that **1** is more readily reduced than **2**. However, complex **1** also underwent oxidation at an  $E_{1/2}$  value of  $0.43$  V versus  $[\text{FeCp}_2]^{+/0}$ . The peak-to-peak separations ( $\Delta E_p$ , **Table 3.6.4**) for both oxidation and reduction of **1** are large relative to  $[\text{FeCp}^*_2]^{+/0}$  especially for the reduction peak, and the reason for this is unclear.

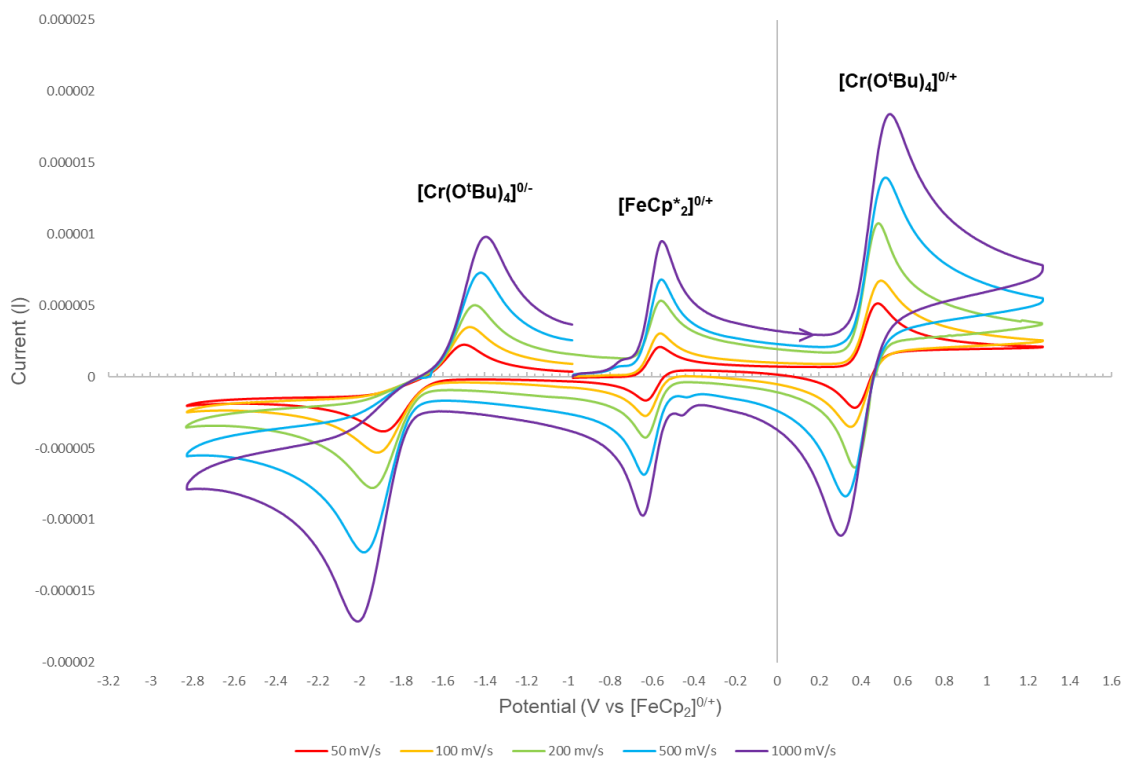


**Figure 3.6.4** Cyclic Voltammogram showing oxidation and reduction of  $[\text{Cr}(\text{O}^t\text{Bu})_4]$  (**1**) in a  $0.1$  M  $[\text{NBu}_4][\text{B}(\text{C}_6\text{F}_5)_4]$  solution in difluorobenzene (DFB) using  $[\text{FeCp}^*_2]^{+/0}$  ( $E_{1/2} = -597$  mV) as a calibrant referenced to  $[\text{FeCp}_2]^{+/0}$  externally. Working and counter electrodes: Pt; reference electrode:  $\text{Ag}^+/\text{Ag}$ .

**Table 3.6.4** Peak-to-peak separations ( $\Delta E_p$ ) for the calibrant,  $[\text{FeCp}^*_2]^{+/0}$ , and complex **1** with respect to increasing scan rates

Scan Rate (mV/s)	$\Delta E_p$ for $[\text{FeCp}^*_2]^{0/+}$ (mV)	$\Delta E_p$ for <b>1</b> <sup>0/+</sup> (mV)	$\Delta E_p$ for <b>1</b> <sup>0/-</sup> (mV)
50	71	116	390
100	72	141	445
200	71	106	495
500	80	195	559
1000	93	236	610

## 4 Conclusions and Future Work

[Cr(O<sup>t</sup>Bu)<sub>4</sub>] (**1**) and [V(O<sup>t</sup>Bu)<sub>4</sub>] (**2**) were prepared according to literature procedures and were isolated in 66% and 47% yield, respectively. Complex **1** undergoes sublimation at 25 °C (10 mTorr) and undergoes decomposition when heated to 110 °C for 24 hours. The thermal decomposition products were identified as isobutylene and *tert*-butanol by <sup>1</sup>H NMR spectroscopy, and the insoluble powder was determined to be amorphous by PXRD. This limits the range of bubbler temperatures for precursor delivery to be between 65 and around 100 °C. Complex **2** undergoes distillation at 25 °C (10 mTorr) and undergoes decomposition when heated to 75 °C in the presence of light for 24 hours. The decomposition products were identified as isobutylene and *tert*-butanol by <sup>1</sup>H NMR spectroscopy, and the insoluble powder was determined to be amorphous by PXRD. However, in the absence of light, complex **2** undergoes decomposition at 100 °C when heated for one week. Thus, the range of bubbler temperatures for complex **2** was determined to be between 65 and about 90 °C.

These complexes were expected to undergo reduction to elemental metal through the reaction with hydrosilanes and hydroboranes. The reactions of **1** and **2** with HBpin proceeded at room temperature (after 24 hours and after 30 seconds, respectively) which resulted in the formation of insoluble material and <sup>t</sup>BuO-Bpin as by-products. The insoluble material was found to be amorphous by PXRD for both reactions (**1** with HBpin, and **2** with HBpin). Repeating these reactions using hexamethylbenzene as an internal <sup>1</sup>H NMR standard established that in both cases, all four *tert*-butoxide ligands are removed from the metal, in the form of <sup>t</sup>BuO-Bpin. This analysis, in conjunction with the observation of gas evolution (presumably H<sub>2</sub>) suggests that the observed reactivity

proceeds to form elemental metal in accordance with the hypothesized reaction pathway proposed in **Scheme 2.1.1**. This combination of precursors and co-reagents suggests the possibility of developing an ALD procedure. ALD of chromium and vanadium thin films utilizing complexes **1** and **2**, respectively, in conjunction with HBpin as a co-reagent, should be attempted. Solution state reactivity studies utilizing PhSiH<sub>3</sub> may also proceed as anticipated in **Scheme 2.1.1**, but required higher temperatures, making PhSiH<sub>3</sub> less suitable (than HBpin) as an ALD co-reagent. In contrast, decamethylsilicocene (**3**), and 1,4-bis(trimethylsilyl)-2-methyl-2,5-cyclohexadiene (**4**), showed no reactivity up to 90 °C.

In an attempt to increase the thermal stability of **1** and **2**, the synthesis of chromium and vanadium complexes containing perfluoro-*tert*-butoxide (pftb) ligands was explored. The chromium complex [CrCl(pftb)<sub>2</sub>(THF)<sub>3</sub>] (**5**) was accessed via the reaction of [CrCl<sub>3</sub>(THF)<sub>3</sub>] and Kpftb, and an X-ray crystal structure was obtained. However, this complex could not be isolated in pure form. Similar reactivity between [VCl<sub>3</sub>(THF)<sub>3</sub>] and Kpftb was explored, and K[V(pftb)<sub>4</sub>] (**6**) was isolated. Furthermore, the toluene solvate of **6**, **6**(toluene), was crystallographically characterized. Complex **6** sublimed at 75-85 °C (10 mTorr) and exhibited some decomposition after heating at 130 °C for 24 hours. No reactivity was observed by <sup>19</sup>F NMR spectroscopy in solution reactions between **6** and HBpin even after heating the solution to 100 °C for 24 hours. Reactivity was observed by <sup>19</sup>F NMR spectroscopy between **6** and PhSiH<sub>3</sub> when the solution was heated to 90 °C for 24 hours. However, no precipitation resulted from this reaction, and no gas evolution was observed, indicating no reduction to elemental vanadium. In order to assess the feasibility of accessing [V(pftb)<sub>4</sub>], cyclic voltammetry was utilized to determine the redox potential

for oxidation of **6**. In a 1,2-difluorobenzene solution, the  $E_{1/2}$  value of **6** was determined to be approximately 0.64 V versus  $[\text{FeCp}_2]^{+/0}$ . The cyclic voltammograms obtained for complex **6** seem to indicate that the  $\mathbf{6}^{0/+}$  redox couple is associated with a structural change, which results in slow electron transfer. This could be due to the loss of the potassium cation from the structure. In order to validate this claim, a cation exchange reaction between complex **6** and tetrabutylammonium chloride could be conducted such that the structural reconfiguration of complex **6** as it undergoes oxidation and reduction would be limited. If a symmetrical wave is observed, then it would indicate the validity of the proposed hypothesis.

As a comparative analysis,  $[\text{V}(\text{O}^t\text{Bu})_4]$  (**2**) was analyzed by cyclic voltammetry; this yielded a qualitatively reversible reduction process and the  $E_{1/2}$  value for  $\mathbf{2}^{0/-}$  was found to be -2.13 V versus  $[\text{FeCp}_2]^{+/0}$ . Analyzing the chromium analogue,  $[\text{Cr}(\text{O}^t\text{Bu})_4]$  (**1**), significantly larger peak-to-peak separations were observed, and the  $E_{1/2}$  for reduction of **1** was calculated to be -1.7 V versus  $[\text{FeCp}_2]^{+/0}$ . Oxidation of **1** was also observed with an  $E_{1/2}$  value of approximately 0.43 V versus  $[\text{FeCp}_2]^{+/0}$ .

## 5 Experimental

### 5.1 General Experimental Conditions

All moisture and air sensitive operations were performed either in a purified and dry argon atmosphere in a glovebox or using standard Schlenk line techniques. Purification of the Schlenk line argon supply was achieved by passing the argon stream through an Oxisorb-W scrubber. NMR spectroscopy was performed using Bruker AV-200, Bruker AV-500, and Bruker AV-600 spectrometers.  $^1\text{H}$  NMR spectra were collected at 298 K and were referenced to  $\text{C}_6\text{D}_6$  ( $\delta$  7.16 ppm) or  $d_8$ -THF ( $\delta$  1.72 and 3.58 ppm). All  $^{13}\text{C}$ ,  $^{11}\text{B}$ , and  $^{29}\text{Si}$  NMR spectra were indirectly referenced with respect to the preceding  $^1\text{H}$  NMR spectrum collected in accordance with the procedure utilized by Iowa State University.<sup>101</sup> The  $^{19}\text{F}$  NMR spectra collected for Chapter 3 were externally referenced to a sample of  $\text{CFCl}_3$  ( $\delta$  0 ppm). All deuterated solvents used were purchased from ACP chemicals and were dried over sodium/benzophenone and distilled. Combustion elemental analyses were performed by the University of Calgary.

Single crystal X-ray analyses were conducted on crystals coated with Paratone oil and mounted on a SMART APEX II diffractometer with a 3 kW sealed Mo generator equipped with a SMART6000 CCD detector at the McMaster Analytical X-ray Diffraction Facility. The collected data sets were processed using XPREP and were solved by SHELXS-97 direct methods and structure refinement was performed using Olex2. All non-hydrogen atoms were solved anisotropically. Powder X-ray diffraction analyses were conducted on a Bruker D8 Advance powder diffractometer with  $\text{Cu K}\alpha$  radiation ( $\lambda = 0.154$  nm). Diffraction patterns collected were processed and analyzed using Diffrac.eva.

All solvents utilized (THF, diethyl ether, toluene, hexanes, pentane, and benzene) were purchased from Sigma Aldrich. THF, diethyl ether, toluene, hexanes, and pentane were dried over sodium/benzophenone and distilled prior to use. Benzene was dried over molecular sieves (4 Å). Acetic acid, ethyl acetate, trifluoroacetic acid, DCM, and methanol were purchased from Sigma Aldrich and were used without further purification

Commercial reagents such as  $[\text{CrCl}_3(\text{THF})_3]$ ,  $[\text{VCl}_3(\text{THF})_3]$ , KH, CuCl, KO<sup>t</sup>Bu, HCp\*, HSiCl<sub>3</sub>, Hpftb, HBpin, and PhSiH<sub>3</sub> were purchased from Sigma Aldrich. HSiCl<sub>3</sub>, Hpftb, HBpin, and PhSiH<sub>3</sub> were degassed through the freeze-pump-thaw method and distilled prior to use.

## 5.2 Synthetic Procedures

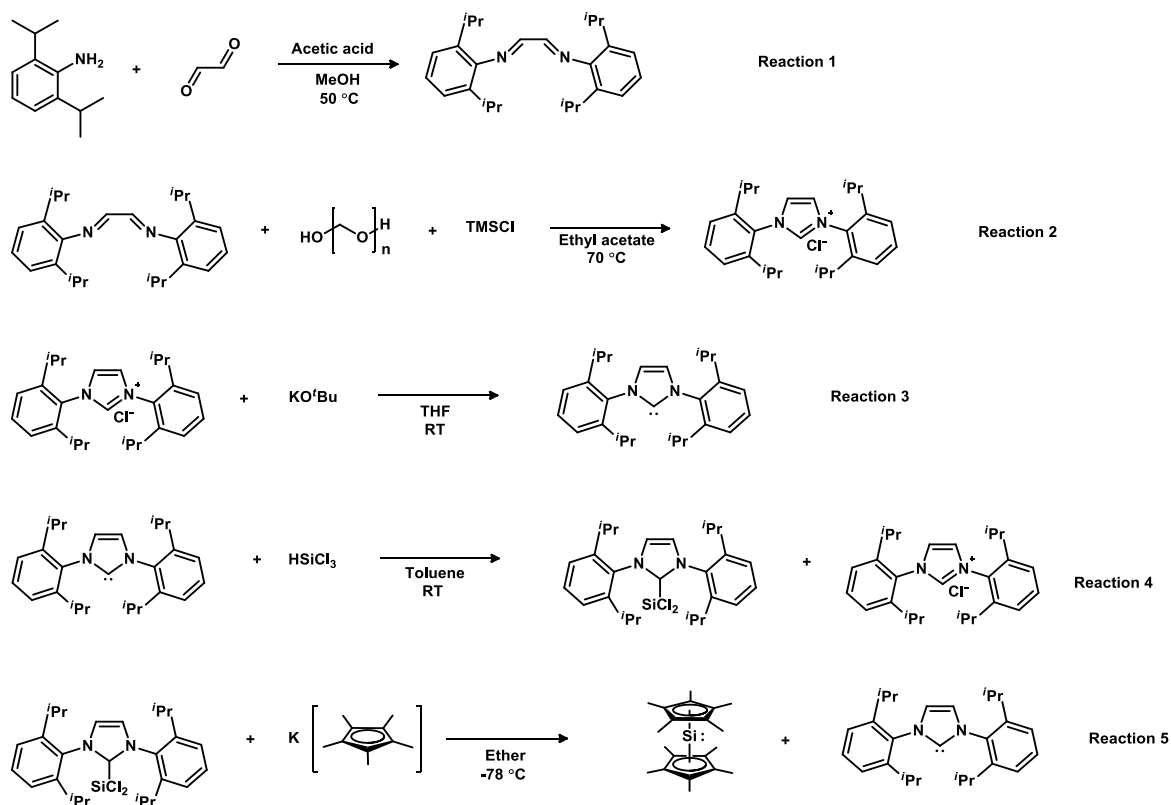
$[\text{Cr}(\text{O}^t\text{Bu})_4]$  (1) This compound was prepared in accordance with the literature procedure with slight modifications.<sup>58</sup> To a 100 mL round bottom flask, 1.000 g of  $[\text{CrCl}_3(\text{THF})_3]$ , 1.1980 g of KO<sup>t</sup>Bu, and 0.3287 g of CuCl was added in a glovebox atmosphere. 10 mL of THF was added to the mixture of solids. The solution was then allowed to stir at room temperature for 24 hours resulting in a deep blue solution with suspended brown copper solid. The volatiles were then stripped *in vacuo* while cooling with an ice bath. This was done to reduce the volatilization of the product. The dark brown slurry was then subjected to sublimation to isolate the dark blue solid as the desired product in 66% yield (0.6101 g) (25 °C, 10 mTorr). <sup>1</sup>H NMR (C<sub>6</sub>D<sub>6</sub>, 600 MHz, 298 K): δ 3.02 ppm (broad s, C(CH<sub>3</sub>)<sub>3</sub>)

$[\text{V}(\text{O}^t\text{Bu})_4]$  (2) This compound was prepared in accordance with the literature procedure with slight modifications.<sup>45</sup> In a glovebox atmosphere, to a 50 mL round bottom flask

0.1000 g of  $[\text{VCl}_3(\text{THF})_3]$  was dissolved in 3 mL of THF resulting in a pink solution. 0.1201 g of  $\text{KO}^t\text{Bu}$ , and 0.0265 g of  $\text{CuCl}$  was added to this solution and resulted in the formation of a deep blue solution. The solution was then allowed to stir at room temperature for 24 hours which resulted in the formation of a seemingly black mixture. The volatiles were then stripped *in vacuo* while cooling with an ice bath. This was done to reduce the volatilization of the product. The dark brown slurry was then subjected to distillation (25-30 °C, 10 mTorr) to isolate the vibrant blue liquid as the desired product in 47% yield (43.5 mg).  $^1\text{H NMR}$  ( $\text{C}_6\text{D}_6$ , 600 MHz, 298 K):  $\delta$  3.07 ppm (broad s,  $\text{C}(\text{CH}_3)_3$ )

$\text{SiCp}_2^*$  (3) Synthesis of the target compound was adapted from literature sources.<sup>102-104</sup>

For the sake of this discussion, 1,3-bis(2,6-diisopropylphenyl)imidazolium chloride will be abbreviated as  $[\text{H}(\text{Idipp})]\text{Cl}$  and the corresponding carbene, 1,3-bis(2,6-diisopropylphenyl)imidazole-2-ylidene, as  $\text{Idipp}$ . Synthesis of  $[\text{H}(\text{Idipp})]\text{Cl}$  from starting material is illustrated in **Scheme 5.2.1**. Reactions 1 and 2 were carried out in air, whereas reactions 3-5 were conducted under argon.



**Scheme 5.2.1** Reactions involved in the synthesis of decamethylsilicocene (**3**)

Reaction 1: A solution containing 39.4 g of 2,6-diisopropylaniline and 3 mL of acetic acid in roughly 250 mL of methanol was added to a solution containing 14.6 g of glyoxal in roughly 250 mL of methanol in a 1 L round bottom flask. The reaction was stirred for 15 minutes at 50 °C. The oil bath was then removed, and the reaction was allowed to stir at room temperature for 24 hours. A yellow precipitate formed and was collected by filtration and washed with cold methanol. The solid was then dried *in vacuo* and collected in 56% yield (23.352 g).

Reaction 2: A solution containing 23.352 g of the product from Reaction 1 and 1.916 g of paraformaldehyde was prepared in roughly 250 mL of ethyl acetate. A separate solution of 8.12 mL of trimethylsilyl chloride in 30 mL of ethyl acetate was prepared in a two-

neck round bottom flask connected to a reflux condenser and heated to 70 °C. The solution containing paraformaldehyde and the product from Reaction 1 was added dropwise over the course of 20 minutes to the two-neck round bottom flask containing the solution of trimethylsilyl chloride in ethyl acetate. The reaction was allowed to stir at 70 °C for two hours and was cooled to 0 °C for 15 minutes. A pale grey precipitate was collected by filtration, washed with ethyl acetate two more times, and dried *in vacuo*. The collected material contained [H(Idipp)]Cl with two equivalents of ethyl acetate trapped in the lattice structure. To remove the ethyl acetate, the fine grey powder was dissolved in minimal warm DCM and was precipitated out with hexanes. The [H(Idipp)]Cl was then isolated by filtration as a fine white powder and dried *in vacuo*. The product of Reaction 2 was isolated in 69% yield (18.258 g).

Reaction 3: In a glovebox, a solution containing 5.855 g of [H(Idipp)]Cl (the product of Reaction 2) and 1.7002 g of KO<sup>t</sup>Bu was prepared in 20 mL of THF in a 100 mL round bottom flask. The solution was allowed to stir for 3 hours at room temperature which afforded a white precipitate. This precipitate was removed by filtration and was washed with three 10 mL portions of THF. The filtrates were combined and dried *in vacuo* to afford an off-white solid in 93% yield (4.9533 g).

Reaction 4: Under inert conditions, a solution containing 4.8224 g of Idipp (the product of Reaction 3) in toluene was prepared. To this, 0.63 mL of trichlorosilane was introduced. The reaction was left to stir for 24 hours at room temperature. The [H(Idipp)]Cl by product precipitated out of solution and was removed by filtration. The toluene filtrates were combined, and the solvent was removed *in vacuo* to afford a pale yellow solid. The pale yellow solid was then washed with copious amounts of hexane.

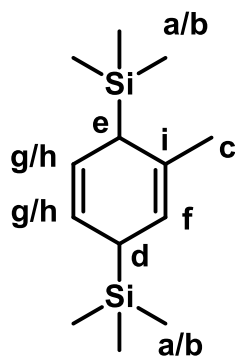
The yellow solid was then dried *in vacuo*. A small impurity exists that seemingly can be removed with more hexane washings, but these washings dissolved significant amounts of the product. With this minor impurity, 1.1450 g of the pale yellow solid, (Idipp)SiCl<sub>2</sub>, was collected in 19% yield.

Reaction 5: Proceeding with this impurity, the reagent was used without further purification. Under inert conditions, in a round bottom flask, 1.5707 g of (Idipp)SiCl<sub>2</sub> was combined with 1.1232 g of KCp\*. The flask was then cooled to -78 °C and diethyl ether was introduced by vacuum distillation which resulted in the formation of a beige solution. The reaction was allowed to stir at -78 °C for 1 hour. The reaction was then allowed to warm up to room temperature and stirred for an additional hour. The volatiles were removed *in vacuo* to afford a beige solid. This solid mixture was stirred in cold hexanes and the resulting suspension was subjected to filtration. The filtered material was washed three times with cold hexanes. The Idipp generated in Reaction 5 was slightly soluble in hexane, so, minimal amounts of solvent were used. The hexane filtrates were then combined and dried *in vacuo*. An off white solid was collected and was further purified by sublimation (10 mTorr, 90 °C). Decamethylsilicocene (**3**) was collected from the cold finger as a white solid in 42% yield (0.9555 g). <sup>1</sup>H NMR (C<sub>6</sub>D<sub>6</sub>, 600 MHz, 298 K): δ 1.90 ppm (s, CH<sub>3</sub>). <sup>13</sup>C NMR (C<sub>6</sub>D<sub>6</sub>, 151 MHz, 298 K): δ 10.69 ppm (C(CH<sub>3</sub>)), 119.46 ppm (C(CH<sub>3</sub>)).

#### 1,4-bis(trimethylsilyl)-2-methyl-2,5-cyclohexadiene (4)

This synthesis was adapted from a literature source.<sup>105</sup> In a glovebox, a suspension of 0.548 g of granular lithium in 10 mL of THF and excess toluene (approximately 3 mL) was prepared. This mixture was then cooled to 0 °C. To this suspension, 6.67 mL of

trimethylsilyl chloride was added dropwise. The solution was allowed to stir for 5 hours at 0 °C. Approximately 100 mL of pentane was added to the reaction to precipitate out the generated LiCl. The suspension was centrifuged and decanted. The volatiles of the supernatant were removed *in vacuo* and a thick pale-yellow liquid was collected as the product in 46% yield (2.8624 g). **<sup>1</sup>H NMR** (C<sub>6</sub>D<sub>6</sub>, 600 MHz, 298 K): δ 0.06 and 0.11 ppm (2 × s, 18H, Si(CH<sub>3</sub>)<sub>3</sub>), 1.65 ppm (s, 3H CCH<sub>3</sub>), 2.09 and 2.22 ppm (2 × m, 1H, 1H, SiCH), 5.28 ppm (m, CH ortho to CCH<sub>3</sub>), 5.53-5.63 ppm (2 × m, 2H, CH para and CH meta to CCH<sub>3</sub>). **<sup>13</sup>C NMR** (C<sub>6</sub>D<sub>6</sub>, 151 MHz, 298 K): -1.51 and -3.11 ppm (a/b), 25.01 ppm (c), 31.32 ppm (d), 36.23 ppm (e), 118.12 ppm (f), 122.83 and 126.29 ppm (g/h), 132.83 ppm (i).



[CrCl(pftb)<sub>2</sub>(THF)<sub>3</sub>] (**5**) In a glovebox atmosphere, to a thick-walled Schlenk flask, 250 mg (0.67 mmol) of [CrCl<sub>3</sub>(THF)<sub>3</sub>] was dissolved in 2 mL of THF. To this purple solution, 732 mg (2.67 mmol) of Kpftb was added. The solution was allowed to stir for 24 hours at 60 °C during which time the purple solution changed to a deep blue solution. The insoluble material was filtered and washed with three 10 mL portions of THF. The filtrates were combined and dried *in vacuo* to yield a blue solid. The isolated material was

dissolved in a minimal amount of warm toluene and was cooled to  $-30\text{ }^{\circ}\text{C}$ , which yielded a blue precipitate. The supernatant was decanted, and the crystallization procedure was repeated two more times. The crystallized material was dissolved in THF, transferred to a round bottom flask, and dried *in vacuo* for 24 hours to yield 439 mg of a blue solid containing a mixture of two products. The major product remains uncharacterized. However, the minor product was crystallized by dissolving the isolated blue solid in warm toluene and cooling to  $-30\text{ }^{\circ}\text{C}$  to afford large purple blocks which were crystallographically characterized to be  $[\text{CrCl}(\text{pftb})_2(\text{THF})_3]$  (**5**).  $^{19}\text{F}$  NMR of  $[\text{CrCl}(\text{pftb})_2(\text{THF})_3]$  (THF externally referenced to  $\text{CFCl}_3$ , 188 MHz, 298 K):  $\delta -37$  ppm (broad s,  $\text{C}(\text{CF}_3)_3$ ).  $^{19}\text{F}$  NMR of the major species (THF externally referenced to  $\text{CFCl}_3$ , 188 MHz, 298 K):  $\delta 20$  ppm (broad s,  $\text{C}(\text{CF}_3)_3$ ).

$\text{K}[\text{V}(\text{pftb})_4]$  (**6**) In a glovebox, a solution of 250 mg (0.67 mmol) of  $[\text{VCl}_3(\text{THF})_3]$  was prepared in 5 mL of THF in a 20 mL round bottom flask, which afforded a vibrant pink solution. To this solution, 734 mg (2.68 mmol) of  $\text{Kpftb}$  was added, which resulted in the immediate conversion of the pink solution to a deep blue solution. The solution mixture was allowed to stir at room temperature for 1 hour. The insoluble material was filtered and washed with three 10 mL portions of THF. The filtrates were combined and dried *in vacuo* to yield a purple solid. The isolated material was dissolved in a minimal amount of warm toluene and cooled to  $-30\text{ }^{\circ}\text{C}$ , which yielded large purple crystals of **6**(toluene). The supernatant was decanted, and the crystallization procedure was repeated two more times. The crystallized material was washed with hexanes three times and dried *in vacuo* for 24 hours in a vial carrier to yield 404.2 mg of a fine purple solid in 59% yield.  $^{19}\text{F}$

**NMR** (THF externally referenced to  $\text{CFCl}_3$ , 188 MHz, 298 K):  $\delta$  -40 ppm (broad s,  $\text{C}(\text{CF}_3)_3$ ). Elemental analysis found (calculated): C, 18.33% (18.65%); H, 0.07% (0%).

### 5.3 Solution State Reactions

$[\text{Cr}(\text{O}^t\text{Bu})_4]$  (**1**) with HBpin In a J-Young tube, 8.5 mg of **1** was reacted with 17.6 mg of HBpin (1:5.6 eq) in  $\text{C}_6\text{D}_6$ . The evolution of a gas (presumably hydrogen gas) was noted roughly 1 hour after addition. The solution was left to react for 24 hours at room temperature which resulted in the transformation of the solution to a very thick black suspension. In order to record NMR spectra of the reaction products, the suspension was centrifuged, and the clear supernatant was decanted.  $^t\text{BuO-Bpin}$  was identified as the reaction by-product.  **$^1\text{H}$  NMR** of  $^t\text{BuO-Bpin}$  ( $\text{C}_6\text{D}_6$ , 600 MHz, 298 K):  $\delta$  1.38 ppm (s, 9H,  $\text{C}(\text{CH}_3)_3$ ), 1.06 ppm (s, 12H,  $\text{C}(\text{CH}_3)_2$ )

$[\text{Cr}(\text{O}^t\text{Bu})_4]$  (**1**) with  $\text{PhSiH}_3$  In a J-Young tube, 9.7 mg of **1** was reacted with 22.2 mg of  $\text{PhSiH}_3$  (1:7.3 eq) in  $\text{C}_6\text{D}_6$ . No reactivity was observed at room temperature when left for 24 hours. The reaction was heated for 60 °C for three days which resulted in the formation of a black suspension.

$[\text{Cr}(\text{O}^t\text{Bu})_4]$  (**1**) with TFA/HBpin in the presence of  $\text{C}_6\text{Me}_6$  A solution was prepared using 20.0 mg of **1** and 9.4 mg of hexamethylbenzene (1.0:1.0 eq) in  $\text{C}_6\text{D}_6$ . The solution was then divided into two NMR tubes. An excess of TFA was added to one NMR tube and the solution colour changed immediately from deep blue to a pale blue solution. The reaction was left to react for 24 hours at room temperature. The other portion was reacted with an excess of HBpin and was left to react for 24 hours at room temperature. After this period of time, NMR spectra were collected.

[V(O<sup>t</sup>Bu)<sub>4</sub>] (2) with HBpin In a J-Young tube, 10.0 mg of **2** was combined with 18.6 mg of HBpin (1:5.0 eq) in C<sub>6</sub>D<sub>6</sub>. Upon the addition of HBpin, the solution changed colour to a teal green within a few seconds. The evolution of gas bubbles was visually observed and within an hour at room temperature, the mixture adopted a deep black colour. A <sup>1</sup>H NMR spectrum of the reaction solution was acquired after one hour of reaction time and hydrogen gas and <sup>t</sup>BuO-Bpin were identified. <sup>1</sup>H NMR of <sup>t</sup>BuO-Bpin (with the presence of H<sub>2</sub>) δ 1.38 ppm (s, 9H, C(CH<sub>3</sub>)<sub>3</sub>), 1.06 ppm (s, 12H, C(CH<sub>3</sub>)<sub>2</sub>), 4.47 ppm (s, H<sub>2</sub>).

[V(O<sup>t</sup>Bu)<sub>4</sub>] (2) with PhSiH<sub>3</sub> In a J-Young tube, 10.0 mg of **2** was reacted with 15.8 mg of PhSiH<sub>3</sub> (1:5.0 eq) in C<sub>6</sub>D<sub>6</sub>. No reactivity was observed initially when the solution was left at room temperature. Reactivity was observed when the sample was heated to 70 °C overnight. The reaction solution was monitored over time, and it was found that the starting material, **2**, was still present by NMR after two days of heating. The reaction solution was monitored over the course of five days at 70 °C until the starting material (**2**) was fully consumed to afford a black mixture. The major product of this reaction was identified as PhSiH(O<sup>t</sup>Bu)<sub>2</sub> and hydrogen gas was detected by <sup>1</sup>H NMR spectroscopy. <sup>1</sup>H NMR (C<sub>6</sub>D<sub>6</sub>, 600 MHz, 298 K): δ 1.32 ppm (s, 18H, C(CH<sub>3</sub>)<sub>3</sub>), 5.47 ppm (s, 1H, SiH), 7.83 ppm (m, 2H, CH meta to Si), 4.47 ppm (s, H<sub>2</sub>).

[V(O<sup>t</sup>Bu)<sub>4</sub>] (2) with HBpin in the presence of C<sub>6</sub>Me<sub>6</sub> A solution was prepared using 10.0 mg of **1** and 4.7 mg of hexamethylbenzene (1.0:1.0 eq) in C<sub>6</sub>D<sub>6</sub>. This solution was then reacted with 18.6 mg of HBpin (1:5.0 eq) for 24 hours at room temperature. After this period of time, NMR spectra were collected.

**Table A** Crystal and Structure refinement data for [CrCl(pftb)<sub>2</sub>(THF)<sub>3</sub>] (**5**)

Identification code	monoclinicAKS1_a
Empirical formula	C <sub>20</sub> H <sub>24</sub> ClCrF <sub>18</sub> O <sub>5</sub>
Formula weight	773.84
Temperature/K	296.15
Crystal system	monoclinic
Space group	P2 <sub>1</sub> /c
a/Å	19.822(4)
b/Å	9.564(2)
c/Å	15.9097(17)
α/°	90
β/°	112.068(17)
γ/°	90
Volume/Å <sup>3</sup>	2795.3(9)
Z	4
ρ <sub>calc</sub> /cm <sup>3</sup>	1.839
μ/mm <sup>-1</sup>	0.657
F(000)	1548.0
Crystal size/mm <sup>3</sup>	0.5 × 0.45 × 0.3
Radiation	MoKα (λ = 0.71073)
2Θ range for data collection/°	4.802 to 59.118
Index ranges	-27 ≤ h ≤ 20, -13 ≤ k ≤ 13, -22 ≤ l ≤ 21
Reflections collected	27440
Independent reflections	7681 [R <sub>int</sub> = 0.0251, R <sub>sigma</sub> = 0.0391]
Data/restraints/parameters	7681/0/406
Goodness-of-fit on F <sup>2</sup>	1.037
Final R indexes [I ≥ 2σ (I)]	R <sub>1</sub> = 0.0312, wR <sub>2</sub> = 0.0741
Final R indexes [all data]	R <sub>1</sub> = 0.0420, wR <sub>2</sub> = 0.0782
Largest diff. peak/hole / e Å <sup>-3</sup>	0.49/-0.64

**Table B** Crystal and Structure refinement data for  $[(\eta^3\text{-Tol})\text{K}(\mu\text{-pftb})_2\text{V}(\text{pftb})_2]\{\mathbf{6}(\text{toluene})\}$

Identification code	AKS2_0m
Empirical formula	$\text{C}_{23}\text{H}_8\text{F}_{36.03}\text{KO}_4\text{V}$
Formula weight	1122.81
Temperature/K	296.15
Crystal system	monoclinic
Space group	$\text{P}2_1/\text{c}$
$a/\text{\AA}$	16.253(10)
$b/\text{\AA}$	10.540(5)
$c/\text{\AA}$	21.510(14)
$\alpha/^\circ$	90
$\beta/^\circ$	107.89(3)
$\gamma/^\circ$	90
Volume/ $\text{\AA}^3$	3506(4)
Z	4
$\rho_{\text{calc}}/\text{cm}^3$	2.127
$\mu/\text{mm}^{-1}$	0.628
F(000)	2177.0
Crystal size/ $\text{mm}^3$	$0.4 \times 0.2 \times 0.1$
Radiation	$\text{MoK}\alpha$ ( $\lambda = 0.71073$ )
$2\Theta$ range for data collection/ $^\circ$	3.98 to 52.74
Index ranges	$-20 \leq h \leq 20, -13 \leq k \leq 13, -25 \leq l \leq 26$
Reflections collected	28773
Independent reflections	7171 [ $R_{\text{int}} = 0.1116, R_{\text{sigma}} = 0.1049$ ]
Data/restraints/parameters	7171/0/588
Goodness-of-fit on $F^2$	1.028
Final R indexes [ $I \geq 2\sigma(I)$ ]	$R_1 = 0.0819, wR_2 = 0.2060$
Final R indexes [all data]	$R_1 = 0.1472, wR_2 = 0.2382$
Largest diff. peak/hole / $e \text{\AA}^{-3}$	1.04/-0.76

## 6 References

- (1) Velmre, E. Thomas Johann Seebeck (1770-1831). *Proc. Est. Acad. Sci. Eng.* **2007**, *13* (4), 276–282.
- (2) November 17 - December 23, 1947: Invention of the First Transistor <https://www.aps.org/publications/apsnews/200011/history.cfm>.
- (3) Moore, G. E. Cramming More Components onto Integrated Circuits. *Proc. IEEE* **1998**, *86* (1), 82–85. <https://doi.org/10.1109/JPROC.1998.658762>.
- (4) Fortunato, E.; Barquinha, P.; Martins, R. Oxide Semiconductor Thin-Film Transistors: A Review of Recent Advances. *Adv. Mater.* **2012**, *24* (22), 2945–2986. <https://doi.org/10.1002/adma.201103228>.
- (5) Shen, C.; Yin, Z.; Collins, F.; Pinna, N. Atomic Layer Deposition of Metal Oxides and Chalcogenides for High Performance Transistors. *Adv. Sci.* **2022**, *9* (23), 1–37. <https://doi.org/10.1002/advs.202104599>.
- (6) Prentki, R. J.; Harb, M.; Zhou, C.; Philippopoulos, P.; Beaudoin, F.; Michaud-Rioux, V.; Guo, H. Tunneling Leakage in Ultrashort-Channel MOSFETs—From Atomistics to Continuum Modeling. *Solid. State. Electron.* **2022**, *197* (August). <https://doi.org/10.1016/j.sse.2022.108438>.
- (7) Introducing the world’s first 2 nm node chip <https://research.ibm.com/blog/2-nm-chip> (accessed Nov 15, 2022).
- (8) Pan, D.; Li, T.; Chien Jen, T.; Yuan, C. Numerical Modeling of Carrier Gas Flow in Atomic Layer Deposition Vacuum Reactor: A Comparative Study of Lattice Boltzmann Models. *J. Vac. Sci. Technol. A Vacuum, Surfaces, Film.* **2014**, *32* (1), 01A110. <https://doi.org/10.1116/1.4833561>.
- (9) Leskelä, M.; Ritala, M. Atomic Layer Deposition (ALD): From Precursors to Thin Film Structures. *Thin Solid Films* **2002**, *409* (1), 138–146. [https://doi.org/10.1016/S0040-6090\(02\)00117-7](https://doi.org/10.1016/S0040-6090(02)00117-7).
- (10) George, S. M. Atomic Layer Deposition: An Overview. *Chem. Rev.* **2010**, *110* (1), 111–131. <https://doi.org/10.1021/cr900056b>.
- (11) Emslie, D. J. H.; Chadha, P.; Price, J. S. Metal ALD and Pulsed CVD: Fundamental Reactions and Links with Solution Chemistry. *Coord. Chem. Rev.* **2013**, *257* (23–24), 3282–3296. <https://doi.org/10.1016/j.ccr.2013.07.010>.
- (12) Puurunen, R. L. Surface Chemistry of Atomic Layer Deposition: A Case Study for the Trimethylaluminum/Water Process. *J. Appl. Phys.* **2005**, *97* (12). <https://doi.org/10.1063/1.1940727>.
- (13) Klesko, J. P.; Kerrigan, M. M.; Winter, C. H. Low Temperature Thermal Atomic Layer Deposition of Cobalt Metal Films. *Chem. Mater.* **2016**, 8–11. <https://doi.org/10.1021/acs.chemmater.5b03504>.

- (14) Klesko, J. P.; Thrush, C. M.; Winter, C. H. Thermal Atomic Layer Deposition of Titanium Films Using Titanium Tetrachloride and 2-Methyl-1,4-Bis(Trimethylsilyl)-2,5-Cyclohexadiene or 1,4-Bis(Trimethylsilyl)-1,4-Dihydropyrazine. *Chem. Mater.* **2015**, 25–28. <https://doi.org/10.1021/acs.chemmater.5b01707>.
- (15) Mäkelä, M.; Hatanpää, T.; Mizohata, K.; Räisänen, J.; Ritala, M.; Leskelä, M. Thermal Atomic Layer Deposition of Continuous and Highly Conducting Gold Thin Films. *Chem. Mater.* **2017**, 29 (14), 6130–6136. <https://doi.org/10.1021/acs.chemmater.7b02167>.
- (16) Yamada, A.; Sang, B.; Konagai, M. Atomic Layer Deposition of ZnO Transparent Conducting Oxides. *Appl. Surf. Sci.* **1997**, 112, 216–222. [https://doi.org/10.1016/S0169-4332\(96\)01022-7](https://doi.org/10.1016/S0169-4332(96)01022-7).
- (17) Yousfi, E. B.; Fouache, J.; Lincot, D. Study of Atomic Layer Epitaxy of Zinc Oxide by In-Situ Quartz Crystal Microgravimetry. *Appl. Surf. Sci.* **2000**, 153 (4), 223–234. [https://doi.org/10.1016/S0169-4332\(99\)00330-X](https://doi.org/10.1016/S0169-4332(99)00330-X).
- (18) Ritala, M.; Leskelä, M.; Johansson, L. S.; Niinistö, L. Atomic Force Microscopy Study of Titanium Dioxide Thin Films Grown by Atomic Layer Epitaxy. *Thin Solid Films* **1993**, 228 (1–2), 32–35. [https://doi.org/10.1016/0040-6090\(93\)90557-6](https://doi.org/10.1016/0040-6090(93)90557-6).
- (19) Mui, C.; Musgrave, C. B. Atomic Layer Deposition of HfO<sub>2</sub> Using Alkoxides as Precursors. *J. Phys. Chem. B* **2004**, 108 (39), 15150–15164. <https://doi.org/10.1021/jp037507r>.
- (20) Grubbs, R. K.; George, S. M. Attenuation of Hydrogen Radicals Traveling under Flowing Gas Conditions through Tubes of Different Materials. *J. Vac. Sci. Technol. A Vacuum, Surfaces, Film.* **2006**, 24 (3), 486–496. <https://doi.org/10.1116/1.2191862>.
- (21) Mallick, B. C.; Hsieh, C.-T.; Yin, K.-M.; Gandomi, Y. A.; Huang, K.-T. Review—On Atomic Layer Deposition: Current Progress and Future Challenges. *ECS J. Solid State Sci. Technol.* **2019**, 8 (4), N55–N78. <https://doi.org/10.1149/2.0201903jss>.
- (22) Knoop, H. C. M.; Potts, S. E.; Bol, A. A.; Kessels, W. M. M. *Atomic Layer Deposition*, Second Ed.; Elsevier B.V., 2015; Vol. 3. <https://doi.org/10.1016/B978-0-444-63304-0.00027-5>.
- (23) Atomic Limits Image Database <https://www.atomiclimits.com/imagebase/?img=aHR0cHM6Ly93d3cuYXRvbWljbGltZXZlbnNvbS93cC1jb250ZW50L3VwbG9hZHMvMjAyMC8xMS9TdXJmYWNLWFuZC1mbHV4LWNvbnRyb2xsZWQtZ3Jvd3RoLnN2ZW==> (accessed Nov 15, 2022).
- (24) Arts, K.; Vandalon, V.; Puurunen, R. L.; Utriainen, M.; Gao, F.; Kessels, W. M. M. (Erwin); Knoop, H. C. M. Sticking Probabilities of H<sub>2</sub>O and Al(CH<sub>3</sub>)<sub>3</sub> during Atomic Layer Deposition of Al<sub>2</sub>O<sub>3</sub> Extracted from Their Impact on Film

- Conformality. *J. Vac. Sci. Technol. A* **2019**, 37 (3), 030908. <https://doi.org/10.1116/1.5093620>.
- (25) Arts, K., Kessels, W.M.M., Knoop, H. C. M. Basic insights into ALD conformality – A closer look at ALD and thin film conformality. <https://www.atomiclimits.com/2020/02/08/basic-insights-into-ald-conformality-a-closer-look-at-ald-and-thin-film-conformality/> (accessed Nov 16, 2022).
- (26) George, S. M. Atomic Layer Deposition: An Overview. *Am. Chem. Soc.* **2010**, 111–131.
- (27) Arts, K.; Utriainen, M.; Puurunen, R. L.; Kessels, W. M. M.; Knoop, H. C. M. Film Conformality and Extracted Recombination Probabilities of O Atoms during Plasma-Assisted Atomic Layer Deposition of SiO<sub>2</sub>, TiO<sub>2</sub>, Al<sub>2</sub>O<sub>3</sub>, and HfO<sub>2</sub>. *J. Phys. Chem.* **2019**, 123 (44), 27030–27035. <https://doi.org/10.1021/acs.jpcc.9b08176>.
- (28) Coyle, J. P.; Dey, G.; Sirianni, E. R.; Kemell, M. L.; Yap, G. P. A.; Ritala, M.; Leskelä, M.; Elliott, S. D.; Barry, S. T. Deposition of Copper by Plasma-Enhanced Atomic Layer Deposition Using a Novel n-Heterocyclic Carbene Precursor. *Chem. Mater.* **2013**, 25 (7), 1132–1138. <https://doi.org/10.1021/cm400215q>.
- (29) Ritala, M.; Puurunen, R. L. Crystallinity of Inorganic Films Grown by Atomic Layer Deposition: Overview and General Trends. *J. Appl. Phys.* **2013**, 113. <https://doi.org/10.1063/1.4757907>.
- (30) Arts, W. M. M.; Kessels, H. C. M. Basic Insights into ALD Conformality - A Closer Look at ALD and Thin Film Conformality. *AtomicLimits* **2020**.
- (31) Cai, J.; Ma, Z.; Wejinya, U.; Zou, M.; Liu, Y.; Zhou, H.; Meng, X. A Revisit to Atomic Layer Deposition of Zinc Oxide Using Diethylzinc and Water as Precursors. *J. Mater. Sci.* **2019**, 54 (7), 5236–5248. <https://doi.org/10.1007/s10853-018-03260-3>.
- (32) Richey, N. E.; De Paula, C.; Bent, S. F. Understanding Chemical and Physical Mechanisms in Atomic Layer Deposition. *J. Chem. Phys.* **2020**, 152 (4). <https://doi.org/10.1063/1.5133390>.
- (33) Hashimi, M.S.J., Leskela, M., Niinisto, J., Ritala, M. Comprehensive Materials Processing - Atomic Layer Deposition; 2014.
- (34) Martin Vos, Adrie Mackus, E. K. Atomic Layer Deposition Process Development. *AtomicLimits* **2019**.
- (35) Knisley, T. J.; Kalutarage, L. C.; Winter, C. H. Precursors and Chemistry for the Atomic Layer Deposition of Metallic First Row Transition Metal Films. *Coord. Chem. Rev.* **2013**, 257 (23–24), 3222–3231. <https://doi.org/10.1016/j.ccr.2013.03.019>.
- (36) Eaborn, C. *Organometallic Chemistry, Volume 12*; **1984**; Vol. 276. [https://doi.org/10.1016/0022-328x\(84\)80620-8](https://doi.org/10.1016/0022-328x(84)80620-8).

- (37) Hwang, C. S. *Atomic Layer Deposition for Semiconductors*; **2014**; Vol. 9781461480. <https://doi.org/10.1007/978-1-4614-8054-9>.
- (38) Nai, S. M. L.; Tan, L. Bin; Selvanayagam, C. *Handbook of Manufacturing Engineering and Technology*; **2015**. [https://doi.org/10.1007/978-1-4471-4670-4\\_59](https://doi.org/10.1007/978-1-4471-4670-4_59).
- (39) Kunte, G. V.; Shivashankar, S. A.; Umarji, A. M. Thermogravimetric Evaluation of the Suitability of Precursors for MOCVD. *Meas. Sci. Technol.* **2008**, *19* (2). <https://doi.org/10.1088/0957-0233/19/2/025704>.
- (40) Kalutarage, L. C.; Heeg, M. J.; Martin, P. D.; Saly, M. J.; Kuiper, D. S.; Winter, C. H. Volatility and High Thermal Stability in Mid-to-Late First-Row Transition-Metal Complexes Containing 1,2,5-Triazapentadienyl Ligands. *Inorg. Chem.* **2013**, *52* (3), 1182–1184. <https://doi.org/10.1021/ic302787z>.
- (41) Kim, T.; Zaera, F. Surface Chemistry of Pentakis(Dimethylamido)Tantalum on Ta Surfaces. *J. Phys. Chem.* **2011**, *115* (16), 8240–8247. <https://doi.org/10.1021/jp201564v>.
- (42) Mashid, S.; Askari, M.; Sasani Ghamsar, M. Synthesis of TiO<sub>2</sub> Nanoparticles by Hydrolysis and Peptization of Titanium Isopropoxide Solution. *Mater. Process. Technol.* **2006**, *15* (5), 772–779. <https://doi.org/10.1016/j.jmatprotec.2007.01.040>.
- (43) Chaukulkar, R. P.; Agarwal, S. Atomic Layer Deposition of Titanium Dioxide Using Titanium Tetrachloride and Titanium Tetraisopropoxide as Precursors. *J. Vac. Sci. Technol. A Vacuum, Surfaces, Film.* **2013**, *31* (3), 031509. <https://doi.org/10.1116/1.4798385>.
- (44) Bradley, D. C.; Mehta, M. L. Alkoxides of Vanadium (IV). *Can. J. Chem.* **1962**, *40* (6), 1183–1188. <https://doi.org/10.1139/v62-180>.
- (45) Westrup, K. C. M.; Gregório, T.; Stinghen, D.; Reis, D. M.; Hitchcock, P. B.; Ribeiro, R. R.; Barison, A.; Back, D. F.; De Sá, E. L.; Nunes, G. G.; et al. Non-Oxo Vanadium(IV) Alkoxide Chemistry: Solid State Structures, Aggregation Equilibria and Thermochromic Behaviour in Solution. *Dalton Trans.* **2011**, *40* (13), 3198–3210. <https://doi.org/10.1039/c0dt01547d>.
- (46) Hales, J. J.; Trudeau, M. L.; Antonelli, D. M.; Kaltsoyannis, N. Computational Study of H<sub>2</sub> Binding to MH<sub>3</sub> (M = Ti, V, or Cr). *Dalton Trans.* **2019**, *48* (15), 4921–4930. <https://doi.org/10.1039/c9dt00025a>.
- (47) Pan, Y.; Yu, E. Theoretical Prediction of Structure, Electronic and Optical Properties of VH<sub>2</sub> Hydrogen Storage Material. *Int. J. Hydrogen Energy* **2022**, *47* (64), 27608–27616. <https://doi.org/10.1016/j.ijhydene.2022.06.080>.
- (48) Cao, Y.; Saito, A.; Kobayashi, Y.; Ubukata, H.; Tang, Y.; Kageyama, H. Vanadium Hydride as an Ammonia Synthesis Catalyst. *ChemCatChem* **2021**, *13* (1), 191–195. <https://doi.org/10.1002/cctc.202001084>.
- (49) Reilly, J. J.; Wiswall, R. H. The Higher Hydrides of Vanadium and Niobium. *Inorg. Chem.* **1970**, *9* (7), 1678–1682. <https://doi.org/10.1021/ic50089a013>.

- (50) Matumura, T.; Yukawa, H.; Morinaga, M. Alloying Effects on the Electronic Structures of  $VH_2$  and  $V_2H_5$ . *J. Alloys Compd.* **1999**, *284* (1–2), 82–88. [https://doi.org/10.1016/S0925-8388\(98\)00466-6](https://doi.org/10.1016/S0925-8388(98)00466-6).
- (51) Maeland, A. J. Investigation of the Vanadium-Hydrogen System by X-Ray Diffraction Techniques. **1962**, *68* (8), 2197–2200.
- (52) Kurup, S. S.; Staples, R. J.; Lord, R. L.; Groysman, S. Synthesis of Chromium(II) Complexes with Chelating Bis(Alkoxide) Ligand and Their Reactions with Organoazides and Diazoalkanes. *Molecules* **2020**, *25* (2). <https://doi.org/10.3390/molecules25020273>.
- (53) Horvath, E. G. Chromium(II) Alkoxides. *Z. anorg. allg. Chem.* **1979**, *61*, 51–61. <https://doi.org/10.1002/zaac.19794570106>
- (54) Nöth, H.; Seitz, M. Preparation and Characterization of Chromium(II) Tetrahydroborate- Tetrahydrofuran (1/2). *J. Chem. Soc. Chem. Commun.* **1976**, *547* (24), 1976. <https://doi.org/10.1039/C3976001004a>.
- (55) Basi, J. S.; Chisholm, M. H.; Mary, Q. Covalent Compounds of Quadrivalent Transition Metals. Part II. Chromium(IV) Tertiary Alkoxides and Triethylsilyloxiide. *J. Chem. Soc. A*, **1971**, No. 772, 772–776. <https://doi.org/10.1039/J19710000772>.
- (56) Tsuda, Tetsuo, Kochi, J. K. Reactions of Grignard Reagents with Chromium(IV) t-Butoxide: Unstable Organochromium(IV) Intermediates. 1972, pp 648–649. <https://doi.org/10.1246/bcsj.45.648>.
- (57) Hagihara, Nobue, Yamazaki, H. Chromium Tetra-t-Butoxide. *J. Am. Chem. Soc.* **1959**, *25* (1), 5–6. <https://doi.org/10.1021/ja01521a079>.
- (58) Mclendon, G.; Thaler, E. G.; Rypdal, K.; Haaland, A.; Caulton, K. G. Structure and Reactivity of  $Cr(OCMe_3)_4$ . *Inorg. Chem.* **1989**, 2431–2434. <https://doi.org/10.1021/ic00311a035>.
- (59) Thaler, E. G.; Rypdal, K.; Haaland, A.; Caulton, K. G. Structure and Reactivity of  $Cr(OCMe_3)_4$ . *Inorg. Chem.* **1989**, *28* (12), 2431–2434. <https://doi.org/10.1021/ic00311a035>.
- (60) Wilkinson, C. and. *Advanced Inorganic Chemistry*, Fifth. Ed.; 1988.
- (61) Mehrotra, R. C. Preparation and Reactions of Chromium(III)Alkoxides. *Synth. React. Inorg. Met. Chem.* **1990**, *20* (7), 963–973. <https://doi.org/10.1080/00945719008048188>.
- (62) Marizy, A.; Geneste, G.; Loubeyre, P.; Guigue, B.; Garbarino, G. Synthesis of Bulk Chromium Hydrides under Pressure of up to 120 GPa. *Phys. Rev.* **2018**, *184103*, 1–7. <https://doi.org/10.1103/PhysRevB.97.184103>.
- (63) Stock, A. D.; Hardcastle, K. I. Phase and Composition Analysis of Chromium Hydride. *J. Inorg. and Nucl. Chem.* **1970**, *32*, 1183–1186. [https://doi.org/10.1016/0022-1902\(70\)80113-0](https://doi.org/10.1016/0022-1902(70)80113-0)

- (64) Ganesan, J. P.; Dev, D.; Krishnaprasad, A.; Feit, C.; Moser, D.; Kanjolia, R. K.; Roy, T.; Banerjee, P. Semiconductor-to-Metal Transition in Atomic Layer Deposition (ALD) of VO<sub>2</sub> Films Using VCl<sub>4</sub> and Water. *Appl. Phys. Lett.* **2021**, *118* (26). <https://doi.org/10.1063/5.0053566>.
- (65) Povey, I. M.; Bardosova, M.; Chalvet, F.; Pemble, M. E.; Yates, H. M. Atomic Layer Deposition for the Fabrication of 3D Photonic Crystals Structures: Growth of Al<sub>2</sub>O<sub>3</sub> and VO<sub>2</sub> Photonic Crystal Systems. *Surf. Coatings Technol.* **2007**, *201* (22-23 SPEC. ISS.), 9345–9348. <https://doi.org/10.1016/j.surfcoat.2007.04.108>.
- (66) Dagur, P.; Mane, A. U.; Shivashankar, S. A. Thin Films of VO<sub>2</sub> on Glass by Atomic Layer Deposition: Microstructure and Electrical Properties. *J. Cryst. Growth* **2005**, *275* (1–2), 1223–1228. <https://doi.org/10.1016/j.jcrysgr.2004.11.144>.
- (67) Østreng, E.; Nilsen, O.; Fjellvåg, H. Optical Properties of Vanadium Pentoxide Deposited by ALD. *J. Phys. Chem. C* **2012**, *116* (36), 19444–19450. <https://doi.org/10.1021/jp304521k>.
- (68) Premkumar, P. A.; Toeller, M.; Radu, I. P.; Adelman, C.; Schaekers, M.; Meersschant, J.; Conard, T.; Elshocht, S. Van. Process Study and Characterization of VO<sub>2</sub> Thin Films Synthesized by ALD Using TEMAV and O<sub>3</sub> Precursors. *ECS J. Solid State Sci. Technol.* **2012**, *1* (4), P169–P174. <https://doi.org/10.1149/2.009204jss>.
- (69) Mattelaer, F.; Geryl, K.; Rampelberg, G.; Dobbelaere, T.; Dendooven, J.; Detavernier, C. Atomic Layer Deposition of Vanadium Oxides for Thin-Film Lithium-Ion Battery Applications. *RSC Adv.* **2016**, *6* (115), 114658–114665. <https://doi.org/10.1039/C6RA25742A>.
- (70) Blanquart, T.; Niinistö, J.; Gavagnin, M.; Longo, V.; Heikkilä, M.; Puukilainen, E.; Pallem, V. R.; Dussarrat, C.; Ritala, M.; Leskelä, M. Atomic Layer Deposition and Characterization of Vanadium Oxide Thin Films. *RSC Adv.* **2013**, *3* (4), 1179–1185. <https://doi.org/10.1039/c2ra22820c>.
- (71) Wang, X.; Guo, Z.; Gao, Y.; Wang, J. Atomic Layer Deposition of Vanadium Oxide Thin Films from Tetrakis(Dimethylamino)Vanadium Precursor. *J. Mater. Res.* **2017**, *32* (1), 37–44. <https://doi.org/10.1557/jmr.2016.303>.
- (72) YUN, S.; LIM, J.; KIM, H. Method of Manufacturing Vanadium Oxide Thin Film. *2007/024094 Al* **2007**, *14* (12).
- (73) Cui, Y.; Ke, Y.; Liu, C.; Chen, Z.; Wang, N.; Zhang, L.; Zhou, Y.; Wang, S.; Gao, Y.; Long, Y. Thermochromic VO<sub>2</sub> for Energy-Efficient Smart Windows. *Joule* **2018**, *2* (9), 1707–1746. <https://doi.org/10.1016/j.joule.2018.06.018>.
- (74) Liu, Y.; Clark, M.; Zhang, Q.; Yu, D.; Liu, D.; Liu, J.; Cao, G. V<sub>2</sub>O<sub>5</sub> Nano-Electrodes with High Power and Energy Densities for Thin Film Li-Ion Batteries. *Adv. Energy Mater.* **2011**, *1* (2), 194–202. <https://doi.org/10.1002/aenm.201000037>.

- (75) An, Q.; Zhang, P.; Xiong, F.; Wei, Q.; Sheng, J.; Wang, Q.; Mai, L. Three-Dimensional Porous  $V_2O_5$  Hierarchical Octahedrons with Adjustable Pore Architectures for Long-Life Lithium Batteries. *Nano Res.* **2015**, *8* (2), 481–490. <https://doi.org/10.1007/s12274-014-0638-1>.
- (76) Kane, S. N.; Mishra, A.; Dutta, A. K. Structure and Optical Properties of Hydrothermally Synthesized Vanadium Oxides Nanobelts. *J. Phys. Conf. Ser.* **2016**, *755* (1). <https://doi.org/10.1088/1742-6596/755/1/011001>.
- (77) Kalutarage, L. C.; Martin, P. D.; Heeg, M. J.; Winter, C. H. Volatile and Thermally Stable Mid to Late Transition Metal Complexes Containing  $\alpha$  - Imino Alkoxide Ligands, a New Strongly Reducing Coreagent, and Thermal Atomic Layer Deposition of Ni, Co, Fe, and Cr Metal Films. *J. Am. Chem. Soc.* **2013**, *135*, 10–13. <https://doi.org/10.1021/ja407014w>.
- (78) Elgrishi, N.; Rountree, K. J.; McCarthy, B. D.; Rountree, E. S.; Eisenhart, T. T.; Dempsey, J. L. A Practical Beginner's Guide to Cyclic Voltammetry. *J. Chem. Educ.* **2018**, *95* (2), 197–206. <https://doi.org/10.1021/acs.jchemed.7b00361>.
- (79) Bard, Allen J., Faulkner, L. R. *Electrochemical Methods Fundamentals and Applications*; John Wiley & Sons. Inc., 2001.
- (80) Nicholson, R. S. Semiempirical Procedure for Measuring with Stationary Electrode Polarography Rates of Chemical Reactions Involving the Product of Electron Transfer. *Anal. Chem.* **1966**, *38* (10), 1406. <https://doi.org/10.1021/ac60242a030>.
- (81) Cho, W.; Sung, K.; An, K.-S.; Sook Lee, S.; Chung, T.-M.; Kim, Y. Atomic Layer Deposition of  $Al_2O_3$  Thin Films Using Dimethylaluminum Isopropoxide and Water. *J. Vac. Sci. Technol. A Vacuum, Surfaces, Film.* **2003**, *21* (4), 1366–1370. <https://doi.org/10.1116/1.1562184>.
- (82) Cao, L.; Mattelaer, F.; Sajavaara, T.; Dendooven, J.; Detavernier, C. A Liquid Alkoxide Precursor for the Atomic Layer Deposition of Aluminum Oxide Films. *J. Vac. Sci. Technol. A* **2020**, *38* (2), 022417. <https://doi.org/10.1116/1.5139631>.
- (83) Rahtu, A.; Ritala, M. Reaction Mechanism Studies on Atomic Layer Deposition of  $Zr_xTi_yO_z$  Using the Novel Metal Halide-Metal Alkoxide Approach. *Langmuir* **2008**, *26* (2), 848–853. <https://doi.org/10.1021/la026357t>.
- (84) Saito, T.; Nishiyama, H.; Tanahashi, H.; Kawakita, K.; Tsurugi, H.; Mashima, K. 1,4-Bis(Trimethylsilyl)-1,4-Diaza-2,5-Cyclohexadienes as Strong Salt-Free Reductants for Generating Low-Valent Early Transition Metals with Electron-Donating Ligands. *J. Am. Chem. Soc.* **2014**. <https://doi.org/10.1021/ja501313s>
- (85) Tsurugi, H.; Tanahashi, H.; Nishiyama, H.; Fegler, W.; Saito, T.; Sauer, A.; Okuda, J.; Mashima, K. Salt-Free Reducing Reagent of Bis(Trimethylsilyl)Cyclohexadiene Mediates Multielectron Reduction of Chloride Complexes of W(VI) and W(IV). *J. Am. Chem. Soc.* **2013**, *135* (16), 5986–5989. <https://doi.org/10.1021/ja401589a>.

- (86) Tsurugi, H.; Saito, T.; Tanahashi, H.; Arnold, J.; Mashima, K. Carbon Radical Generation by  $d^0$  Tantalum Complexes with  $\alpha$ -Diimine Ligands through Ligand-Centered Redox Processes. *J. Am. Chem. Soc.* **2011**, *133* (46), 18673–18683. <https://doi.org/10.1021/ja204665s>.
- (87) Graf, D.; Frank, M.; Ojelere, O.; Gessner, I.; Juergensen, L.; Grosch, M.; Mathur, S. Structure-Decomposition Relationships of Homoleptic and Heteroleptic Vanadium(IV) Alkoxides for Defined Gas Phase Depositions of  $VO_2$  and  $V_2O_3$  thin Films. *Mater. Today Proc.* **2019**, *33*, 2445–2450. <https://doi.org/10.1016/j.matpr.2020.01.334>.
- (88) Zhou, J.; Jiang, B.; Zhao, Z.; Shibata, N. Etherification of Fluoroarenes with Alkoxyboronic Acid Pinacol Esters via C-F Bond Cleavage. *Org. Lett.* **2022**, *24* (28), 5084–5089. <https://doi.org/10.1021/acs.orglett.2c01864>.
- (89) Makarov, K.; Kaushansky, A.; Eisen, M. S. Catalytic Hydroboration of Esters by Versatile Thorium and Uranium Amide Complexes. *ACS Catal.* **2022**, *12* (1), 273–284. <https://doi.org/10.1021/acscatal.1c04799>.
- (90) Zhang, Q.; Wang, S.; Yin, J.; Xiong, T.; Zhang, Q. Remote Site-Selective Asymmetric Protoboration of Unactivated Alkenes Enabled by Bimetallic Relay Catalysis. *Angew. Chemie - Int. Ed.* **2022**, *61* (23). <https://doi.org/10.1002/anie.202202713>.
- (91) Yan, B.; Dutta, S.; Ma, X.; Ni, C.; Koley, D.; Yang, Z.; Roesky, H. W. Organoaluminum Hydrides Catalyzed Hydroboration of Carbonates, Esters, Carboxylic Acids, and Carbon Dioxide. *Dalton Trans.* **2022**, *51* (17), 6756–6765. <https://doi.org/10.1039/d2dt00785a>.
- (92) Mukhopadhyay, T. K.; Flores, M.; Groy, T. L.; Trovitch, R. J. A Highly Active Manganese Precatalyst for the Hydrosilylation of Ketones and Esters. **2014**, *90* (2). <https://doi.org/10.1021/ja4116346>.
- (93) Gao, D.; Cui, C. N-Heterocyclic Carbene Organocatalysts for Dehydrogenative Coupling of Silanes and Hydroxyl Compounds. *Chem. - A Eur. J.* **2013**, *19* (34), 11143–11147. <https://doi.org/10.1002/chem.201301893>.
- (94) Yoshida, T.; Ilies, L.; Nakamura, E. Silylation of Aryl Halides with Monoorganosilanes Activated by Lithium Alkoxide. *Org. Lett.* **2018**, *20* (10), 2844–2847. <https://doi.org/10.1021/acs.orglett.8b00818>.
- (95) Griffiths, M.; Dubrawski, Z.; Bačić, G.; Masuda, J.; Japahuge, A.; Zeng, T.; Barry, S. Controlling Thermal Stability and Volatility of Organogold (I) Compounds for Vapor Deposition with Complementary Ligand Design. *Eur. J. Inorg. Chem.* **2019**, 4927–4938. <https://doi.org/10.1002/ejic.201901087>.
- (96) Filler, Robert, Schure, R. M. Highly Acidic Perhalogenated Alcohols. A New Synthesis of Perfluoro-*t*-Butyl Alcohol. *J. Org. Chem.* **1967**, *4948* (April), 1217–1219. <https://doi.org/10.1021/jo01279a081>
- (97) Reeve, W.; Erikson, C. M.; Aluotto, P. F. A New Method for the Determination of

the Relative Acidities of Alcohols in Alcoholic Solutions. The Nucleophilicities and Competitive Reactivities of Alkoxides and Phenoxides. *Can. J. Chem.* **1979**, *57* (20), 2747–2754. <https://doi.org/10.1139/v79-444>.

- (98) Köhn, R. D.; Coxon, A. G. N.; Chunawat, S.; Heron, C.; Mihan, S.; Lyall, C. L.; Reeksting, S. B.; Kociok-Köhn, G. Triazacyclohexane Chromium Triflate Complexes as Precursors for the Catalytic Selective Olefin Trimerisation and Its Investigation by Mass Spectrometry. *Polyhedron* **2020**, *185*, 114572. <https://doi.org/10.1016/j.poly.2020.114572>.
- (99) Connelly, N. G.; Geiger, W. E. Chemical Redox Agents for Organometallic Chemistry. *Chem. Rev.* **1996**, *96* (2), 877–910. <https://doi.org/10.1021/cr940053x>.
- (100) Zumdahl, Steven S., Zumdahl, S. A. *Chemistry*, 9th ed.; Cengage Learning, 2014.
- (101) Indirect Referencing <https://www.cif.iastate.edu/nmr/nmr-tutorials/indirectref> (accessed Nov 30, 2022).
- (102) Ghadwal, R. S.; Roesky, H. W.; Merkel, S.; Henn, J.; Stalke, D. Lewis Base Stabilized Dichlorosilylene. *Angew. Chemie - Int. Ed.* **2009**, *48* (31), 5683–5686. <https://doi.org/10.1002/anie.200901766>.
- (103) Ghana, P.; Arz, M. I.; Schnakenburg, G.; Straßmann, M.; Filippou, A. C. Metal-Silicon Triple Bonds: Access to  $[\text{Si}(\eta^5\text{-C}_5\text{Me}_5)]^+$  from  $\text{SiX}_2(\text{NHC})$  and Its Conversion to the Silylidyne Complex  $[\text{TpMe}(\text{CO})_2\text{MoSi}(\eta^5\text{-C}_5\text{Me}_5)]$  ( $\text{TpMe} = \kappa^3\text{-N, N', N''-Hydridotris(3,5-Dimethyl-1-Pyrazolyl)Borate}$ ). *Organometallics* **2018**, *37* (5), 772–780. <https://doi.org/10.1021/acs.organomet.7b00665>.
- (104) Fujimoto, T.; Ritter, T. PhenoFluorMix: Practical Chemoselective Deoxyfluorination of Phenols. *Org. Lett.* **2015**, *17* (3), 544–547. <https://doi.org/10.1021/ol5035518>.
- (105) Klesko, J. P.; Thrush, C. M.; Winter, C. H. Thermal Atomic Layer Deposition of Titanium Films Using Titanium Tetrachloride and 2-Methyl-1,4-Bis(trimethylsilyl)-2,5-Cyclohexadiene or 1,4-Bis(trimethylsilyl)-1,4-Dihydropyrazine. *Chem. Mater.* **2015**, *27* (14), 4918–4921. <https://doi.org/10.1021/acs.chemmater.5b01707>.